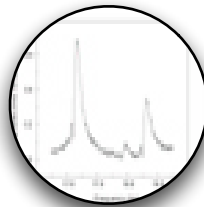
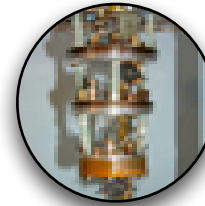
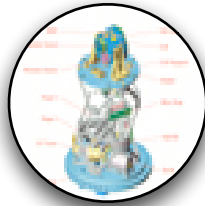
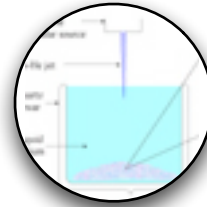
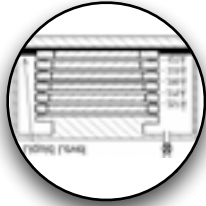


## CHAPTER 2

### CONDENSED MATTER & LOW TEMPERATURE PHYSICS





# ESR Investigations of Atoms Stabilized in Impurity-Helium Solids

S.I. Kiselev, V.V. Khmelenko,  
and D.M. Lee

Laboratory of Atomic and Solid State Physics,  
Cornell University

Quantum fluids and solids have been studied intensively by low temperature physicists for almost a century. We define quantum fluids and solids by comparing the interparticle spacing of the identical particles comprising the fluid or solid with the thermal de Broglie wave length of these entities. When these lengths become comparable, we are in the quantum regime. These investigations have led to many remarkable phenomena including superfluidity, superconductivity, Bose Einstein condensation in atomic gases, quantized vortices, magnetic phase transitions and a multitude of other effects. We have been investigating impurity-helium (Im-He) solids, which are porous complex gel-like substances consisting of individual impurity atoms and/or molecules or clusters of impurity atoms and/or molecules, each surrounded by a thin layer of solid helium. Van der Waals forces are responsible for binding together these constituents. The samples are prepared by injecting a beam of mixed helium and impurity gas into a beaker of superfluid helium at  $T = 1.5$  K. Snowflake like particles of the Im-He solid form in the liquid helium and fall to the bottom of the beaker where they congeal to form our sample. We have investigated the formation and evolution of Im-He solids containing atomic hydrogen, deuterium, and mixtures of molecular hydrogen and deuterium in an attempt to maximize the hydrogen atom concentration, with the ultimate goal of creating a new quantum solid. The experiments were performed at  $T = 1.35$  K.



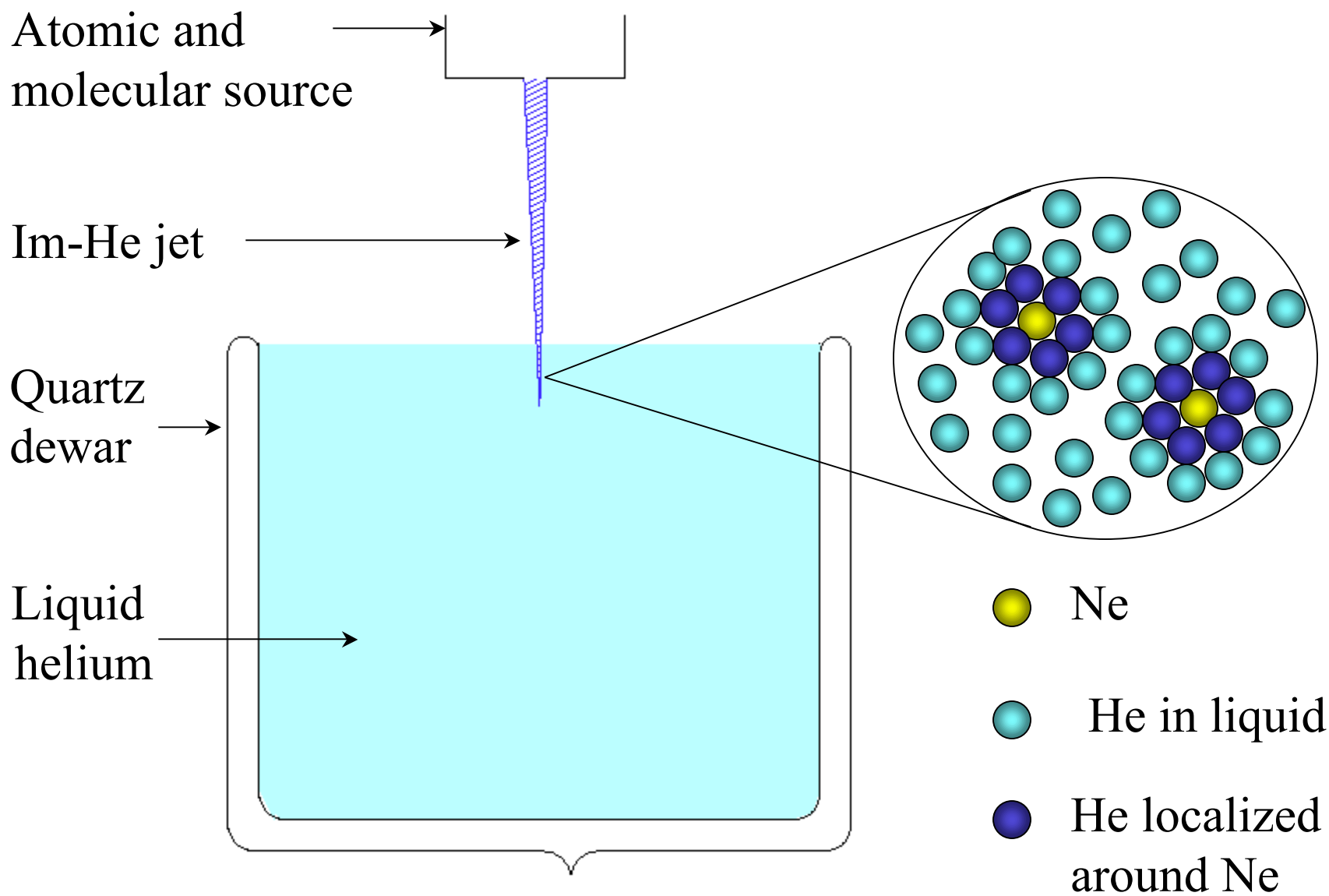


Figure 1a.

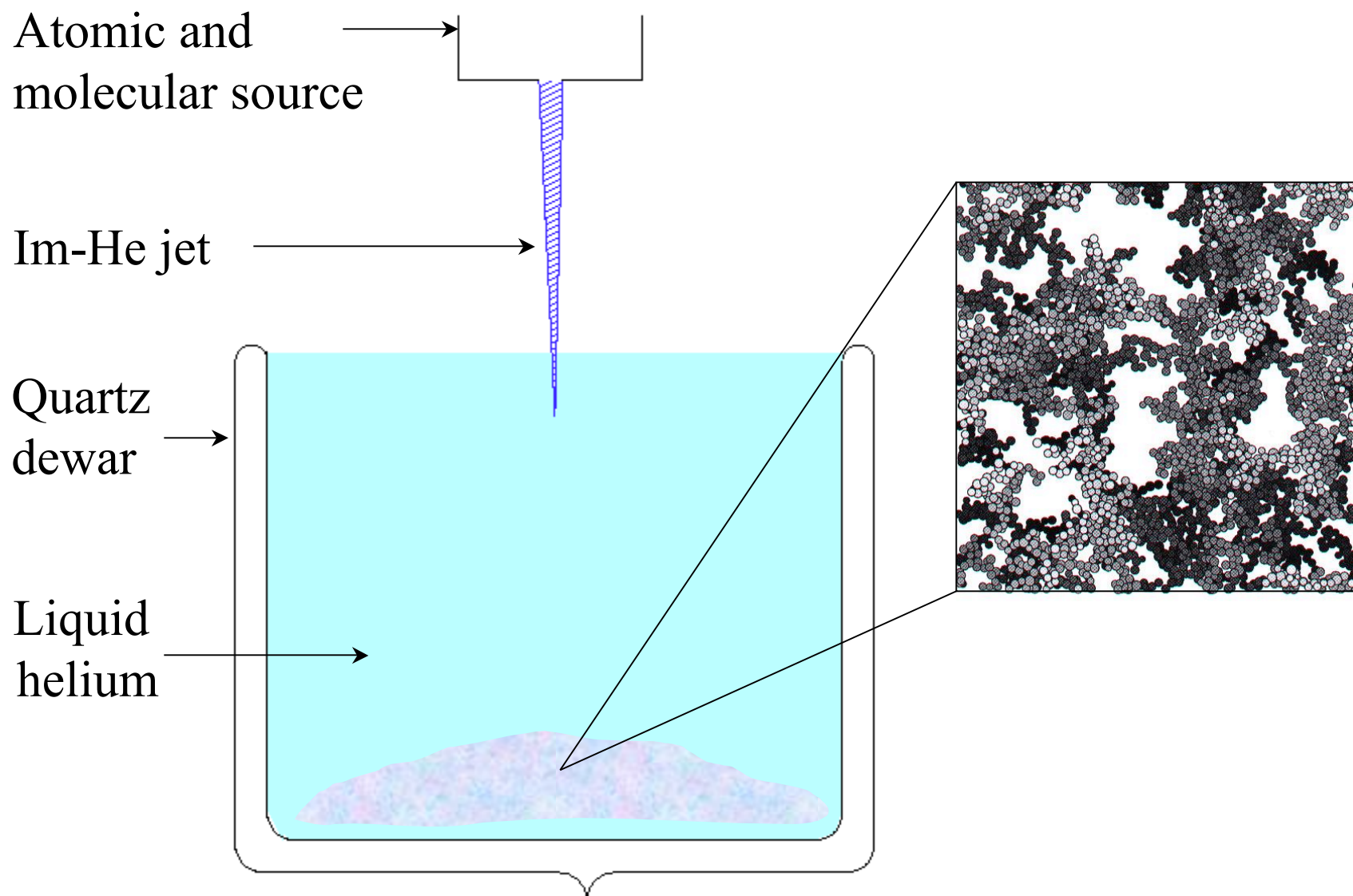


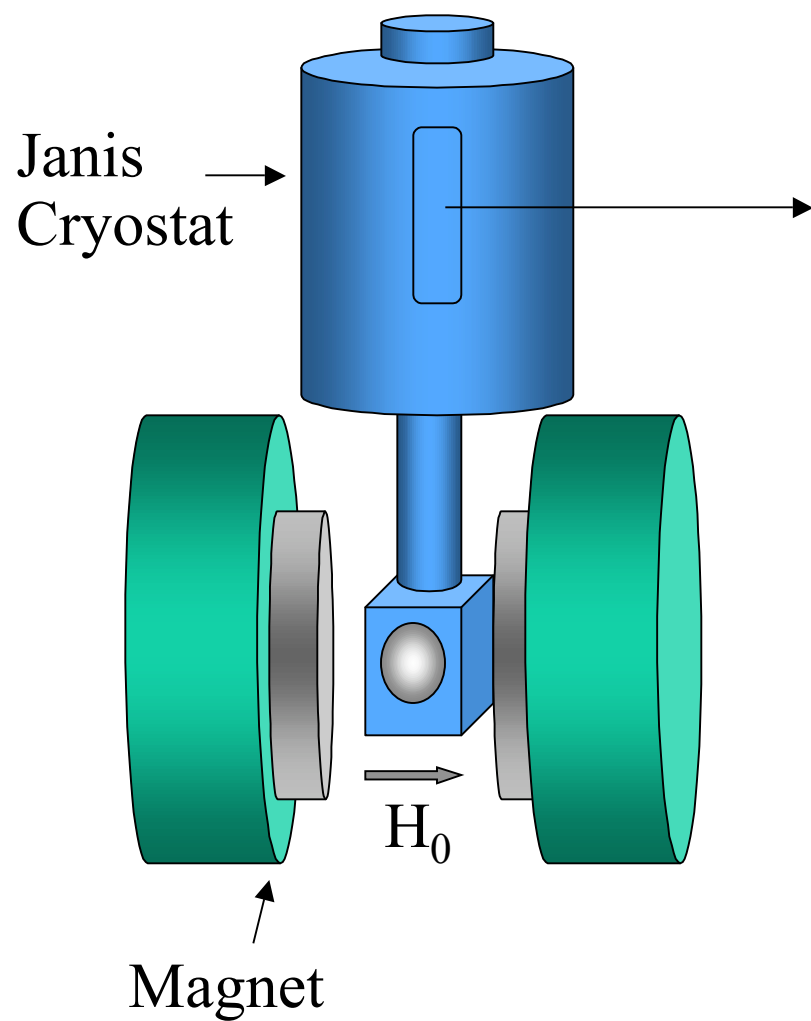
Figure 1b.

Figure 1 shows the basic scheme for sample preparation.

In Fig. 1a, the mixed beam of the impurity gas and helium gas penetrates the surface of the superfluid He in the collection beaker followed by the formation of thin layers of solid helium around the impurity atoms or small clusters of impurity atoms. In this case Ne atoms correspond to the impurities.

In Fig. 1b, the small Im-He solid clusters sink to the bottom of the collection beaker where they stick together to form macroscopic samples of an Im-He solid. The inset shows a micrograph of aerogel which is thought to have a porous structure similar to that of Im-He solids.

Figure 2.



## Sample preparation setup.

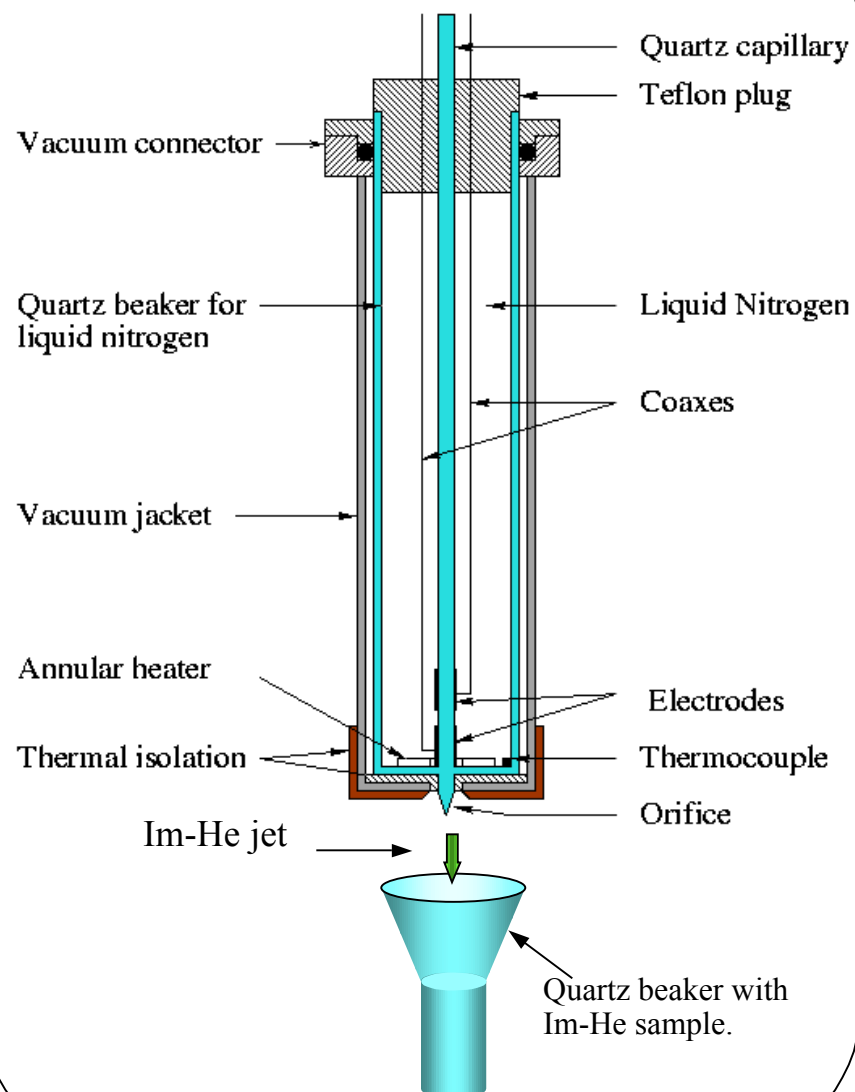
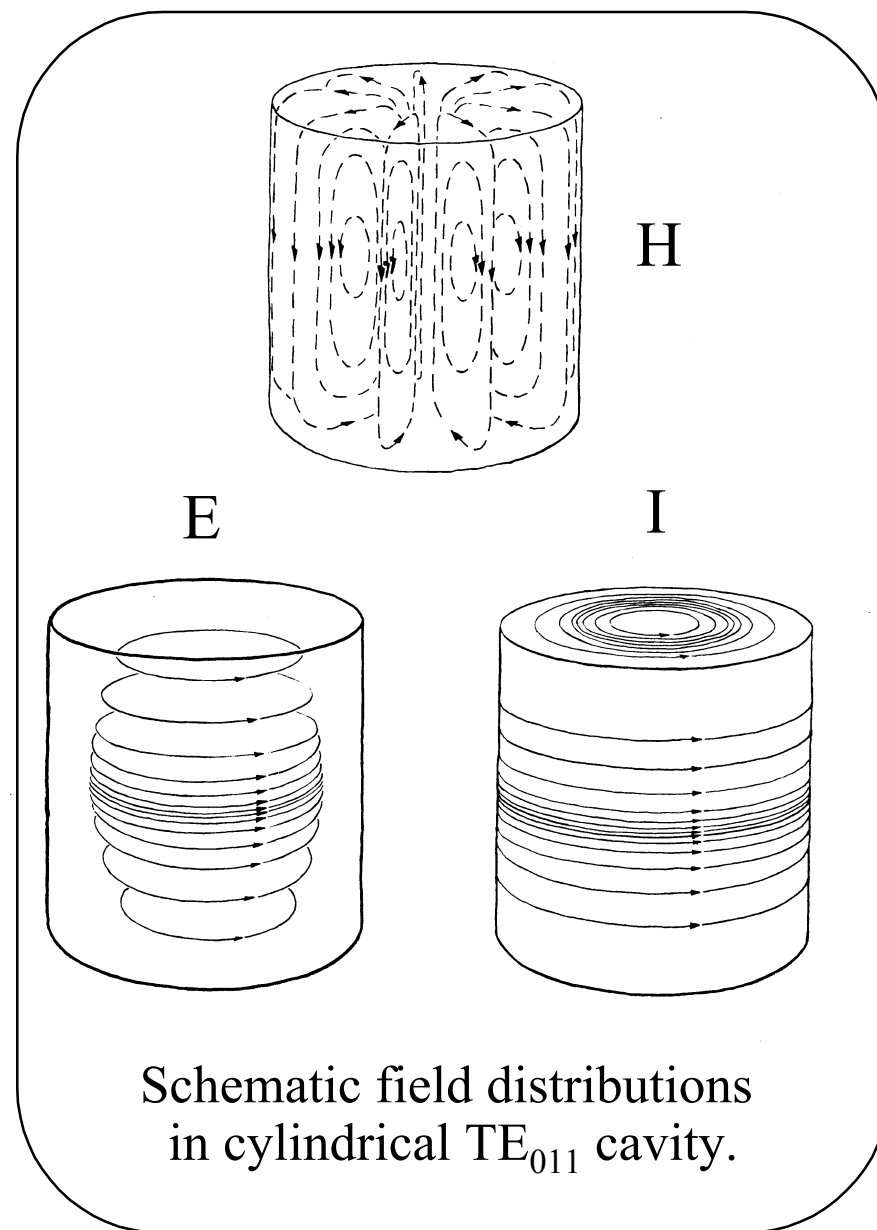
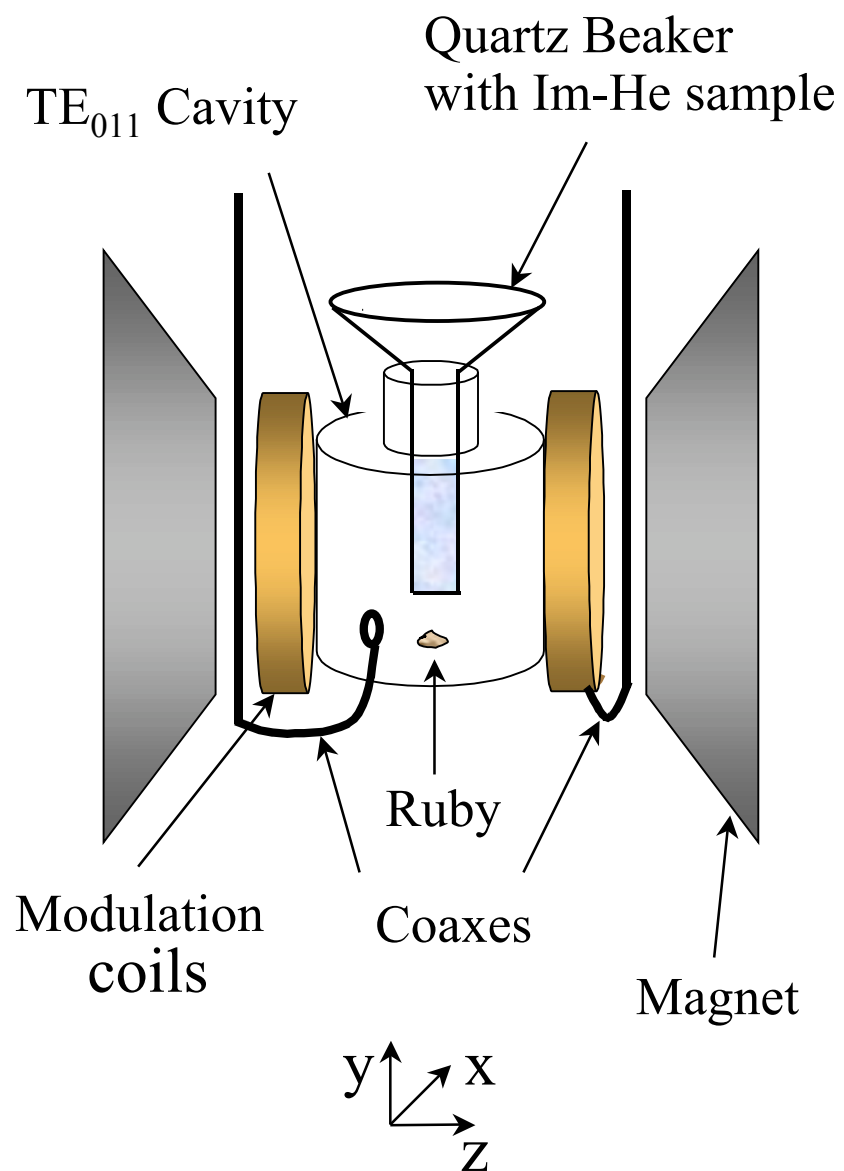


Figure 2 shows the commercial variable temperature Janis cryostat with a tail designed to fit in between the 12 inch pole pieces of a homogeneous electromagnet. Optical access is also provided. Also displayed in figure 2 is the sample preparation setup. The make-up gases are mixed in an external gas handling system and then travel down a central quartz capillary surrounded by liquid  $N_2$ . Electrodes are provided in order to apply a radiofrequency discharge to the gas flowing through the tube. The experiments discussed in this presentation involve atomic hydrogen and/or deuterium in Im-He solids prepared from  $H_2:D_2:He$  gas mixtures. The gaseous discharge dissociates a large fraction of the  $H_2$  and  $D_2$  molecules so that a considerable number of H and D atoms are found in the Im-He solid. The upper end of the quartz collection beaker is flared out in the form of a cone in order to capture a maximum amount of the Im-He sample emerging from the orifice.

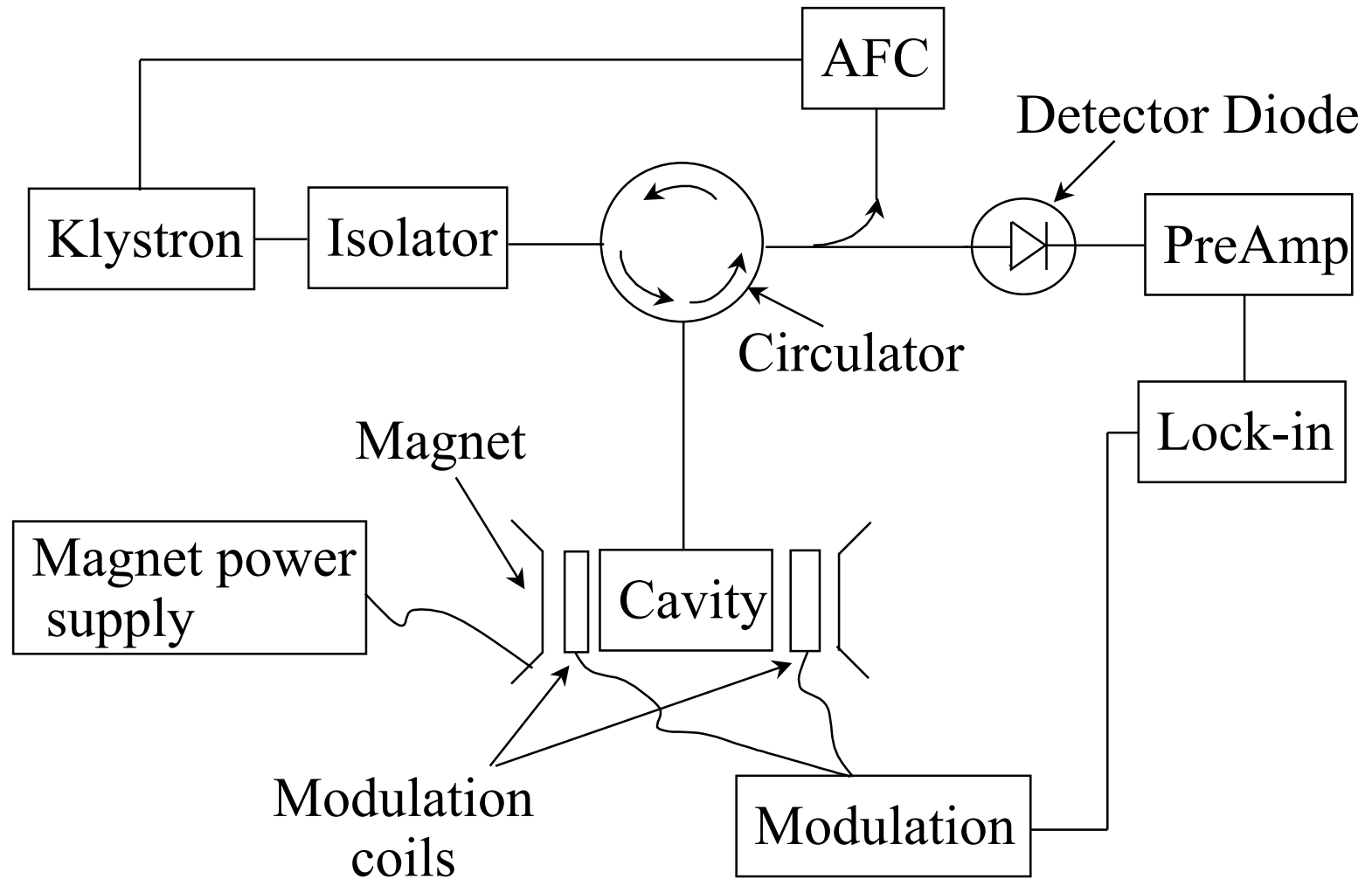
Figure 3.



In order to perform electron spin resonance experiments, the sample beaker is lowered into a  $TE_{011}$  cylindrical resonant cavity surrounded by a set of 100 kHz modulation coils. A schematic drawing of the cavity is shown in figure 3. A small coupling loop is used to excite microwaves in the cavity. A ruby crystal is placed at the bottom of the cavity for the purpose of calibration. The field profiles for our cavity are also shown in figure 3. It should be noted that the maximum value of the microwave magnetic field is along the cylinder axis. Near the top and bottom of the cavity, the microwave magnetic fields have large horizontal components. The electric field and the induced currents are small near the axis, so a hole can be placed in the top of the cavity with minimal disruption to the field patterns.

Figure 4.

## ESR Spectrometer.



$$H = H_0 + (dH/dt)t + H_{\text{mod}} \cos(\omega t), \quad \omega = 2\pi \cdot 100 \text{ kHz}$$

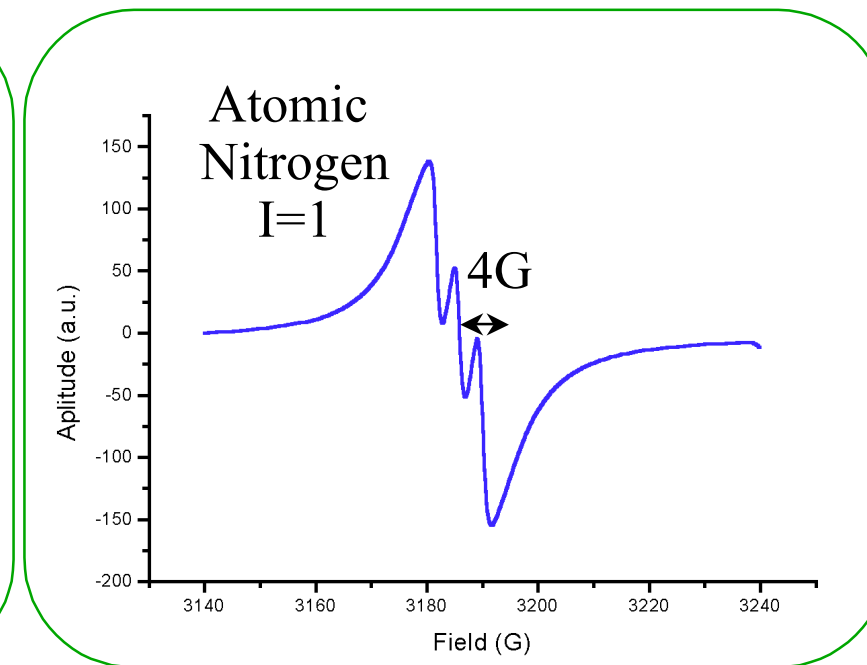
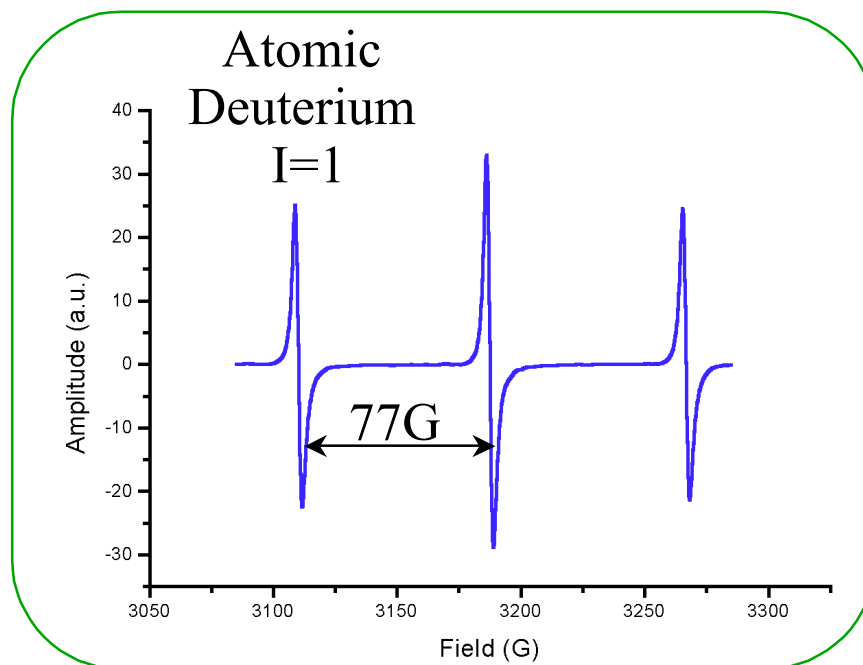
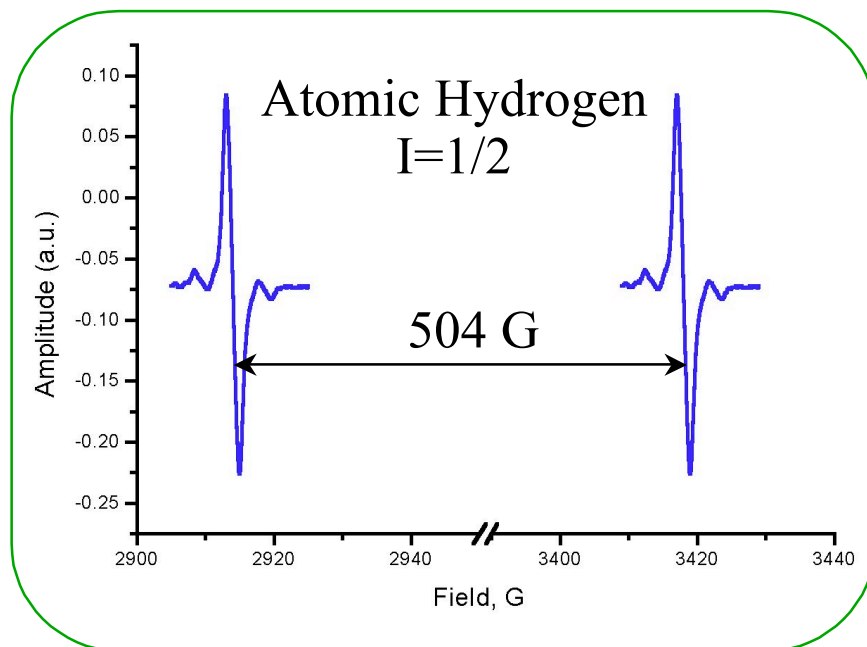


The microwave spectrometer employed in these experiments operated at about 9 GHz with an applied steady field on the sample of 0.3 tesla, (3 kG). A simple homodyne scheme was used, as shown in figure 4. A continuous wave signal generated by the klystron was routed to the  $TE_{011}$  cavity by a circulator.

The microwaves were reflected by the cavity and then routed by the circulator to the detector and amplifier chain. The steady field was ac modulated by the aforementioned 100 kHz signal. This allowed lock in detection to be performed, increasing the sensitivity. The output of the lock in detector corresponded to the derivative of an electron spin resonance absorption line.

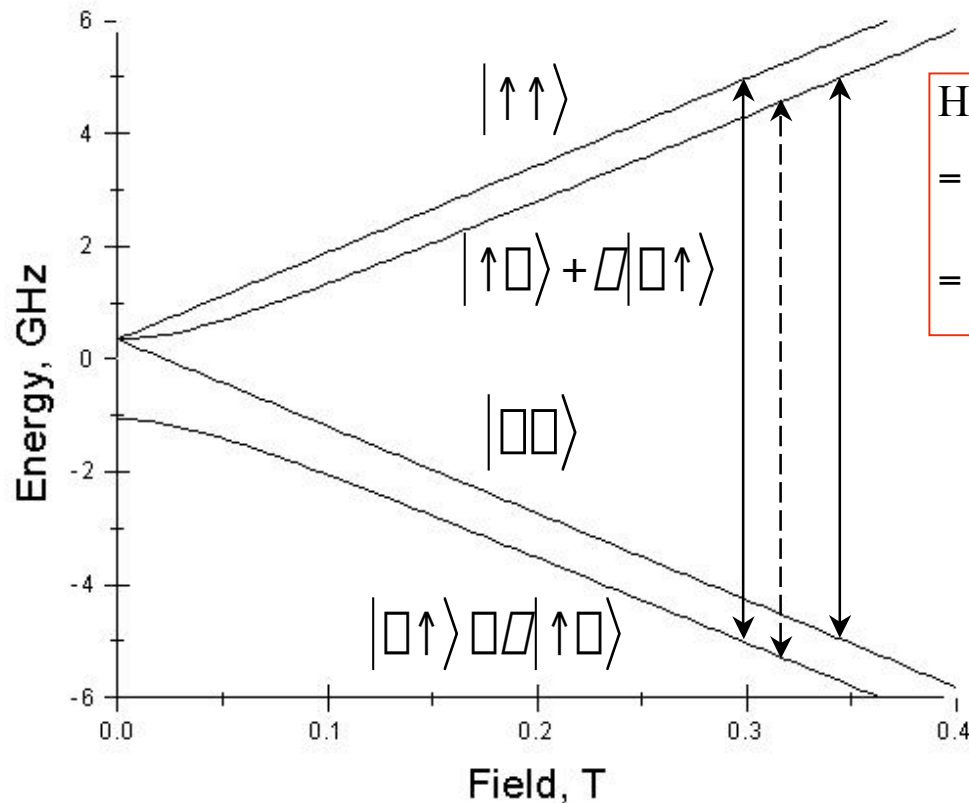
Figure 5.

ESR hyperfine structure  
for interactions with nuclei  
of different magnetic moments.



In figure 5, we show examples of the ESR signal from atomic hydrogen, atomic deuterium and atomic nitrogen from our Im-He solids. The hyperfine splittings are clearly displayed. It is straightforward to calculate these splittings from the Breit-Rabi equation.

Figure 6.



Treat  $H_{rf}$  as perturbation ( $H_{rf} \ll H_0$ ):

$$\begin{aligned} \text{Hamiltonian : } H_{rf}(t) &= H_{rf} \cos \omega t \\ &= \hbar g (S_x H_{1x} + S_y H_{1y} + S_z H_{1z}) \cos \omega t \\ &= g \hbar S_z H_{1z} + \frac{1}{2} g \hbar [(H_{1x} - iH_{1y}) S_+ + (H_{1x} + iH_{1y}) S_-] \end{aligned}$$

Use Fermi golden rule:

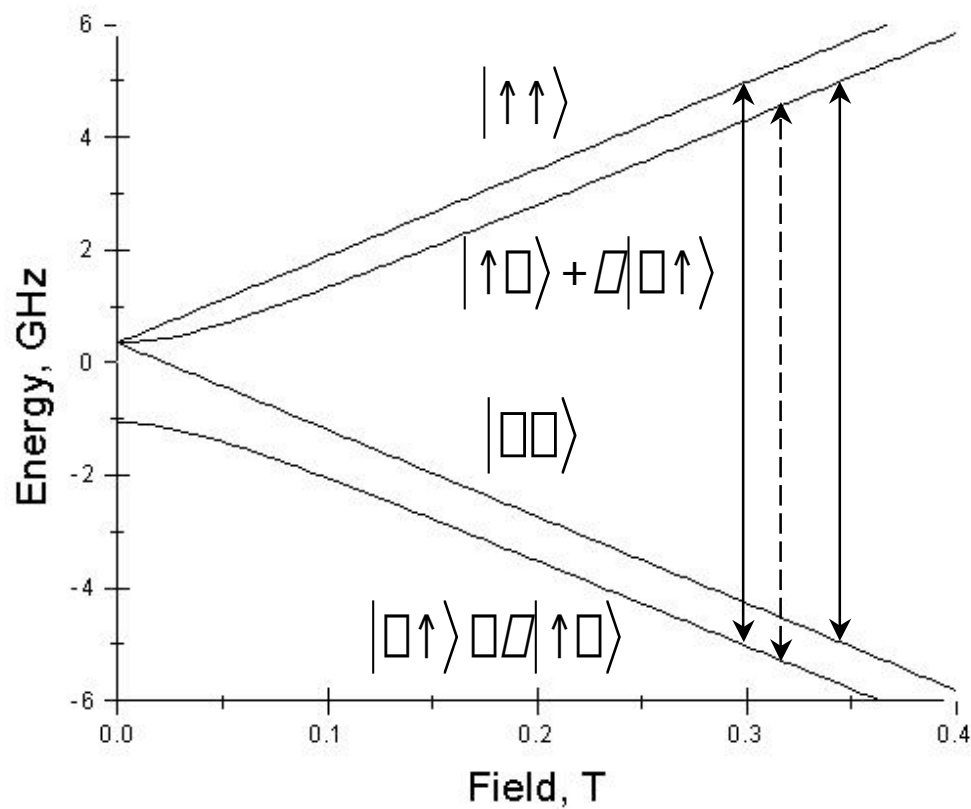
$$W(f \leftarrow i) = g(\omega) (2\hbar)^{-2} |\langle i | H_{rf}(t) | f \rangle|^2$$

$$W(|\uparrow\uparrow\rangle \leftarrow |\uparrow\downarrow\rangle \text{ or } |\downarrow\uparrow\rangle) = \text{const} \cdot |\langle \uparrow\uparrow | H_{rf} | \uparrow\downarrow \text{ or } \downarrow\uparrow \rangle|^2 = C |\langle \uparrow\uparrow | (H_{1x} - iH_{1y}) S_+ | \uparrow\downarrow \text{ or } \downarrow\uparrow \rangle|^2 = C (H_{1x}^2 + H_{1y}^2) 4$$

$$W(|\square\square\rangle \leftarrow |\uparrow\square + \square\downarrow\rangle) = C (H_{1x}^2 + H_{1y}^2) 4$$

$$W(|\uparrow\downarrow \text{ or } \downarrow\uparrow\rangle \leftarrow |\uparrow\square + \square\downarrow\rangle) = C H_{1z}^2 \omega^2$$

We shall be considering only H and D atoms in what follows. The Fermi contact interaction provides the dominant hyperfine splitting mechanism, since we are dealing with ground states which are spherically symmetric  $s$ -states. The hyperfine diagram is shown for the hydrogen atom in figure 6. The solid lines correspond to allowed transitions. The dashed line corresponds to a forbidden transition involving a simultaneous electron-proton spin flip.



$\square M_S = \pm 1$ , and  $\square M_I = 0$  for  $H_{rf} \perp z, H_0$   
 $\square M_S = \pm 1$ , and  $\square M_I = \mp 1$  for  $H_{rf} \parallel z, H_0$

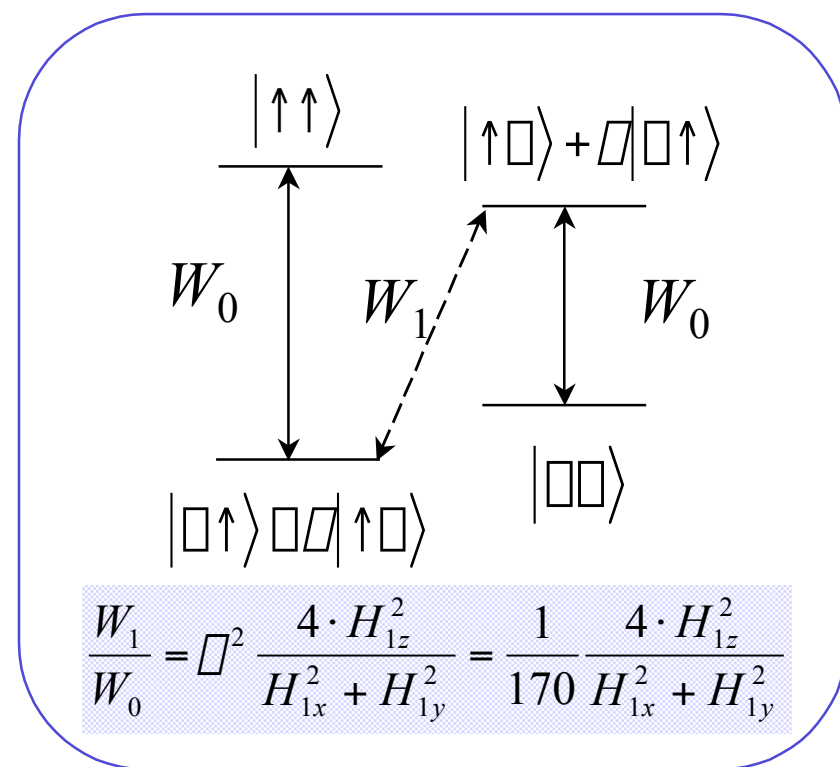


Figure 7.

A calculation of the relative intensities of the allowed and forbidden lines in the atomic hydrogen hyperfine spectrum is also shown in figure 6 with figure 7 showing the final results. The forbidden line intensity is  $\sim 200$  times smaller than the intensities of the allowed lines. Another noteworthy feature of these calculations is also indicated in fig. 6, where it is shown that the allowed lines respond to the microwave components  $H_{Ix}$  and  $H_{Iy}$  which are perpendicular to the applied steady magnetic field, whereas the forbidden line responds to  $H_{Iz}$  which is parallel to the applied steady magnetic field. Therefore the allowed lines exhibit transverse resonance, whereas the forbidden line corresponds to a longitudinal resonance.

ESR spectra of hyperfine structures of H and D atoms in  $\text{H}_2\text{-D}_2\text{-He}$  solid (mixture used -  $\text{H}_2\text{:D}_2\text{:He}=1\text{:4:100}$ ).

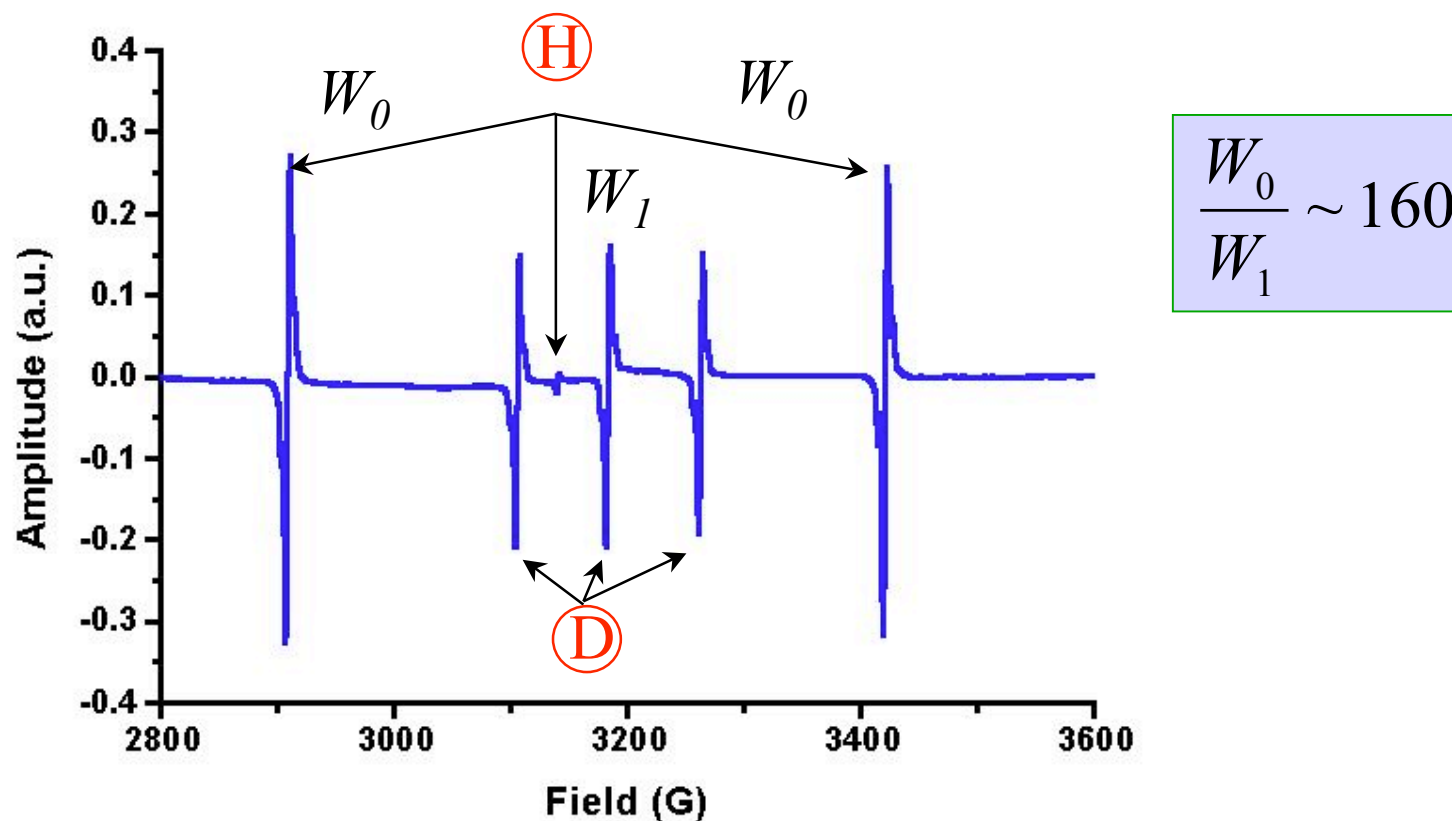


Figure 8.

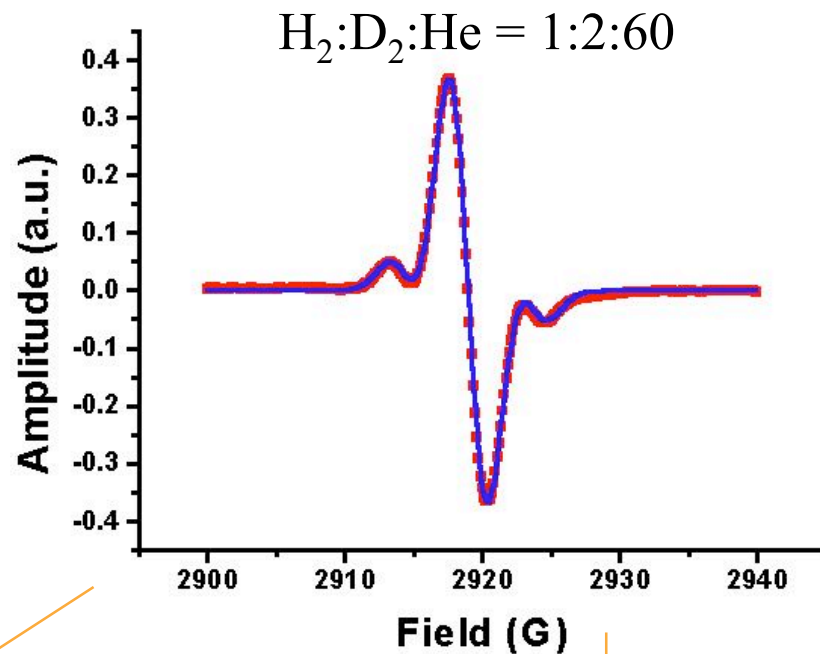
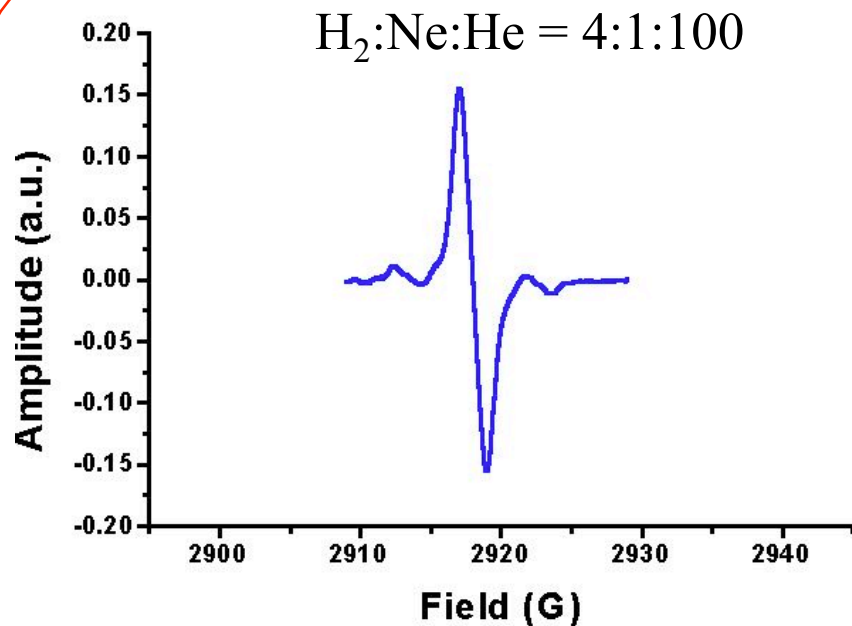
$\Delta H_{\text{firstH}} \text{ forbiddenH} \approx 232 \text{ G}$

from Breit - Rabi :  $\Delta H_{\text{firstH}} \text{ forbiddenH} \approx 235 \text{ G}$



The complete ESR spectra for hydrogen and deuterium atoms are shown in figure 8. The hydrogen lines are designated by the symbol **H** and the deuterium lines by the symbol **D**. The very small feature between the central and the left hand deuterium peak corresponds to the forbidden line of hydrogen. The ratio  $\sim 160$  roughly corresponds to the prediction given in figure 7.

Notice that the signals displayed in figure 8 are derivative signals which are derivatives of the intensities of the microwave absorption lines



Low field ESR lines from atomic H .

$$\Delta H_{\text{fitted}} = 4.3 \pm 0.1 \text{ G}$$

$$\Delta H_{\text{theory}} = H_0 \frac{g_N \Delta_N}{g_e \Delta_e} = 4.3 \text{ G}$$

$$\langle r \rangle_n = 0.73 (g_e \Delta_e / H)^{1/3} n^{1/6} (I_{\text{sat}} / I_{\text{main}})^{1/6}$$

$$\frac{I_{\text{sat}}}{I_{\text{main}}} \approx .11 \quad \langle r \rangle_n = 2.0 \text{ } ^\circ \text{ } 2.2 \text{ \AA}$$

for one - two protons near H atom

Figure 9.

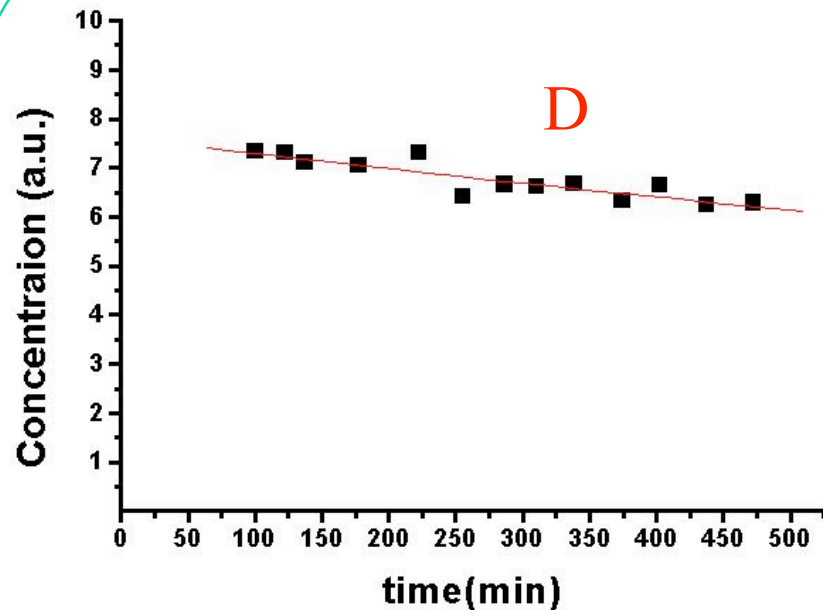
The H atom allowed lines form a doublet with a separation of order 500 gauss. A doublet is to be expected for a system with electron spin =  $1/2$  and nuclear spin =  $1/2$ . For the case of deuterium we have a triplet since the spin of the deuteron is unity. The spacing is narrower because the nuclear moment of the deuteron is a factor of  $\sim 7$  smaller than that of the proton.

If one looks carefully, one can observe small satellite lines on either side of both the allowed hydrogen signals and the allowed deuterium signals. These satellites come about as a result of the dipolar interactions between the electron spin of a hydrogen or deuterium atom and protons on nearby  $H_2$  or HD molecules. The satellite lines are better resolved when viewed on a larger scale as shown in figure 9.

Two different cases are shown in figure 9. In the left-hand frame, satellites for hydrogen atoms in a mixed H:H<sub>2</sub>:Ne:He impurity solid are shown. In this sample there is no deuterium and hence no HD or D<sub>2</sub> present. In the right hand frame we show satellite lines around the ESR line in atomic hydrogen embedded in a mixed H:D:H<sub>2</sub>:D<sub>2</sub>:He impurity helium solid. Deuteron flips do not give rise to resolvable satellites because of the small size of the deuteron magnetic moment. We note that the satellite shifts relative to the main lines are each separated by 4.4 gauss from the main ESR lines as would be expected for a proton spin flip in the external magnetic field. The intensities of the satellite lines can be used according to the theory of Trammell *et al.* (Phys. Rev. **110**, 630 (1958)) to calculate the separation between a neighboring hydrogen molecule and a hydrogen atom. For one or two protons near a hydrogen atom, this gives a separation of 1.9-2.2 Å indicating that a hydrogen atom typically will be found in association with a neighboring H<sub>2</sub> or HD molecule.

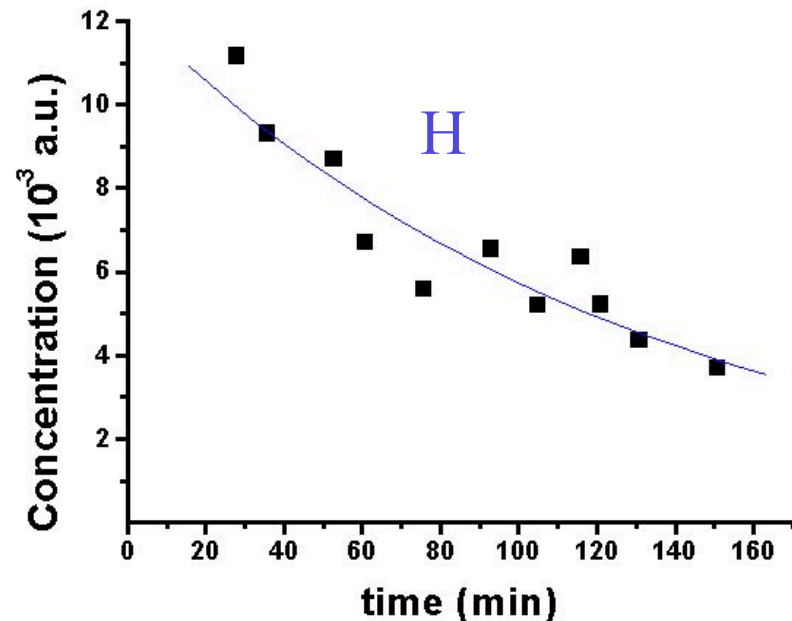


## Effect of storage of H and D in Im-He solid at T=1.4 K.



Mixture used  $D_2:He=1:20$

$$\tau = 2500 \pm 500 \text{ min}$$



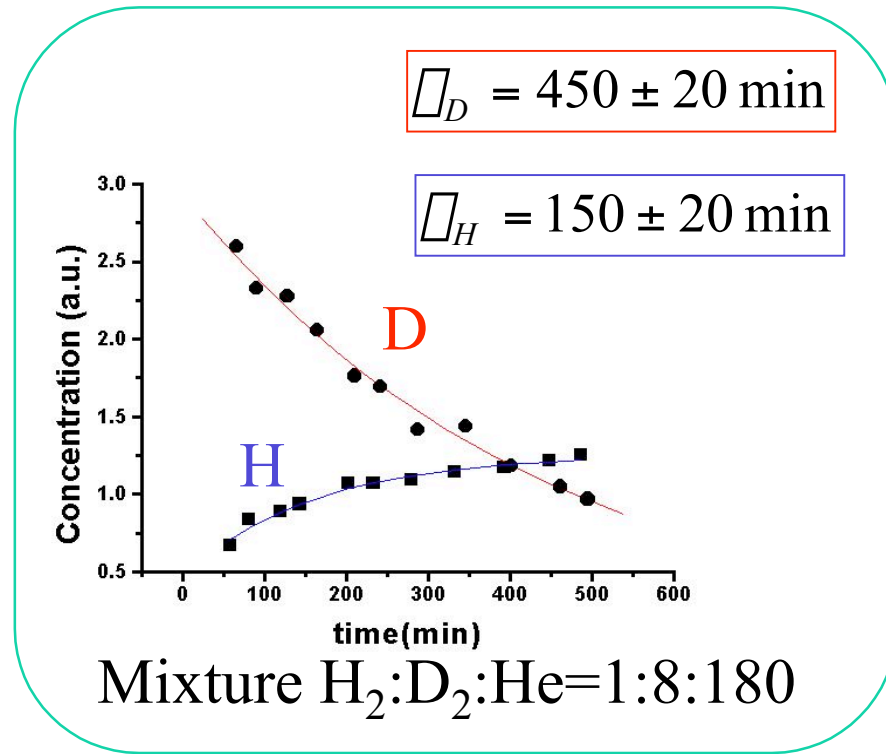
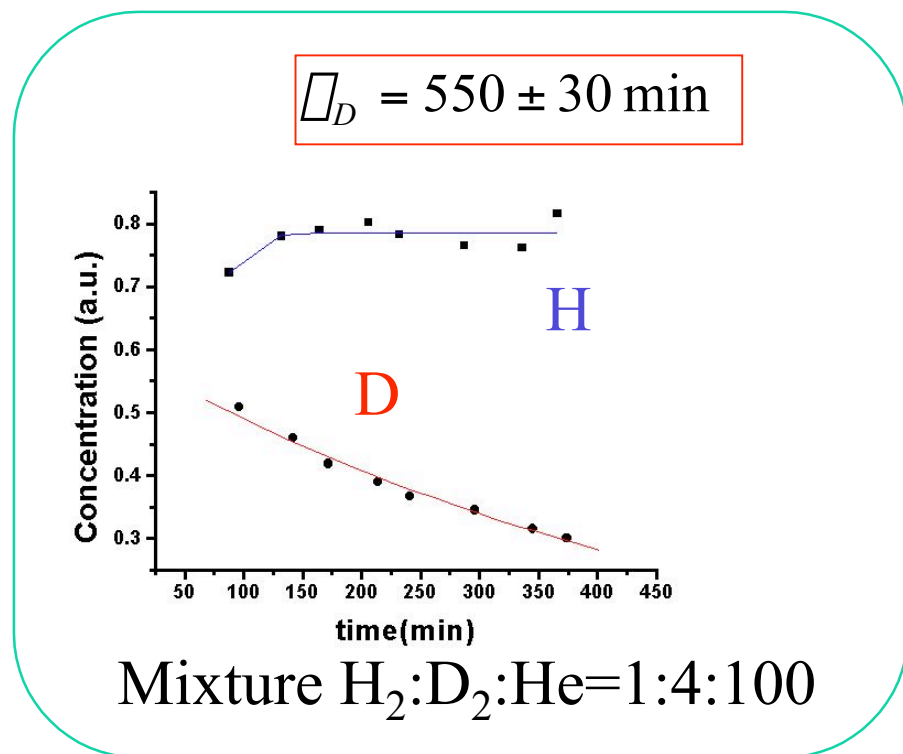
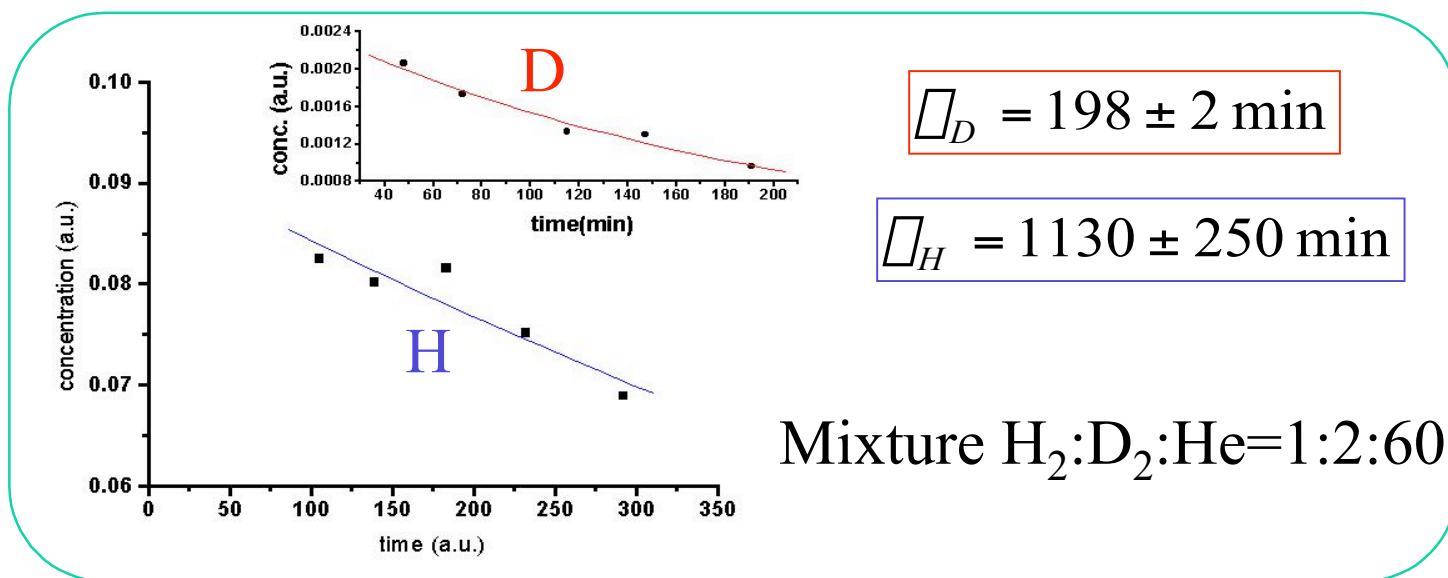
Mixture used  $H_2:Ne:He=1:4:100$

$$\tau = 130 \pm 20 \text{ min}$$

Figure 10.

We now consider the time evolution of samples of Im-He solids containing H atoms and/or D atoms as obtained from our ESR measurements. In the left hand frame of Figure 10, we show the slow decay of deuterium atoms in an Im-He sample containing only D and He atoms and D<sub>2</sub> molecules. For the initial gas mixture D<sub>2</sub>:He = 1:20, the time constant for the decay of the population of D atoms is 2500 minutes. This comes about as a result of the slow recombination of the D atoms to form D<sub>2</sub> molecules. In the right hand frame of Figure 10, we show the time evolution of H atoms in an Im-He solid containing H, H<sub>2</sub>, Ne and He. The decay of the H atoms is much faster with a time constant of about 130 minutes. The zero point motion of the H atoms is expected to be more rapid than that of D atoms, but the loss rate of H atoms far exceeds the rate expected from this effect alone.

Figure 11.





The behavior changes radically when hydrogen and deuterium atoms and molecules are simultaneously present in an impurity-helium solid. Results of the ESR intensity evolution for samples containing three different initial gas mixtures are shown in Figure 11. In the top frame corresponding to an initial gas mixture  $\text{H}_2:\text{D}_2:\text{He} = 1:2:60$ , the atomic deuterium is found to decay quite rapidly with a time constant of  $\sim 198$  minutes and the atomic hydrogen decays much more slowly with a time constant of  $\sim 1130$  minutes. In the lower left hand frame representing the time evolution of the H and D populations, respectively, the H atom population saturates and the D atom population declines with a time constant of 550 minutes for an initial gas mixture  $\text{H}_2:\text{D}_2:\text{He} = 1:4:100$ . The lower right hand frame represents the time evolution of a gas mixture with ratios  $\text{H}_2:\text{D}_2:\text{He} = 1:8:100$ . For this case the hydrogen atom population increases rapidly with a time constant of 150 minutes and the deuterium atom population decreases with a time constant of 450 minutes.

The data shown in Figure 11 can be explained by chemical reactions which occur at 1.35K. When a deuterium atom interacts with a hydrogen molecule, a temporary compound HDH molecule is formed, which in turn emits a hydrogen atom, leaving behind an HD molecule. The potential barrier for the formation of the compound HDH molecule is about 4000K, so a thermally activated chemical reaction at 1.35K can be ruled out. The process can only proceed if quantum mechanical tunneling takes place. Therefore, one of the reactions we are observing is the tunneling exchange reaction,  $D+H_2 \rightarrow H+HD$ . A second tunneling exchange reaction  $D+HD \rightarrow H + D_2$  can also take place. Takayanagi and Sato have studied exchange tunneling reactions involving hydrogen and deuterium. The various reactions and the reaction rate constants  $k$  are shown in the table. The rate for the first reaction  $D+H_2 \rightarrow H+HD$ , is more than two orders of magnitude faster than that from the second reaction  $D+HD \rightarrow H+D_2$ , as can be seen from the Table.

## Low Temperature Tunneling Reactions.

Calculated rate constant for the first order kinetics,  $k'$ .

- |     |   |                     |
|-----|---|---------------------|
| (1) | $\text{H}_2 + \text{D} \rightarrow \text{H} + \text{HD}$  | $5.4 \cdot 10^{12}$ |
| (2) | $\text{HD} + \text{D} \rightarrow \text{H} + \text{D}_2$  | $1.3 \cdot 10^{14}$ |
| (3) | $\text{DH} + \text{D} \rightarrow \text{D} + \text{HD}$   | $2.2 \cdot 10^{15}$ |
| (4) | $\text{D}_2 + \text{D} \rightarrow \text{D} + \text{D}_2$ | $3.7 \cdot 10^{18}$ |
| (5) | $\text{H}_2 + \text{H} \rightarrow \text{H} + \text{H}_2$ | $2.0 \cdot 10^{12}$ |
| (6) | $\text{HD} + \text{H} \rightarrow \text{H} + \text{DH}$   | $1.0 \cdot 10^{14}$ |
| (7) | $\text{DH} + \text{H} \rightarrow \text{D} + \text{H}_2$  | $< 10^{15}$         |
| (8) | $\text{D}_2 + \text{H} \rightarrow \text{D} + \text{DH}$  | $< 10^{15}$         |

$$\frac{d[\text{D}]}{dt} = k[\text{H}_2] \cdot [\text{D}] = k'[\text{D}]$$

Takayanagi and Sato, J. Phys. Chem. **92**, 2862 (1990)

By the time the Im-He solid has formed, this reaction has already partly depleted the supply of D atoms and has considerably enhanced the H atom population in the sample. The second reaction leads to a slower production of the H atom population which for some of the samples in Figure 10 cannot always keep pace with the recombination of H atoms into molecules. For the  $\text{H}_2:\text{D}_2:\text{He} = 1:4:100$  samples, the tunneling reaction and recombination reaction oppose one another leading to a steady population of H atoms.

In summary, we have studied the hyperfine spectra of atoms of deuterium and hydrogen via electron spin resonance in impurity-helium solids. We have found satellite lines around the resonance lines associated with spin flips of protons attached to  $\text{H}_2$  and HD molecules in the applied steady magnetic field. We have also observed a forbidden line in the hyperfine spectrum of hydrogen corresponding to simultaneous electron-proton spin flips. From the satellite intensities we have determined that hydrogen and deuterium atoms are usually found in close association with  $\text{H}_2$  or HD molecules. There is no evidence from our experiments of isolated H and D atoms. We have also observed the reaction kinetics of exchange tunneling reactions in Im-He solids for the first time.

We thank NASA for supporting this research via grant NAG8-1445.

## **Finite-size effects on the conductivity of He-4 near the superfluid transition**

Guenter Ahlers  
University of California  
Santa Barbara, CA 93106

We will present experimental data for the conductivity of He-4 near the superfluid transition in finite cylindrical and rectangular geometries and discuss the corresponding finite-size scaling functions.

This work was done by Edgar Genio, Daniel Murphy, Yuanming Liu, Fengchuan Liu, and Guenter Ahlers. The work was supported by NASA Grant NAG8-1429 and is part of the Flight Definition Project Boundary Effects on the Superfluid Transition (BEST).

## **Surface Physics with Helium Crystals in Microgravity**

Alex Babkin  
University of New Mexico  
Albuquerque, NM 87111

We report on the latest progress in our ground based morphological studies of helium crystals. We discuss the objectives of the experimental studies, their significance and relevant experimental techniques. We also report on the progress in theoretical studies of the subject. Our new experimental set-up that is currently under construction is aimed to help solving a number of experimental problems that will help to design a flight experiment more precisely.

# Critical Casimir Forces in Systems of Different Universality Class

R. Garcia and M. H. W. Chan,

*Physics Department, 104 Davey Lab., Pennsylvania State University, University Park, PA 16802*

---

## Abstract

Dielectric constant measurements of helium films adsorbed on Cu electrodes provide evidence for the existence of the critical Casimir force near the superfluid transition in  $^4\text{He}$  and near the tricritical point in  $^3\text{He}$ - $^4\text{He}$  mixtures. This force, an analog of the Casimir force in electromagnetism, provides important information on critical finite size effects. In pure  $^4\text{He}$ , we find the force is attractive but near the tricritical point the force appears repulsive, a change due to the extraordinary boundary conditions at the tricritical point. We have begun construction of a Casimir pressure gauge that is capable of directly measuring the critical Casimir force near critical points of systems belonging to many different universality classes.

---

## 1. Introduction

When a fluid undergoing a phase transition is confined between two flat surfaces, there is a correction  $E(d)$  to the free energy per unit area that depends on the separation  $d$  between the surfaces. This correction affects the specific heat, a second derivative of the free energy, and also manifests itself in an effective force per unit area  $F = -(\partial E/\partial d)_T$  between the surfaces confining the film. Such effects can be readily verified near a critical point when the diverging correlation length  $\xi$  of the fluctuations in the order parameter becomes comparable to the film thickness  $d$ . Fisher and deGennes[1,2] propose a universal form for the finite-size correction near a critical point

$$E(d) = \frac{k_B T_c}{d^2} \Theta(d/\xi) \quad (1)$$

where  $\xi = \xi_{o\pm} |t|^{-\nu}$  and the reduced temperature  $t = T/T_c - 1$ .  $\Theta$  is a scaling function that is predicted to depend on the universality class and the boundary conditions of the order parameter[2,4-7]. The corresponding

$$F = \frac{k_B T_c}{d^3} \vartheta(d/\xi) \quad (2)$$

where  $\vartheta(d/\xi) = 2\Theta - d\partial\Theta/\partial d$ [4].  $F$  is called the critical Casimir force due to a formal analogy with the Casimir force in electromagnetism[3,4]. While the Casimir force is due to the confinement of zero point fluctuations in

the electromagnetic field, the critical Casimir force is due to confinement of fluctuations in the order parameter.

Evidence for Eq.1 is found, for example, in the observed finite-size correction to the specific heat of helium films. The maximum of the film specific heat occurs when the scaling variable  $x = td^{1/\nu} = (\xi_o d/\xi)^{1/\nu} \simeq 9$ [4,8], consistent with finite-size scaling(Eq.1). Evidence of the critical Casimir force has also been reported in certain adsorbed binary fluid mixture films[9].

In our experiments, we have sought to observe the effect of the critical Casimir force on liquid helium films adsorbed on Cu substrates near the lambda point. In this case, superfluid fluctuations are confined between the film-substrate and film-vapor interfaces. An experiment by Dionne and Hallock in 1989 shows an anomaly in the helium film thickness suggestive of such a force[10]. Our measurements have found an attractive critical Casimir force in  $^4\text{He}$  films near the superfluid transition[11] and a repulsive Casimir force near the tricritical point TP of  $^3\text{He}$ - $^4\text{He}$  mixtures[12]. These measurements show the critical Casimir effect in adsorbed films, but we would also like to observe it when the fluid is bound by two solid walls, because then the boundary conditions will be different. A Casimir pressure gauge is presently being constructed that will be capable of directly measuring the critical Casimir force

14 July 2002



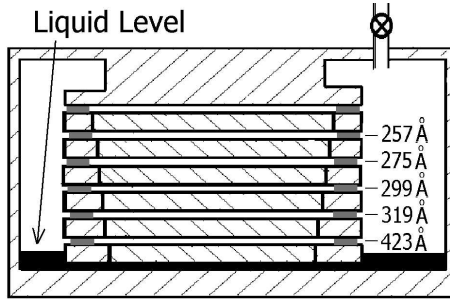


Fig. 1. A schematic of the cell used to study films of pure  $^4\text{He}$  and  $^4\text{He}$  with small amounts of  $^3\text{He}$  added. The adsorbed film thickness decreases the higher up in the cell we go. The bulk liquid helium at the bottom of the cell is shown as a black layer. The height  $h$  above the bulk liquid for the various capacitors ranges between 2 mm and 14 mm, giving adsorbed film thicknesses between 423 and 257 Å.

in this geometry. It will also be capable of measuring the force near liquid-vapor critical points.

## 2. $^4\text{He}$ films near the superfluid transition

In Fig. 1, we show a schematic of the experimental cell we used for films of pure  $^4\text{He}$  and dilute mixtures. There are six capacitor plates forming 5 capacitors at different heights  $h$  above the bulk liquid. In accord with the theory of wetting films[13] and finite-size scaling[2,5], the thickness of a helium film wetting a Cu substrate a height  $h$  above the bulk liquid is given by

$$Mgh = \alpha/d^3 + V k_B T_c \vartheta/d^3 \quad (3)$$

In the first term,  $g$  is the gravitational acceleration,  $h$  the height above the bulk liquid, and  $M$  the mass per atom of the bulk liquid. In the second term,  $\alpha = 2600\text{K}\text{\AA}^3/(1 + d/193\text{\AA})$  is a coefficient characterizing the van der Waals attraction of the helium atom to the Cu substrate[13]. The last term is the predicted chemical potential difference between the film and bulk due to the critical Casimir force, where  $V$  is the specific volume per atom in the bulk liquid[2,4,5,11].

Far from the superfluid transition, it is expected that  $\vartheta \rightarrow 0$ [2,4,5,7] and the film thickness  $d$  at a given  $h$ , according to Eq.3, is determined only by a competition between the van der Waals attraction of the liquid to the substrate and gravity which pulls the liquid to the bottom of the cell. The film is progressively thinner on surfaces higher up in the cell. Close to  $T_c$ , the critical Casimir force modifies the effective interaction with the substrate, so that if  $\vartheta < 0$ , the liquid film will thin, producing a dip.

Near the superfluid transition in  $^4\text{He}$  films, indeed, we observe a dip in the film thickness. In Fig. 2, we show  $\vartheta$  calculated from the measured thickness for films using Eq.3 for different  $h$ [11]. Evidently,  $\vartheta < 0$  so that the

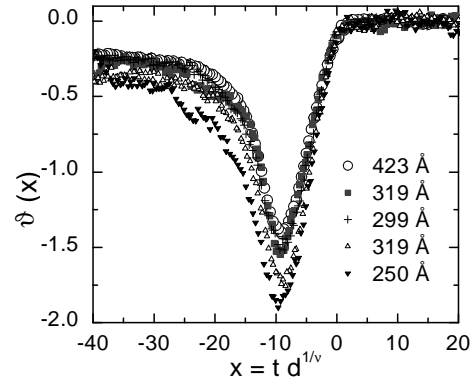


Fig. 2. The scaling function  $\vartheta$  vs the scaling variable  $x = t d^{1/\nu} = (\xi_o d/\xi)^{1/\nu}$  where  $\nu = 0.6705$ [14]. The 5 different curves correspond to the 5 different  $h$  in Fig. 1. The uncertainty in  $\vartheta$  is about 20%.

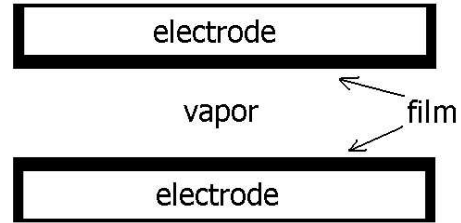


Fig. 3. Schematic of capacitor showing helium films (black) adsorbed onto the electrodes.

critical Casimir force is attractive. Such an attractive Casimir force occurs whenever the boundary conditions are the same at both of the confining interfaces[4–7,15]. For pure  $^4\text{He}$  this makes sense because the order parameter vanishes at the boundaries, consistent with Dirichlet boundary conditions at both the film-vapor and film-substrate interfaces. In Fig. 2, the minimum of  $\vartheta$  occurs at the same value of  $d/\xi$  for films of different thickness. This is expected due to the  $d/\xi$  dependence of  $\vartheta$ . However, the curves do not fall perfectly upon each other. Various explanations have been proposed for this lack of collapse, including a systematic error in the determination of  $d$ [7,11,15]. Further work, both experimental and theoretical, is needed to clarify this issue. In the small region above  $T_c$ , the measured  $\vartheta$  is consistent with an  $\epsilon$  expansion calculation of  $\vartheta$  for Dirichlet boundary conditions[4,11]. However, no appropriate calculations exist for below  $T_c$ [16,20].

## 3. Capacitance measurement of adsorbed films

In the capacitance technique we used to measure  $d$ , the liquid film is adsorbed on the electrodes of a parallel plate capacitor, as shown schematically in Fig.3. To

calculate the film thickness from the measured capacitance  $C$ , we assume that the capacitances due to the adsorbed film and due to the vapor between the films add in series, obtaining

$$d = \frac{1}{2} G (1/\epsilon - 1/\epsilon_{film}) / (1/\epsilon_{vapor} - 1/\bar{\epsilon}_{film}) \quad (4)$$

where  $G$  is the gap between the plates,  $\epsilon_{film}$  is the dielectric constant of the film, and  $\epsilon_{vapor}$  is the dielectric constant of the vapor[11]. The effective dielectric constant  $\epsilon = C/C_o$  where  $C_o$  is the capacitance when all the fluid is removed. In order to prevent capillary condensation of the liquid in the capacitor gap, we must use a large gap  $G = 0.2mm$ . Because of the large gap, a  $500\text{\AA}$  thick helium film adsorbed on the capacitor plates contributes only  $\sim 5 \times 10^{-5}$  to  $\epsilon$  while the vapor between the plates contributes  $\sim 4 \times 10^{-4}$ . We calculate  $\epsilon_{vapor}$  from the saturated vapor density via the Clausius-Mossotti equation, including a correction for the second virial coefficient.

While the capacitance technique gives an accurate measurement of  $\Delta d$ , we have found in practice that it is not good at determining the absolute value of  $d$ . There is no dip or peak-like anomaly in  $\epsilon_{vapor}$  so we are sure that the anomaly in Fig.2 is due to something in the film and not an effect in the vapor. However, because the second virial coefficient is not known in the temperature range of our experiments, this contributes to our uncertainty in the absolute value of  $d$ . More significantly, stray capacitances and capillary condensation in scratches on the surface produce temperature-independent errors in  $\epsilon$ , large in comparison to the contribution to  $\epsilon$  of the adsorbed film[10,11]. To correct for these errors, we have adjusted the data by subtracting a constant so that  $d$  calculated using Eq.4 agrees with  $d$  predicted from Eq. 3 far above  $T_c$  when the critical Casimir effect is expected to be negligible[2,4,5]. We, of course, would prefer not to make such an adjustment, but it was necessary in order to interpret our data sensibly[11].

#### 4. $^3\text{He}$ - $^4\text{He}$ mixture films near the tricritical point

We have also measured the critical Casimir effect in  $^3\text{He}$ - $^4\text{He}$  mixture films. The mole fraction of  $^3\text{He}$  in the liquid  $X = n_3/(n_3 + n_4)$  where  $n_3$  is the number of moles of  $^3\text{He}$  and  $n_4$  is the number of moles of  $^4\text{He}$ . In pure  $^4\text{He}$  films and in  $^4\text{He}$  with small amounts of  $^3\text{He}$  added ( $X < 0.6$ ), the critical Casimir force is observed to be attractive, i.e  $\vartheta < 0$ , producing a dip in the film thickness centered just below the bulk superfluid transition temperature. As  $^3\text{He}$  is added, the dip follows the superfluid transition to lower temperature, becoming progressively broader but remaining about

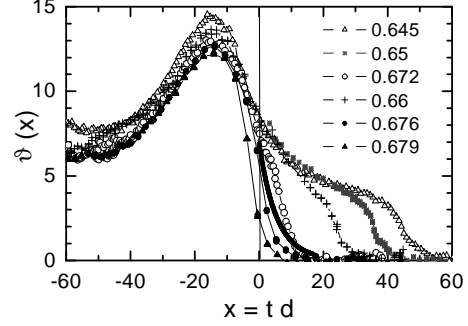


Fig. 4. The scaling function  $\vartheta$  vs the scaling variable  $x = td^{1/\nu}$  where  $\nu = 1$  along a path of constant  $X$  near TP[17,18]. The different curves correspond to 5 different mole fractions  $X$  close to the tricritical point. For  $X < 0.672$ , we observe a shoulder-like thickening associated with the superfluid onset in the bulk liquid and a peak associated with phase separation. As  $X \sim 0.672$  is approached, the shoulder and peak merge.

the same magnitude as for pure  $^4\text{He}$ [11]. For  $X > 0.6$ , however, Laheurte et al. determined that the mixture film close to the substrate surface, enriched in  $^4\text{He}$ , becomes superfluid, even before the rest of the film or bulk liquid is superfluid[19]. Because of this superfluid layer, different boundary conditions are present close to TP and the critical Casimir force there is expected to be repulsive rather than attractive[5,6,20].

In Fig. 4, we show the measured  $\vartheta$  for a single height (2 mm) above the bulk liquid and various  $X$  close to tricritical mole fraction  $X_t$ . We use Eq. 3, but are careful to substitute for  $M$  and  $V$  the corresponding quantities for the bulk liquid mixture[12]. Evidently,  $\vartheta > 0$  as expected, consistent with a repulsive force. For  $X < 0.672$ , we observe a shoulder-like thickening associated with the superfluid onset in the bulk liquid and a peak associated with phase separation. As TP ( $X \sim 0.672$ ) is approached, the shoulder and peak merge.

The thick line in Fig. 4 shows a theoretical calculation of  $\vartheta$  near the tricritical point of the Ginzburg-Landau XY model, where the order parameter is assumed to be zero at one interface and nonzero at the other[20]. While the agreement between the theoretical and measured  $\vartheta$  seems quite good, the agreement may be fortuitous, considering the 5-20% experimental uncertainty in  $\vartheta$ [12]. At present, there is no theory describing how the critical Casimir force evolves as  $X$  is varied from  $X_t$ . Further work is also necessary to study in detail how the critical Casimir force evolves near  $X \sim 0.6$  and in more dilute mixtures.

#### 5. Casimir Pressure Gauge

The capacitance measurement of adsorbed films has allowed us to measure critical Casimir force indirectly

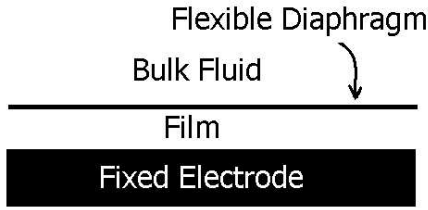


Fig. 5. A schematic drawing showing a flexible diaphragm (black line) and a fixed electrode (black bar). An attractive critical Casimir force will pull the diaphragm towards the electrode, increasing the measured capacitance between them.

by its effect on the equilibrium film thickness. A serious drawback of this technique, noted above, is that it is not a good for measuring the absolute value of the film thickness. The uncertainty in the absolute value of  $d$  is about 20%. Also, for mixtures near TP, we are limited to having only 1 capacitor in the vapor phase, a smaller cell being necessary in order to reduce the equilibration time to about 1 hour per point. Because we have only 1 capacitor, we are limited to measuring a single height above the bulk liquid. Another disadvantage is that we are limited to thinner films (500 Å or less). If we try to get much thicker films by reducing  $h$  below 2 mm, then the films adsorbed on the two capacitor electrodes will no longer be the same thickness.

We have recently begun construction of a Casimir pressure gauge in order to directly measure the critical Casimir force. This gauge does not suffer from any of the drawbacks inherent in the capacitance measurement of adsorbed films. Even more importantly, it will allow us for the first time to also measure the critical Casimir force near the liquid-vapor critical point, where e.g. above  $T_c$  there is no liquid film whatever.

In Fig. 5, we show a schematic side-view of the sensor. The diaphragm and fixed electrode are completely submerged in the critical fluid. Because the boundary conditions for the order parameter are identical at the flexible diaphragm and at the fixed electrode, the critical Casimir force is expected to be attractive. Thus, as we approach  $T_c$ , the critical Casimir force will pull the diaphragm closer to the fixed electrode. This increases the capacitance between the diaphragm and fixed electrode. For a 1 micron thick film,  $F \sim -3 \times 10^{-5} Pa$ . This will translate into a  $\sim 0.1\%$  increase in  $C$ , while even a  $1 \times 10^{-7}$  change in  $C$  is readily measurable.

In Fig. 5, the bulk and film spaces on either side of the diaphragm are connected so that the fluid can easily flow between them. This cancels out the background pressure of the fluid unrelated to the critical Casimir force.

For these measurements, gravitational rounding will present a significant encumbrance, limiting how close the bulk liquid can be made to approach the criti-

cal point. Near TP in  $^3\text{He}$ - $^4\text{He}$  mixtures, for example, gravity will cause the bulk liquid to be enriched in the denser  $^4\text{He}$ . The width of the critical Casimir effect scales with the scaling variable  $x = td$ . For a 1 micron thick film, the Casimir effect near TP will be about 1 mK wide in temperature. Therefore, we will need to take points  $\sim 50 \mu K$  apart. If we are this close to  $T_t$  and the cell is 1 mm in height, then  $X$  will be  $\sim 0.01$  higher at the bottom of the cell than at the top. Similar considerations apply near the liquid-vapor critical point.

## Acknowledgments

We thank H. Meyer for providing unpublished pressure data used in some of our calculations. We thank M. Krech and G. Williams for providing their calculations of  $\vartheta$  ahead of publication. And we also thank M. Cole, K. Knorr, and N. Mulders for informative discussions. This work was supported by NASA's Office of Biological and Physical Research under NAG8-1761.

## References

- [1] M. E. Fisher, in *Critical Phenomena*, Proc. 51st "Enrico Fermi" Summer School, Varenna, edited by M. Green (Academic, NY, 1971), p. 1; V. Privman and M.E. Fisher, Phys. Rev. B **30**, 322 (1984).
- [2] M. E. Fisher and P.-G. de Gennes, C. R. Acad. Sci. Paris, Ser. B **287**, 209 (1978).
- [3] H. B. G. Casimir, Proc. K. Ned. Akad. Wet. **51**, (1948) 793; S. K. Lamoreaux, Phys. Rev. Lett. **78**, (1997) 5; U. Mohideen and A. Roy, Phys. Rev. Lett. **81**, 4549 (1998).
- [4] M. Krech and S. Dietrich, Phys. Rev. Lett. **66**, (1991) 345; **67**, (1991) 1055; Phys. Rev. A **46**, 1922 (1992); Phys. Rev. A **46**, 1886 (1992); J. Low Temp. Phys. **89**, 145 (1992).
- [5] M. P. Nightingale and J. O. Indekeu, Phys. Rev. Lett. **54**, 1824 (1985); J. O. Indekeu, M. P. Nightingale, W. V. Wang, Phys. Rev. B **34**, 330 (1986); K. K. Mon and M. P. Nightingale, Phys. Rev. B **35**, 3560 (1987); J. O. Indekeu, J. Chem. Soc. Faraday Trans. II **82**, 1835 (1986).
- [6] U. Ritschel and M. Gerwinski, Physica A **243**, 362 (1997).
- [7] M. Krech, J. Phys.: Condens. Matter **11**, R391 (1999).
- [8] S. Mehta and F. M. Gasparini, Phys. Rev. Lett. **78**, (1997) 2596; S. Mehta et al., J. Low Temp. Phys. **114**, 465 (1999); J.A. Nissen et al., J. Low Temp. Phys. **92**, 353 (1993); V. Dohm Physica Scripta **T49**, 46 (1993).
- [9] A. Mukhopadhyay and B. M. Law, Phys. Rev. Lett. **83**, 772 (1999); Phys. Rev. E **62**, 5201 (2000).
- [10] R. J. Dionne and R. B. Hallock, in *Quantum Fluids and Solids-1989*, edited by G. Ihás and Y. Takano, AIP Conf. Proc. No. 194 (AIP, New York 1989), p. 199.
- [11] R. Garcia and M.H.W. Chan, Phys. Rev. Lett. **83**, 1187 (1999); Physica B **280**, 55 (2000).
- [12] R. Garcia and M.H.W. Chan, Phys. Rev. Lett. **88** 086101 (2002); J. Low Temp. Phys. **121**, 495 (2000).

- [13] I. E. Dzyaloshinskii, E. M. Lifshitz and L. P. Pitaevskii, Adv. Phys. **10**, 165 (1961); E. Cheng and M. W. Cole, Phys. Rev. B **38**, 987 (1998); G. Vidali et al., Surf. Sci. Rep., **12**, 122 (1991); S. Rauber et al., Surf. Sci., **123**, 173 (1982).
- [14] L.S. Goldner and G. Ahlers, Phys. Rev. B **45**, 13129 (1992).
- [15] H. Li and M. Kardar, Phys. Rev. Lett. **67**, (1991) 3275; Phys. Rev. A **46**, 6490 (1992).
- [16] G.A. Williams, Preprint submitted to Physica B.
- [17] G. Ahlers and D. S. Greywall, Phys. Rev. Lett. **29**, 849 (1972); H. A. Kierstead, J. Low Temp. Phys. **35**, 25 (1979); E. H. Graf, D. M. Lee and J. D. Reppy, Phys. Rev. Lett. **71**, 226 (1967).
- [18] G. Goellner, et al., J. Low Temp. Phys. **13**, (1973) 113 ; E. K. Riedel et al., J. Low Temp. Phys. **22**, 369 (1975); M. G. Ryschekewitsch and H. Meyer JLTP **35**, 103 (1979); P. Leiderer, D. R. Watts, and W. W. Webb, Phys. Rev. Lett. **33**, 483 (1974); H. Meyer, Private communication.
- [19] J.-P. Laheurte, J.-P. Romagnan and W.F. Saam, Phys. Rev. B **15**, 4214 (1977); J. Low Temp. Phys. **30**, 425 (1978).
- [20] M. Krech, private communication.

## **Multiple-channel superconducting quantum interference device controller using a digital signal processor**

Benjie Limketkai, Jim Granger, Mark Weilert, and Inseob Hahn  
Jet Propulsion Laboratory,  
California Institute of Technology  
Pasadena, California 91109-8099

We report on the design, performance and limitations of an improved multiple SQUID controller base upon a single digital signal processor (DSP). The main DSP program flux-locked-loop algorithm is written in a machine language to minimize the execution time. We added a simple frequency converter to improve the performance of the controller that was built using a commercially available sensor and a preamplifier. The noise level of the dc SQUID controller system is comparable with the commercial analog system,  $\sim 4 \mu\text{V}/\text{Hz}^{1/2}$  at 100Hz. The current system could control up to 5 SQUID channels.

## **New measurement technology for thermometry and heat flux control**

Robert Duncan  
University of New Mexico  
Albuquerque, NM 87131-1156

New measurement technologies have been developed to advance thermometry and heat flux control for low-temperature, fundamental physics experiments. The DYNAMX and CQ experiments plan to use a new layered aluminum cell endcap design that will spread heat from a small surface-mount resistor uniformly across a 2.5 cm cell diameter using only a 0.5 cm thick endcap. The bubble chamber mounted on the top endcap is thermally isolated so that the surface area within the bubble chamber does not contribute to the heat flow out of the He-II, assuring uniform heat flux through the cross section of this endcap.

Thin films and microstructures of dilute Mn magnetic ions in Pd have been prepared by sputtering bulk PdMn material on machined glass and sapphire substrates for use in spatially resolved thermometry and bolometry. The thermal sensitivity of these thin film devices have been measured as a function of magnetic field and temperature, showing complex thermomagnetic behavior that varies with the film thickness. The thermomagnetic performance of these films is easily controlled and non-hysteretic, so that these devices may facilitate many new experiments in the study of the quantum fluids.

This work has been performed in collaboration with D.A. Sergatskov, R.C. Nelson, A.V. Babkin, S.T.P. Boyd, T.D. McCarson, A.M. Churilov, R.A.M. Lee, D.L. Goodstein, and A. Chatto, and is supported by the Fundamental Physics Discipline within the Microgravity Science Office of NASA.



# Oscillatory and Relaxation Transient Studies in the Convection of Supercritical $^3\text{He}$

Horst Meyer and Andrei B. Kogan\*

*Department of Physics, Duke University, Durham, NC 27708-0305.*

*\*present address: Department of Physics, MIT, Cambridge, MA 02139-4307.*

We analyze the temporal profile  $\Delta T(t)$  of the temperature difference, measured across a very compressible supercritical  $^3\text{He}$  fluid layer in its convective state. The experiments were done along the critical isochore in a Rayleigh-Bénard cell after starting the vertical heat flow  $q$ . For  $q > q_{ons}$  (“convection onset”), the transient  $\Delta T(t)$  under given conditions of  $q$  and  $\epsilon \equiv (T - T_c)/T_c$ , with  $T_c = 3.318\text{K}$ , shows a damped oscillatory profile with period  $t_{osc}$  modulating a smooth base profile. The latter forms the tail of the transient which relaxes exponentially to the steady-state  $\Delta T(\infty)$  with a time constant  $\tau_{tail}$ . The scaled times  $t_{osc}/t_D$  and  $\tau_{tail}/t_D$  from all the data could be collapsed onto two curves as a function of the Rayleigh number over  $\sim 3.5$  decades. Here  $t_D$  is the characteristic thermal diffusion time.

While a substantial amount of recent research has dealt with pure fluid convection in a Rayleigh-Bénard cell in a quasi steady-state (See for instance [1]), comparatively little study has been done on the transient behavior after the heat flow  $q$  has been started across a fluid layer. Here we study the temporal profile of the temperature drop  $\Delta T(t)$  across the fluid layer (thickness  $L=0.106\text{cm}$ , aspect ratio 57) of a very compressible fluid, supercritical  $^3\text{He}$ , before the steady state value  $\Delta T \equiv \Delta T(\infty)$  is reached. Our study is concerned with  $\Delta T > \Delta T_{ons}(\epsilon)$ , the convection onset value, and  $\epsilon \equiv (T - T_c)/T_c$  where  $T_c = 3.318\text{ K}$ . The range along the critical isochore is  $5 \times 10^{-4} \leq \epsilon \leq 0.2$ .

Experiments on the convective behavior of  $^3\text{He}$ , both transient and steady state, were recently reported [2] at Rayleigh numbers  $Ra < 5 \times 10^8$ . In the measurements of  $\Delta T(t)$



at a given  $\epsilon$  and heat flow  $q$ , the temperature of the upper plate was kept constant and that of the bottom plate was left floating. A detailed discussion on the fulfillment of the Boussinesq criteria in the experiments is given in ref [2]. The present paper describes an analysis of some of the transients and their characteristic times, to be compared elsewhere [3] with predictions by Onuki and his group [4].

Under certain conditions, to be described below, damped oscillations of  $\Delta T(t)$  with a period  $t_{osc}(q, \epsilon)$  were observed for  $\epsilon \geq 9 \times 10^{-3}$ , following the initial sharp rise from zero after  $q$  is turned on. These result from a combination of density and high compressibility that leads to strong thermo-acoustic phenomena which have been shown responsible for very fast temperature homogenisation inside the fluid layer [5]. The mechanism involved for the accelerated energy transfer has been named “piston effect”, which results from the hot (or cold) boundary layer that forms where a heat is suddenly applied (or withdrawn). This layer then acts as a piston that isentropically compresses (decompresses) the bulk of the fluid, thus raising (lowering) the temperature in a homogeneous way, as has been described in refs [6,7]. A sequence of hot and cold piston effects produces maxima and minima in  $\Delta T(t)$  until a steady-state regime is reached.

After activation of the heat flow, the observed  $\Delta T(t)$  pattern is as follows: For a heat flow  $q < q_{ons}$ , (convection “onset”),  $\Delta T(t)$  tends smoothly to  $\Delta T(\infty)$  (see Fig.1c) with a relaxation time  $\tau_0$  as discussed in ref. [2]. This transient of the non-convective fluid is observed in zone F of Fig.2, the boundary of which is known from ref. [2]. As  $q$  is increased beyond  $q_{ons}$ , the transient shows first an overshoot - or truncated oscillation (see Fig.1b). This behavior is observed in zone A of Fig.2. Above a certain range of  $q$ ,  $\Delta T(t)$  then shows a damped oscillatory behavior (see Fig.1a). This is observed in zone B of Fig.2, near its lower boundary. The profile  $\Delta T(t)$  becomes more complex in zone B with increasing  $q$  but can be described in terms of two superposed components, after the sharp initial rise: a) a sharp peak followed by a smooth base profile with a minimum beyond which  $\Delta T(t)$  tends exponentially to  $\Delta T(\infty)$  from below with a relaxation time  $\tau_{tail}(q, \epsilon)$ , b) damped oscillations of period  $t_{osc}(q, \epsilon)$ , modulating the smooth base profile. The visibility and relative amplitude

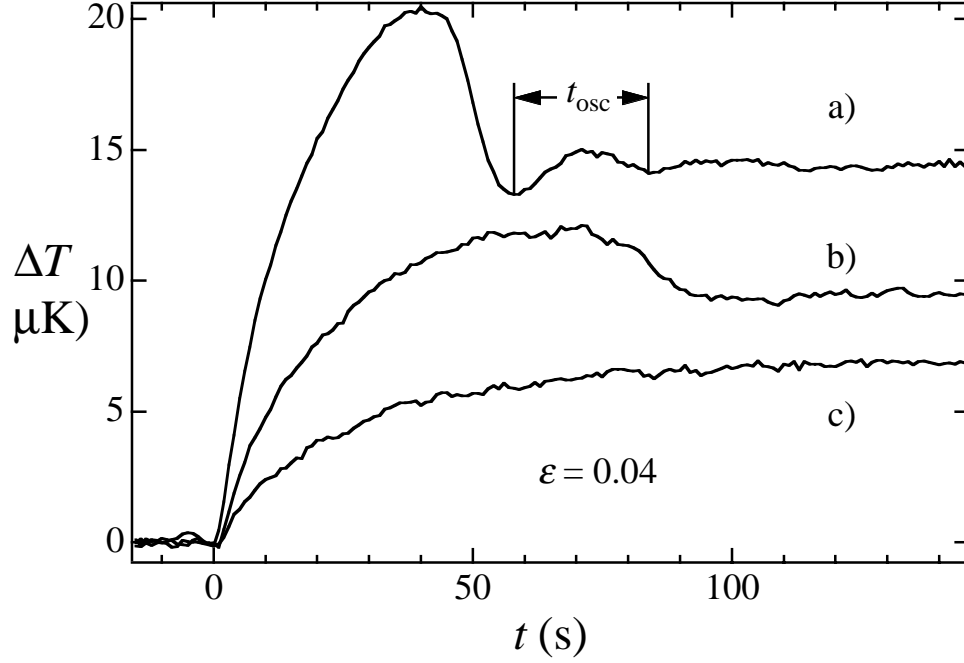


FIG. 1. Profiles  $\Delta T(t)$  at  $\epsilon = 0.04$  for several values of  $q$  (in  $10^{-8}$  W/cm $^2$ ) : a) 5.17, b) 2.53, c) 1.21.

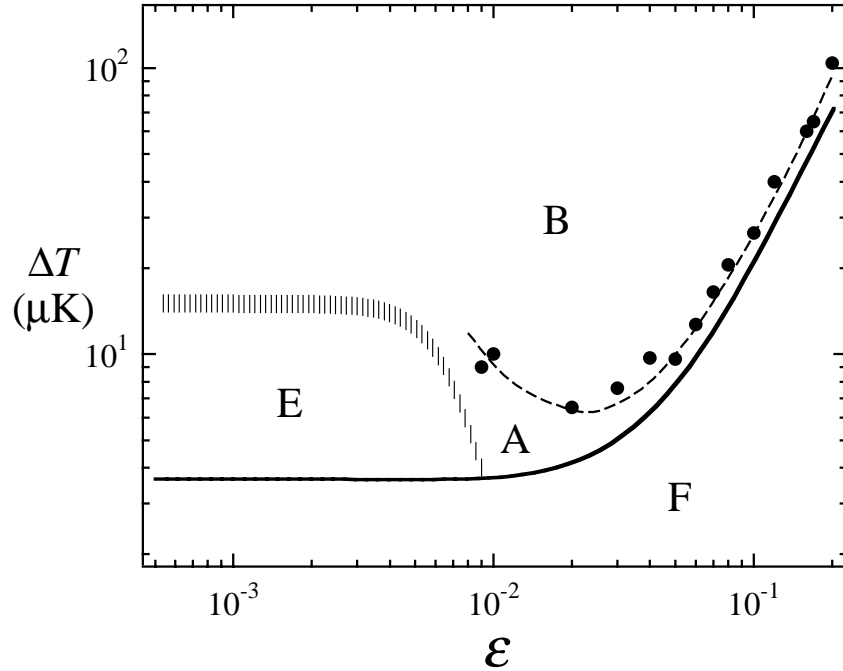


FIG. 2. Tentative “zone diagram” for the profiles  $\Delta T(t)$  in the  $\Delta T - \epsilon$  plane. The line of solid circles forms the boundary between zone A and B. There are no data for this boundary below  $\epsilon < 9 \times 10^{-3}$ , where no oscillations are observed. In zone E, no “overshoot” is observed. In zone F, the fluid is mechanically stable.

of these components are functions of  $\epsilon$  and of  $q$ . For a given  $\epsilon$ , both  $\tau_{tail}$  and  $t_{osc}$  decrease with increasing  $q$ , and always  $t_{osc} < \tau_{tail}$ . When  $t_{osc}$  becomes comparable to the time constant of the thermometer circuitry,  $\simeq 1.3$  s., the oscillation amplitude and finally the first peak become smoothed out and only the base profile relaxation is observed. This evolution with  $q$  at  $\epsilon = 0.05$  can be seen in Fig.3, where for emphasis only the top portion of the  $\Delta T(t)$  profile is shown.

For the determination of  $\tau_{tail}$ , which ranged from  $\sim 5$  to 100 s., the data curve was fitted to an exponential, and a check of the dependence on the sampling range showed an internal consistency in  $\tau_{tail}$  within about  $\pm 10$  %. The relaxation profile distortion by the instrumental time constant has been considered [9]. Besides an amplitude shift with time, there is no significant change produced in the value of  $\tau_{tail}$ . The oscillation period  $t_{osc}$  was obtained from the time count between succeeding minima, with an error within approximately  $\pm 10\%$ . In this determination, the position of the first maximum in  $\Delta T(t)$  after starting the heat flow was not included. This was because the time between this maximum and the first minimum,  $t_m$  as defined in ref. [4], is larger than half of the oscillation

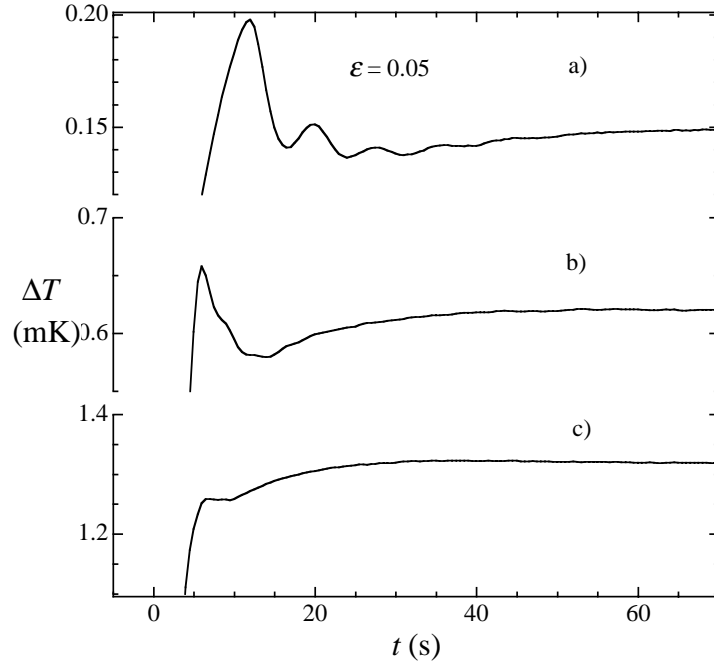


FIG. 3. Evolution of the profiles  $\Delta T(t)$  at  $\epsilon = 0.05$  with increasing values of  $q$  (in  $10^{-8}$  W/cm<sup>2</sup>) a) 96.5, b) 613, c) 1540.

period  $t_{osc}$ . This asymmetry is most evident for  $\epsilon = 0.2$ , and gradually decreases with  $\epsilon$ .

At high enough values of  $q$ , an additional very broad maximum is observed before  $\Delta T(\infty)$  is reached from above. The amplitude of this component is only at most 0.3 % of  $\Delta T(\infty)$  and the corresponding relaxation time to steady state is estimated to be about  $O(5\tau_{tail})$ . We will neglect here the small effect of this additional component.

We have found that plots of both  $t_{osc}$  and  $\tau_{tail}$ , when scaled by the diffusive time  $t_D = L^2/4D$  [8], and plotted versus  $[Ra^{corr} - Ra_c]$ , can be collapsed on two separate curves. Here  $D$  is the thermal diffusivity,  $Ra^{corr}$  is the Rayleigh number corrected for the adiabatic temperature gradient [2] and  $Ra_c=1708$  is the critical Rayleigh number. The range of scaling extends over about 3.5 decades in  $[Ra^{corr} - Ra_c]$ . In Fig.4 we show this scaling plot where the various symbols indicate the temperatures  $\epsilon$  where the transients were recorded. There are some systematic deviations and scatter of less than  $\pm 10\%$  from the average curves. This is a remarkable result because with decreasing  $\epsilon$  over the range for this plot, the compressibility and  $t_D$  increase by factors of 40 and 20 respectively, and the Prandtl number  $Pr$  increases

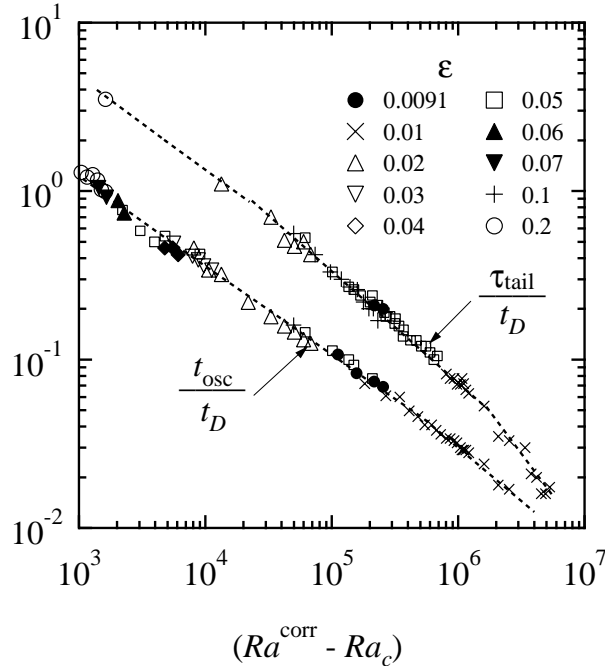


FIG. 4. Scaled plots of  $t_{osc}/t_D$  and  $\tau_{tail}/t_D$  versus  $[Ra^{corr} - Ra_c]$  for reduced temperatures  $9 \times 10^{-3} \leq \epsilon \leq 0.2$ . The two dashed lines are “guides to the eye”.

from 2 to 42. Over approximately 2.5 decades of  $[Ra^{corr} - Ra_c]$ , the curves for  $t_{osc}/t_D$  and  $\tau_{tail}/t_D$  can be represented by power laws with exponents of  $\simeq -0.52$  and  $-0.60$ . Hence both scaled times diverge as  $[Ra^{corr} - Ra_c] \rightarrow 0$ . There seems to be no clear dependence on  $Pr$ , as shown by the collapsing of the data for various values of  $\epsilon$ . The scaling in Fig.4 is the analog of the  $Nu^{corr}(Ra^{corr})$  plot for the steady state shown in Fig 7 of ref. [2], and which to a first approximation is independent of the properties of fluids. We can therefore expect that the representations in Fig.4 should be the same for other fluids kept at constant volume, and hence they represent in a crude first approximation a universal set of curves. We note that for convection transients observed at constant pressure in liquid  $^4\text{He}$  [10],  $\Delta T(t)$  relaxes from its “overshoot” maximum towards  $\Delta T(\infty)$  with a characteristic time that diverges as  $[Ra - Ra_c] \rightarrow 0$ , similarly showing the “slowing down” as the transition to fluid stability is approached. For  $\epsilon < 9 \times 10^{-3}$ , no damped oscillations were detected, and the character of the transients seems to have changed (See refs. [2]. An analysis of  $\tau_{tail}$  at  $\epsilon = 5 \times 10^{-4}$  showed the data to be inconsistent with an extrapolation from the curve in Fig.4 to the higher  $Ra$  numbers ( $\sim 4 \times 10^8$ ) corresponding to these data.

This work is supported by NASA grant NAG3-1838. We greatly appreciate the help of Fang Zhong with formatting the Figures.

- 
- [1] J.J. Niemela, L. Skrbek, K.R. Sreenivasan and R.J. Donnelly, *Nature* **404**, 837 (2000), X. Chavanne, F. Chilla, B. Chabaud, B. Castaing and B. Hebral, *Phys. Fluids* **13**, 1300 (2001), X.Xu, K.M.S. Bajaj and G. Ahlers, *Phys.Rev. Lett.* **84**, 4357 (2000).
  - [2] A.B. Kogan and H. Meyer, *Phys. Rev. E* **63** , 056310 (2001).
  - [3] H. Meyer and A.B. Kogan (to be published).
  - [4] Y. Chiwata and A. Onuki, *Phys. Rev. Lett.* **87**, 144301 (2001), A. Furukawa and A. Onuki, *Phys. Rev. E* **66** (2002) to appear.

- [5] A. Onuki and R.A. Ferrell, Physica A **64**, 245 (1990).
- [6] P. Carlès, Physica D **147**, 36 (2000) and private communication.
- [7] S. Amiroudine and B. Zappoli (private communication, and preprint).
- [8] This diffusion time is as defined in [4], and differs from the usual diffusive time  $L^2/D$  in ordinary fluids by a factor of 4. This is because  $t_D$  is chosen for the situation of a supercritical fluid where  $C_p \gg C_v$ , and for relaxation at constant density. Under such conditions, the relaxation time is 4 times shorter than when  $C_p \approx C_v$  ( See. R.P. Behringer, A. Onuki and H. Meyer, J. Low. Temp. Phys. **81**, 71 (1990)
- [9] We are indebted to D. Schaeffer of the Duke U. Mathematics Department for producing an equation expressing the observed  $\Delta T(t)$  signal in terms of an input signal modified by an instrumental time constant shorter than  $\tau_{tail}$ .
- [10] R.P. Behringer and G. Ahlers, Phys. Lett. A **62**, 329 (1977), R.P. Behringer, Rev. Mod. Phys. **57**, 657 (1985)

## **Turbidity in a density-matched system**

Don Jacobs  
The College of Wooster  
Wooster, OH 44691

The turbidity of a density-matched, liquid-liquid mixture has been measured very near its critical point. Understanding critical phenomena in simple systems, as in the liquid-liquid system studied here, is essential both to test theory and to serve as a model system for more complex behavior near a critical point. We are conducting a ground based (1-g) experiment that measures the turbidity of methanol-cyclohexane extremely close to its critical consolute point. By covering the range of reduced temperatures  $t=(T-T_c) / T_c$  from  $10^{-8}$  to  $10^{-2}$ , the turbidity measurements allow the Green-Fisher critical exponent  $\beta$  to be determined. The turbidity data can also be compared to the theoretical approximation developed by Ferrell and to a recent Monte Carlo simulation. These two results predict very different behavior for the turbidity when very close to the critical point and our experiment can help address the differences.

## **Correlation length of perfluoroheptane and 2,2,4-trimethylpentane**

Don Jacobs  
The College of Wooster  
Wooster, OH 44691

The turbidity of the liquid-liquid mixture perfluoroheptane and 2,2,4-trimethylpentane (also known as iso-octane) has been measured and used to determine the correlation length amplitude. By measuring the ratio of the transmitted to incident light intensities over three decades in reduced temperature, we are able to determine that that amplitude to be  $0.242 \pm 0.009$  nm. This value differs significantly from that reported in the literature. When we combine this value with the amplitude  $A^+$  determined in a recent heat capacity measurement on this system, the two-scale-factor universality constant  $X$  is  $0.0177 \pm 0.0018$ , which is quite consistent with other determinations between 0.018 and 0.020.



# Observations on Solid $^4\text{He}$ Growth using Interdigital Height Detector

J. Fay and H. Kojima

*Serin Physics Laboratory, Rutgers University, Piscataway NJ 08854*

## Abstract

A compact interdigital capacitor is used as a level detector to study the solid  $^4\text{He}$  edge height. The capacitor consists of 38 interlaced  $50\text{ }\mu\text{m}$  wide and  $3.8\text{ mm}$  long gold films separated by  $50\text{ }\mu\text{m}$  and deposited onto a flat  $5\times 5\text{ mm}^2$  sapphire substrate. The background capacitance is  $6.5\text{ pF}$ . The capacitance change is  $1.3\times 10^{-3}\text{ pF/mm}$  of solid  $^4\text{He}$  height change. A height change of  $11\text{ }\mu\text{m}$  is detectable. Observations at  $1.15\text{ K}$  show over pressures (measured with a low temperature strain gauge) up to  $25\text{ mbar}$  prior to nucleation of solid. The solid height may be controlled by varying heat applied to a pressure bomb cooled to  $77\text{ K}$ . Small stresses are applied to the solid to look for changes in solid height that should occur to maintain the equilibrium with the superfluid in contact.

PACS numbers: 67.80.-s, 62.20.-x

Keywords: quantum crystal, Grinfeld instability, interdigital capacitor

## I. MOTIVATION

The ultimate goal of our research is to study the instability of solid surface morphology under applied stresses[1]. We choose solid  $^4\text{He}$  in contact with superfluid as a model material. For investigation of interface related phenomena, the solid/liquid interface of  $^4\text{He}$  below 2 K has many advantages such as small latent heat, rapid melting and freezing and superfluid heat conduction. A simple compact solid helium height detector is useful for diagnostic and monitoring purposes. Capacitor sensors with simple parallel plate configuration are commonly used to detect changes in the amount of material inserted between the plates. For our study, confining helium into small volume is not desirable in reducing the boundary effects. For this reason, we choose to work with an interdigital capacitor(IDC) which occupies a minimal volume and can be mounted onto the wall of a sample chamber.

## II. APPARATUS

The rectangularly shaped solid helium sample chamber is depicted in Fig. 1. An IDC is mounted on one vertical wall and a piezoelectric lead zirconate titanate transducer(PZT) with plunger plate is mounted on the opposite wall. Without the PZT being mounted, the chamber dimensions are  $10 \times 9 \text{ mm}^2$  at the base and 15 mm along the vertical. When the PZT is mounted, the base dimensions become  $10 \times 5 \text{ mm}^2$ . Helium is fed in via fill tube. The pressure in the chamber is monitored by an *in situ* Straty-Adams type capacitive strain gauge(not shown). By applying dc voltages across the PZT, stresses can be applied on the solid.

The IDC consists of 38 interlaced  $50 \text{ }\mu\text{m}$  wide and 3.8 mm long gold finger films separated by  $50 \text{ }\mu\text{m}$  and deposited onto a flat  $5 \times 5 \text{ mm}^2$  sapphire substrate. The total capacitance  $C$  is given by  $C = (c_1 + c_2 + c_3)NL$  where  $N$  is the total number of pairs,  $L$  the length of the fingers,  $c_1 = \frac{\epsilon_o \epsilon_1 K[(1-(a/b)^2)^{1/2}]}{2K[a/b]}$  where  $K[x]$  is a complete elliptic integral of the first kind[3]. Here,  $\epsilon_1$  is the dielectric constant of helium deposited on the IDC. The capacitance between fingers is given by  $c_2 = \epsilon_o \epsilon_2 \frac{h}{a}$ , where  $h$  is the thickness of the film and  $a$  is the distance between the edges of the adjacent fingers and  $b$  is the distance between the centers of the adjacent fingers. Since the thickness of the fingers is at most  $5 \times 10^3 \text{ \AA}$ ,  $c_2$  does not contribute significantly to the total capacitance. The term  $c_3$  is similar to  $c_1$  except

### Interdigital Capacitor and Solid Growth Chamber

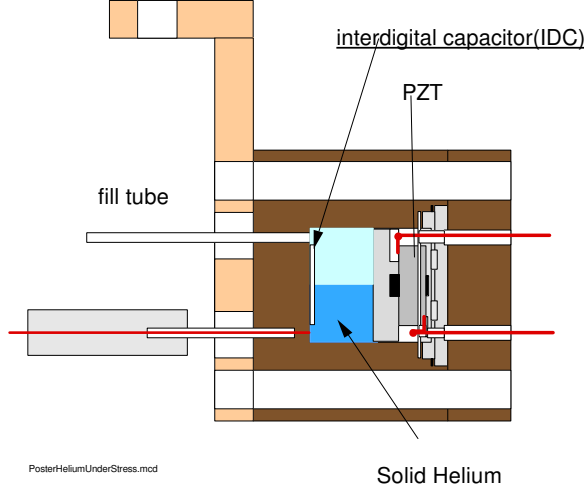


FIG. 1: Schematic of solid helium sample chamber with PZT as stress generator

$\epsilon_1$  becomes the dielectric constant of the sapphire substrate. The capacitance is measured with a bridge (General Radio, model 1900) whose off-balance signal is monitored by a lock-in amplifier operating at 2 kHz. If the effective dielectric constant of sapphire is taken as 10 ( $\epsilon_{\parallel c} = 9.4$  and  $\epsilon_{\perp c} = 11.5$ ),  $c_3 = 8.1$  pF. This is not too far from the measured 6.5 pF.

## III. RESULTS

### A. Condensing Liquid

After the chamber is cooled down to and maintained at 1.2 K, it is slowly filled with helium from a room temperature source. The change in the lock-in output voltage during this process is shown in Fig. 2. The output voltage to capacitance conversion ratio is 1.849V/0.01pF. Prior to the time interval shown in Fig. 2, there is a sudden decrease (reproducible from run to run) of about 0.005 pF. We suspect the decrease comes from the change in temperature of the sapphire substrate.

The expected change in capacitance between point (a) and point (b) when the IDC is fully covered with liquid helium at 1.2 K is  $\Delta C = \frac{\epsilon_o \delta \epsilon_1 2.441 NL}{2 \times 1.854} = 0.0458$  pF ( $\delta \epsilon_1 = 1.057 - 1 = 0.057$ ). The measured value is 0.040 pF in fair agreement.

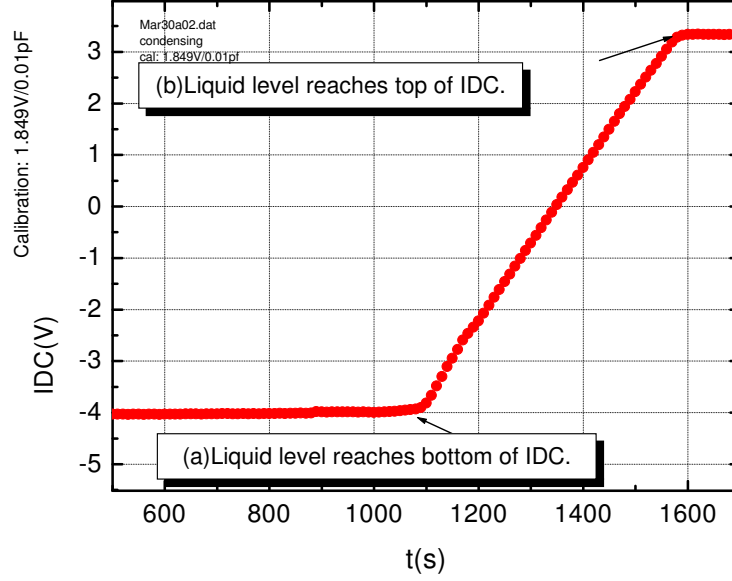


FIG. 2: Change in capacitance during condensing liquid into the sample chamber.

### B. Pressurizing Liquid

Once the chamber is totally filled with liquid helium, the chamber is pressurized slowly up to the melting pressure. The lock-in output ( $0.935\text{V}/1\text{fF}$ ) increases as shown in Fig. 3. The same measurement is shown in Fig. 4 as a function of the liquid density[4]. The capacitance increases linearly with the density as expected. The expected change from the increase in density of helium in the pressurization from the vapor pressure to the melting pressure is  $+7.4\text{ fF}$ . However, the observed change is only  $+4.5\text{ fF}$  in disagreement with the expectation. A small movement in the connecting leads not close to the IDC is suspected to be the source of disagreement.

### C. Growing Solid

When the chamber pressure approaches the melting pressure within 5–10 psi, the rate of filling is controlled by applying heat to a small separate helium "bomb" cooled to near 77 K and open to the chamber. An example of observed temporal evolution in growth and melting of solid is illustrated in Fig. 5. The lock-in output is converted to changes in capacitance. The chamber pressure must often exceed the equilibrium melting pressure before a solid seed nucleation (see below for further discussion) occurs as signaled by the spike in  $\Delta C$  at  $t = 900\text{ s}$ . Once a nucleation occurs, the chamber pressure remains constant as more helium is fed

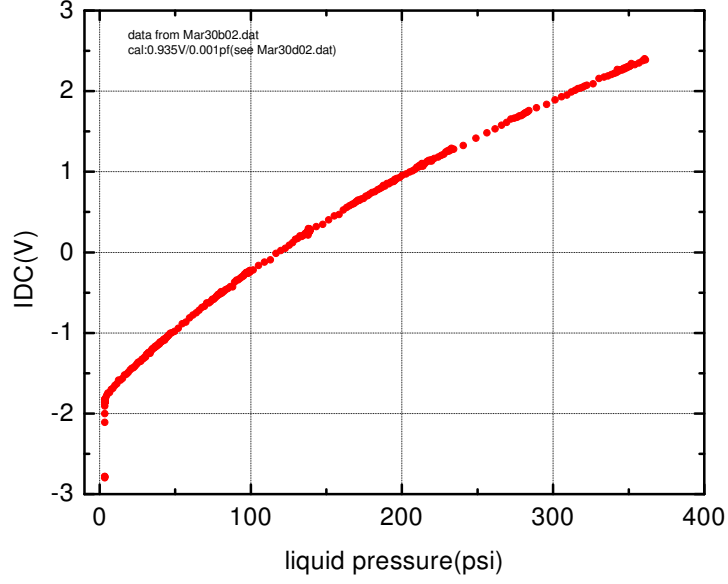


FIG. 3: Change in capacitance during increase in pressure from saturated vapor pressure to melting pressure.

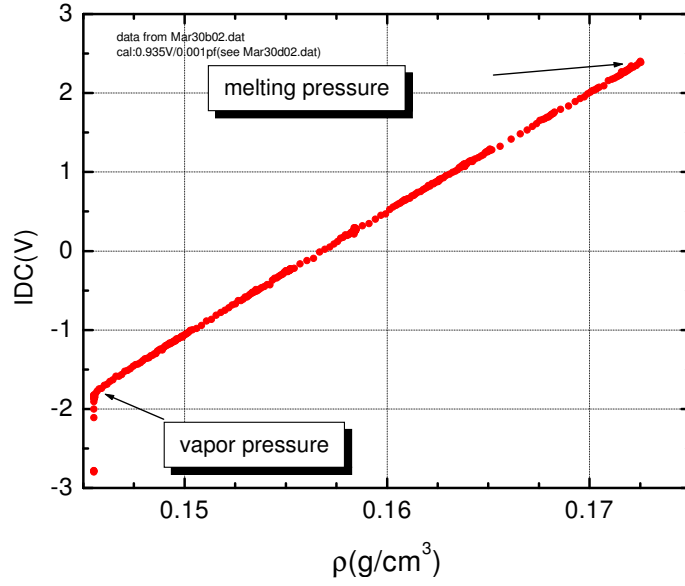


FIG. 4: Change in capacitance during the pressurization shown in Fig. 3 plotted as function of density.

into the chamber at the melting pressure determined by the temperature. There is a blind interval of time when the solid level cannot be detected since the IDC does not extend to the bottom of the chamber. In Fig. 5, the solid level reaches the lower end of IDC at about 1100 s.[5] A relatively smooth increase in height of the solid is observed till the capacitance saturates when the solid level reaches the top of the IDC. When helium is continued to be fed

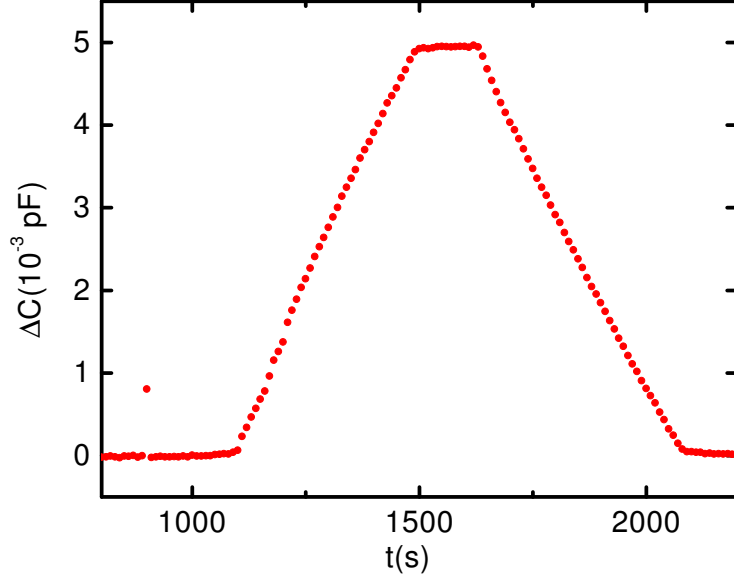


FIG. 5: Nucleation, growth and melting of solid  $^4\text{He}$ .

into the chamber, the inlet pressure to the chamber suddenly increases when the chamber is totally filled with solid. The chamber pressure sensor shows no change here since it becomes disconnected from the chamber by a solid plug. The melting is induced by removing helium from the chamber. The rate of melting can again be controlled by varying the heater power applied to the bomb.

The change in capacitance at liquid condensation, pressurization and solid growth are all shown in Fig. 6 as a function of the change in helium density at each "transformation." A straight line is drawn through the origin and the condensation data point. The discrepancy as noted above in the capacitance change during the pressurization shows up clearly. The observed total change in capacitance during the solid growth is 5.0 fF. The expected change normalized by the change in density to the measured  $\Delta C$  at vapor-liquid transition is 4.9 fF in good agreement.

#### D. Super-pressurization at Nucleation Events

Nucleation events can be seen in some but not in all runs. Three consecutive nucleation events in one run are seen by both the IDC and by the chamber pressure sensor capacitance as shown in Fig. 7. The super-pressurization in the chamber before the nucleation begins varies from one nucleation to the next. To repeat seeing nucleation, the pressure is dropped below the melting pressure by about 60 mbar. No under-pressurization drop is observed

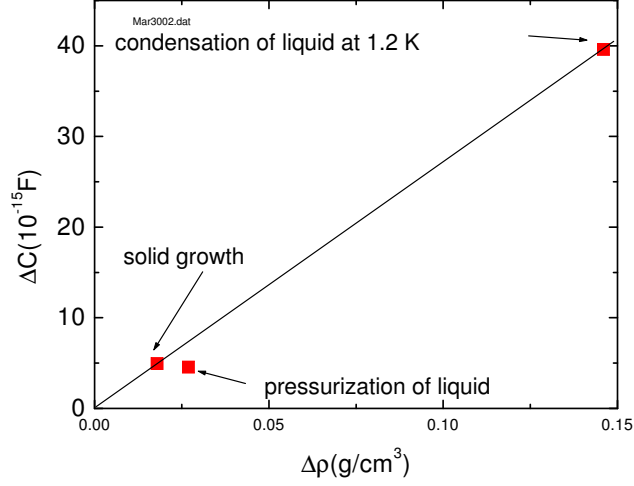


FIG. 6: Changes in capacitance measured at three "transformations" as function of density change.

when the solid begins to melt. Note that the melting pressure (and therefore the chamber temperature) is increasing as time passes. In this run, the nucleation process could be seen repeatedly. However, the super-pressurization required for nucleation varies from cool down to cool down and it can barely be detected by our chamber pressure sensor in some runs. In such cases, lowering the pressure even by 15 psi before increasing the pressure to the melting pressure again did not induce super-pressurization.

One nucleation event is displayed in detail in Fig. 8 The super-pressurization here is

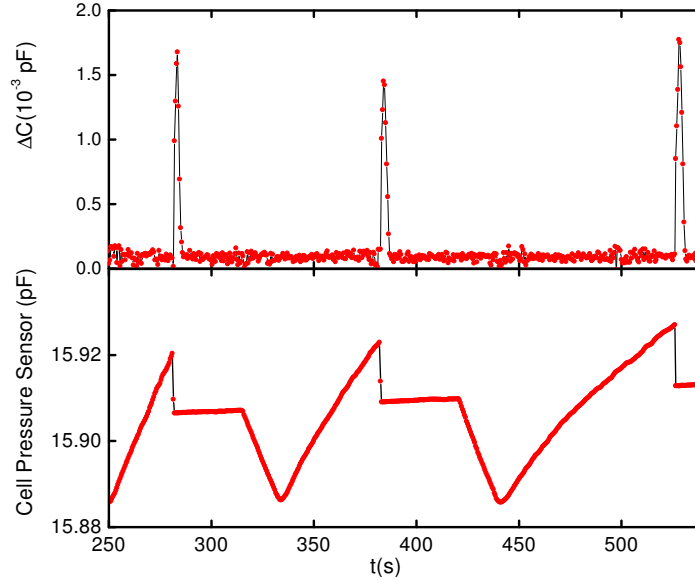


FIG. 7: Three nucleation events: upper panel, the capacitance change of IDC; lower panel, capacitance change of *in situ* pressure sensor.

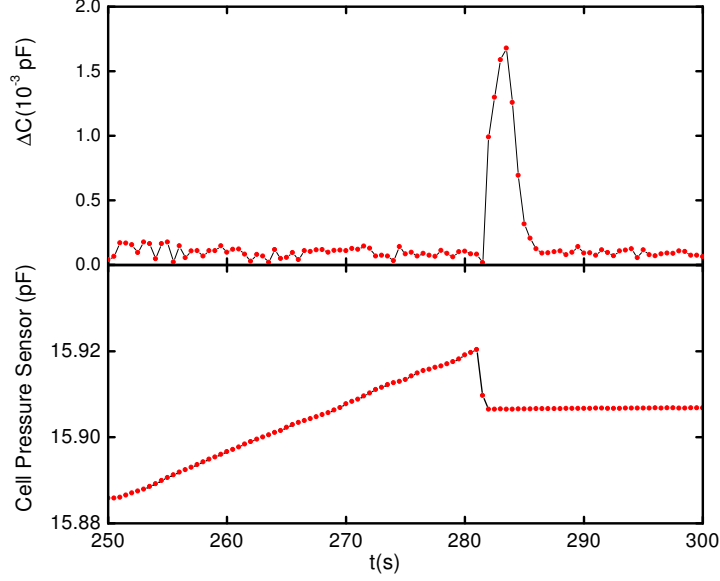


FIG. 8: Detail of one nucleation event.

25 mbar. Data are taken every 0.5 s and the IDC lock-in time constant is set at 0.1 s. The chamber pressure drop after the nucleation occurs within 0.5 s. Presumably, the time interval is limited only by the solid growth coefficient. The response time of the chamber pressure sensor is not fast enough to follow the rapid changes in the chamber pressure as observed by Tsymbalenko[6]. Estimating the change in density as  $\delta\rho = \delta p/c^2$  where  $\delta p$  is the super-pressure and  $c = 365$  m/s is the speed of sound at the melting pressure, we find the volume of the solid seed created is about  $5 \times 10^{-5} \text{ cm}^3$ . If the seed has a spherical shape, its radius is 0.2 mm. Subsequent to the nucleation event, the IDC detects the presence of solid seed. The relatively long time interval during which the presence of solid is detected by the IDC indicates that the response is not caused by some acoustic disturbance that would be launched at the time of nucleation. It seems that the seed appears near the top of the IDC, slides along its surface and finally settles down to the bottom of the chamber.

### E. Applying Stress to Solid $^4\text{He}$

Consider a slab of solid  $^4\text{He}$  (of density  $\rho_C$ ) in contact with liquid (of density  $\rho_L$ ) on top. Apply a horizontal stress  $s_0$ :  $\sigma_{xx} = \sigma_{zz} + s_0$  with  $u_{yy} = 0$ . The solid acquires extra elastic energy. The chemical potential of the solid and liquid at the interface must maintain equality. Therefore, the solid must melt for the liquid to increase its chemical potential. The solid/liquid interface height is *lowered*. The decrease in height in terrestrial gravity is



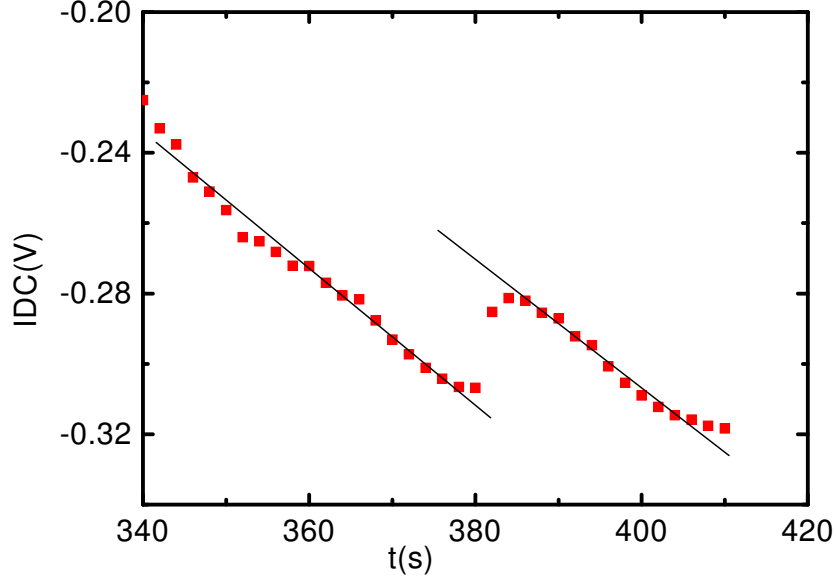


FIG. 9: Change in capacitance of IDC when stress is applied on solid  $^4\text{He}$  with PZT.

given by[7]

$$\delta H = \frac{(1 - \nu)s_0^2}{2Yg(\rho_C - \rho_L)} \quad (1)$$

where  $g$  is the gravitational acceleration,  $\nu$  Poisson's ratio, and  $Y$  Young's modulus.

Stress was applied on the solid  $^4\text{He}$  to look for this expected change in height using our IDC. The change in length of the PZT is given by  $\delta x = d_{pzt}V$ , where  $d_{pzt}$  is the effective piezoelectric constant and  $V$  the applied voltage across the PZT. The stress applied on the solid is  $s_0 = (\delta x/X)Y$ , where  $X$  is the length of the solid. From our own measurement of the piezoelectric constant at 300 K and 77 K, we estimate it to decrease to about  $30 \times 10^{-12}$  m/V at 1.2 K. Putting in the material parameters[8], the expected decrease in height is 7  $\mu\text{m}$  at  $V = 1200$  V (the maximum voltage available from our dc supply) is applied on the PZT.

Four runs during which many attempts to look for solid height changes with various values of applied voltage  $V$  have been conducted. The search was made between 1.15 and 1.25 K. Both polarities of the applied voltage were tried. If the solid  $^4\text{He}$  sticks to the plunger, the change in height does not depend on the sign of the applied strain. The height of the solid was varied between the middle to near the top of the IDC. In many of the attempts made, the applied voltage to the PZT produced no measurable effect. In two of the runs, height changes were observed coincident with the applied voltage and with the correct direction of change. An example is shown in Fig. 9. Note there was a steady decrease in height owing

to a small temperature drift. When 1200 V was applied at  $t = 310$  s (not shown owing to concurrent height change owing to a temperature change), the height decreased. When the voltage was turned off at  $t = 380$  s, the height increased back up. The corresponding change in height is  $37 \mu\text{m}$ . This is much greater than the expected value. Attempts to produce intermediate change in height were not successful.

Considering the minimum detectable limit is greater than about  $11 \mu\text{m}$ , it would be difficult to see the expected drop in height at 1200 V. It is surprising that large effects such as shown in Fig. 9 were seen. Let's see if the critical threshold stress for onset of stress-induced instability was exceeded. The critical threshold stress is given by

$$s_c = \left\{ \frac{((\rho_C - \rho_L)\gamma g)^{1/2} Y}{1 - \nu^2} \right\}^{1/2} \quad (2)$$

where  $\gamma$  is the surface tension ( $\sim 0.2$  dyne/cm). Putting in numbers, the corresponding critical strain is  $u_{xxc} = s_c/Y \sim 10^{-4}$ . The extension of the PZT at 1200 V is about  $4 \times 10^{-6}$  cm and so the strain on the solid  $^4\text{He}$  would be  $\sim 10^{-5}$ . This is smaller than  $u_{xxc}$  by a factor of 10. Thus, a stress-induced instability can be eliminated as the cause of the effect shown in Fig. 9. Rapid changes in temperature is known to initiate surface instabilities[9]. As seen by the *in situ* pressure sensor, there does not appear to be large enough temperature changes to cause such thermal effects. Thus, the effects seen in Fig. 9 remains a mystery.

## Acknowledgements

We thank Misha Grinfeld for inspiration and discussions. J. F. is a Rutgers Undergraduate Research Fellow. The research is supported by NASA.

- 
- [1] M.A. Grinfeld, Soviet Phys. Doklady, **31**, 31(1986); Europhys. Lett. **22**, 723(1993).
  - [2] G.K. White, *Experimental Techniques in Low Temperature Physics*, Clarendon Press, Oxford(1989).
  - [3] H.E. Endres, S. Drost, Sensor Actuators **B4**, 95(1991).
  - [4] The liquid pressure at  $T = 1.2$  K was converted to density(given in  $\text{g/cm}^3$ ) using an empirical formula:  $\rho = 0.14511 + 1.20755 \times 10^{-4} p - 2.34104 \times 10^{-7} p^2 + 4.62392 \times 10^{-10} p^3 - 4.36575 \times 10^{-13} p^4$ , where  $p$  is the pressure in psi.

- [5] In the initial attempts of this experiment, irreproducible transient change in capacitance between the nucleation event and the when the solid level reaches the lower edge of IDC. This effect turned out to be caused by the motion of the 50  $\mu\text{m}$  diameter gold hook up wires to the IDC when  $^4\text{He}$  solid deflected them. When the wires were made rigid by applying small amount of Apiezon N grease, the effect disappeared.
- [6] V.L. Tsymbalenko, Phys. Lett. **A274**, 223(2000).
- [7] S. Balibar and P. Nozières, Solid State Comm. **92** 19(1994).
- [8] The material parameters at  $T = 1.2\text{ K}$  are used:  $\rho_C = 0.1908\text{ g/cm}^3$ ,  $\rho_L = 0.1729\text{ g/cm}^3$ ,  $\nu = 1/3$ , and  $Y = 3 \times 10^8\text{ dyne/cm}^2$ .
- [9] J. Bodensohn, et al., Z. Phys. B Cond. Matt. **64** 55(1986).

# Effects of Heat Current on The Superfluid Transition In a Low-gravity Simulator

*Charles C. Hays, Yuanming Liu, Melora Larson,  
Warren Holmes, and Ulf E. Israelsson*

Jet Propulsion Laboratory  
California Institute of Technology  
Pasadena, Ca

## Abstract

Liquid  $^4\text{He}$  provides an ideal system for the study of phase transitions under non-equilibrium, dynamic experimental conditions. Under the influence of a heat current,  $Q$ , the physical properties become nonlinear and  $Q$ -dependent near the superfluid transition. For example, renormalization-group<sup>1</sup> and mean-field<sup>2</sup> theories predict an enhancement of the heat capacity due to an applied heat current, and these predictions have been experimentally verified.<sup>3</sup> Gravity induced pressure variations in the liquid may influence the character of the transition in addition to our ability to examine the transition experimentally.

As such, to examine the effects of gravity on the heat-current influenced superfluid transition in *liquid*- $^4\text{He}$ , a low-gravity simulator facility has been developed at JPL.<sup>4</sup> One of the more attractive aspects of this experiment is that these data fill the void in results between 1g earth-based studies and proposed  $\mu\text{g}$ -experiments. The low-g simulator uses a superconducting magnet to supply the magnetic force profile  $\nabla B(\text{dB/dz}) \sim -22 \text{ T}^2/\text{cm} = \mu\text{g}$  to cancel gravitationally-induced hydrostatic pressure variations in a helium sample over a range 0.01 to 1g. In this reduced gravity range, experiments have verified that the canceling B-field does not change the sample pressure. In this poster we describe the experimental work in progress to improve our experimental capabilities. These improvements include the implementation of SQUID-based mini-high-resolution-thermometers (mini-HRTs) onto a new cryostat probe. High permeability magnetic shields will be used to reduce the stray magnetic fields that adversely affect the performance of the SQUID sensors and mini-HRTs. Continuous cooling of the existing superconducting magnet to  $T = 2.2 \text{ K}$  using a  $\pi$ -plate refrigerator will also be incorporated into the design of the new facility.

## References

1. R. Haussmann and V. Dohm, Phys. Rev. Lett. **72**, 3060 (1994).
2. T.C.P Chui, D.L. Goodstein, A.W. Harter, and R. Mukhopadhyay, Phys. Rev. Lett. **77**, 1793 (1996).
3. A.W. Harter, R.A.M. Lee, A. Chatto, X. Wu, T.C.P. Chui, and D.L. Goodstein, Phys. Rev. Lett. **84**, 2195 (2000).
4. Y. M. Liu, M. E. Larson, and U. E. Israelsson, J. Low Temp. Phys. **113**, 867 (1998).

## **Dynamics near the critical point in heat flow**

Akira Onuki

Dept. of Physics, Kyoto Univ., Japan

First, we consider dynamics near the critical point in heat flow.

After a review of convection above  $T_c$  near the gas-liquid critical point, we discuss a new problem of two-phase convection, where bubble boiling and liquid condensation take place from the bottom and top boundaries. Here even for a very small temperature increase, a gas film appears at a heated surface due to enhanced thermal expansion near criticality. At larger heat input, the temperature gradient automatically assumes a unique small value (0.034 mK/cm for  $^3\text{He}$ ) in the interior of the cell, while it becomes mostly localized in the layers near the boundaries. Thus heat flow from below and phase separation are coupled to form unique self-organized convective states in the interior. Interestingly, this is analogous to formation of self-organized superfluid states in  $^4\text{He}$  with high-density vortices under gravity and heat flow from above. These hydrodynamic effects are very sensitive to gravity.

Second, we show that the wetting properties are very sensitive to heat flow.

# Compressibility Measurements near the Critical Point of Oxygen

J. A. Lipa, D. A. Stricker, D. Avaloff and S. Wang,

*Physics Department, Stanford University, Stanford, CA 94305.*

## ABSTRACT:

We describe preliminary results for the behavior of the compressibility of oxygen near its critical point obtained with an apparatus that reduces gravitational compression effects on the fluid. The results extend deeper into the asymptotic region near the critical point than was achieved in earlier experiments. The system uses magnetic levitation to reduce the hydrostatic compression of every element within a fluid and is capable of applying forces of  $\pm 3$  g to a sample of oxygen. By performing critical point experiments with gravity cancelled on earth, the need for scarce flight resources to study this field of physics can be reduced, leading to substantial savings for the taxpayer. Also, the time available for experiments can be much longer than anticipated in upcoming flight missions, especially those using low temperatures. The apparatus can be used for high resolution measurements of the equation of state, the coexistence curve, the specific heat, and transport phenomena.

## INTRODUCTION:

The goal of the work described here is to perform an improved investigation of critical phenomena entering deep into the asymptotic region by making use of magnetic levitation to reduce the hydrostatic compression of a fluid. This region cannot be accessed on the ground except in very special situations, for example, at the lambda point of helium. So far, no ordinary critical point has been investigated in this way. A number of flight experiments have been performed on near-critical systems and various difficulties have been encountered. We have developed a system to levitate a pure fluid, liquid oxygen, near its critical point at about 154 K, using magnetic forces. With careful tuning of the applied fields we expect to be able to reduce the hydrostatic compression near the critical point by a factor of at least  $10^3$  and possibly  $10^4$ , and perform measurements to within a part in  $10^7$  of the critical temperature. The first experiment we have performed is a measurement of the compressibility along the critical isochore. The results will be used to derive a new exponent value for the divergence of the compressibility along the critical isochore after corrections have been applied to the raw data described here.

A magnetic technique to cancel the hydrostatic pressure variations in a small column of liquid helium to the 1% level was demonstrated at JPL [1]. A similar magnet was also used at Brown University [2] to levitate large drops of helium. These experiments needed very large field  $\times$  field gradient ( $B \nabla B$ ) values to achieve levitation due to the small value of the susceptibility of helium. The resulting magnet design constraints severely limit the sample volume where accurate cancellation of gravity can be achieved. In contrast, a much more effective cancellation of the hydrostatic pressure over larger volumes can be accomplished with a sample of liquid oxygen in very modest magnetic fields using wide bore solenoids and carefully designed gradient coils.

Wilson's application of the RG calculation scheme to the problem of the critical point led to predictions for the exponents and many 'universal' amplitude ratios in the model [3]. However, in addition to the values for these quantities, there now exists a highly accurate field-theoretical prediction for the bulk scaling equation of state for the asymptotic critical region,

published very recently by Guida and Zinn-Justin [4]. Even more interesting for a direct experimental test is the bulk compressibility as it exhibits the strongest divergence among all thermodynamic quantities. In their present form these analytic field-theoretical results are configured for the 3-D Ising model, but they can be converted to predictions for gas-liquid systems using well-known transformations. These predictions for fundamental thermodynamic quantities are currently the most accurate ones in the entire field of bulk critical phenomena in statistical physics. They call for equally accurate experimental tests which extend significantly beyond pure exponent measurements, involving the entire PVT surface and the behavior of parameters over wide ranges of the intensive variables  $P$  and  $T$ . The project described here is designed to address these issues.

## APPARATUS

The instrument we have built consists of a magnetic levitation system that is capable of canceling the effect of gravity on liquid oxygen to about 0.1%, a capacitance cell with associated electronics for equation of state and order parameter measurements, and a thermal enclosure designed to achieve a thermal stability and homogeneity of about  $10^{-8}$  in the reduced temperature  $t = T/T_c - 1$  near 154 K. The levitation system consists of a solenoid and a gradient coil configured to provide a lift force uniformity of about 0.1% over a disk-shaped volume 1 mm high and 1 cm in diameter. The uniform field and the gradient can be adjusted independently. To minimize the effects of magnetic contaminants on the field distribution, all components within the magnet bore are fabricated from non-magnetic materials. The cell contains a pair of narrow gap capacitors formed from aluminum deposited on sapphire. These capacitors were designed to be very stable and have low sensitivity to pressure. The capacitors are separated vertically by about 0.7 mm and are 0.5 cm in diameter. By applying a pulsed dc bias to the plates the effect of electrostriction on the fluid can be observed.

A significant element of the apparatus is the thermal control system. We designed a system to achieve a stability and homogeneity of about  $10^{-8}$  near the critical point, allowing good operation at the resolution goal of  $t \sim 10^{-7}$ . This is at about the level obtained in state-of-the-art thermal controllers such as those used on the Zeno flight experiment and planned for the MISTE experiment. The mechanical portion of the control system is a multi-shell enclosure operated in a high vacuum. A photograph of the partially disassembled system with the shells removed is shown in figure 1. Temperatures are measured using thermistors and conventional high resolution ac bridge techniques involving high stability ratio transformers. Calibration is performed with a platinum resistance thermometer. Of special importance is the cell fill line that must pass through the helium bath. If it was not insulated from the helium, the oxygen would freeze in it, limiting our ability to change the sample density. Insulation is provided by enclosing the capillary in a vacuum tube and equipping it with heaters and thermometers distributed along the line. For many measurements it is acceptable to have the line closed at least part of the time.

## RESULTS

The sample density is measured by monitoring the shift in capacitance between two plates due to the fluid filling the gap. A commercial capacitance bridge with a resolution  $\Delta C/C \sim 10^{-7}$  is used for the measurements. The density measurements were calibrated by reference to the coexistence curve after allowance for the empty cell capacitance. Of most interest are density differences from some reference value, commonly the critical density. So far, the



**Figure 1:** Inner components of thermal control system.

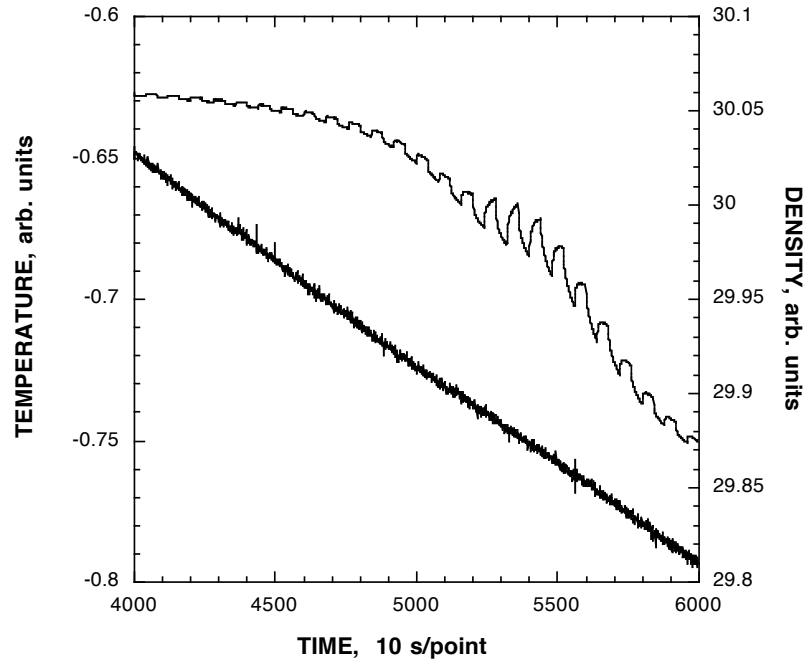
density and compressibility data has been calibrated by reference to the results of Weber [5]. Longer term we plan to use our own isotherm measurements for the reference. In figure 2 we show some typical electrostriction data obtained as the cell cools along an isochore close to critical.

Figure 3 shows some initial measurements of the compressibility in the critical region using the lower pair of capacitor plates. From separate coexistence curve measurements it appears that for this set of data the mean density of the sample is within 1% of critical, and possibly much closer. The data shows some rounding for  $t < 5 \times 10^{-6}$ . This effect is still being investigated. Additional compressibility measurements are being performed on nearby isochores.

## ACKNOWLEDGMENTS

We wish to thank the NASA office of Life and Microgravity Sciences and Applications for its support with grant # NAG8-1431.





**Figure 2:** Typical set of compressibility and temperature measurements in the critical region.

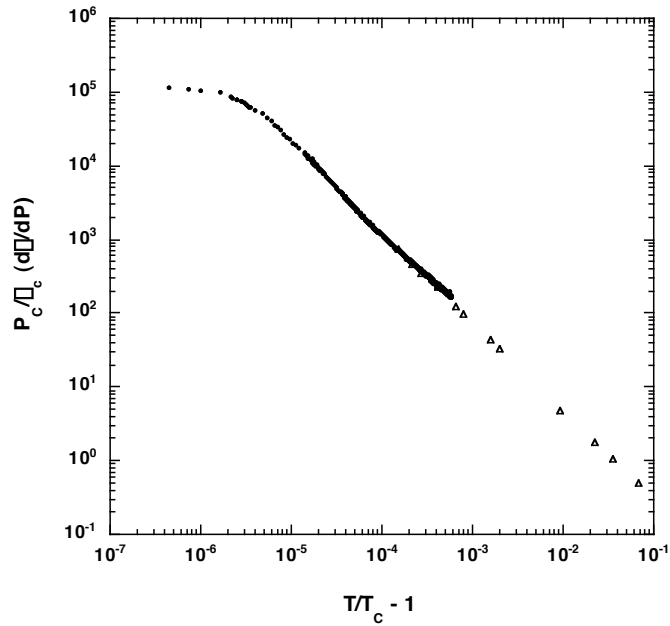


**Figure 3 :** Compressibility measurements in the critical region. Triangles are the results of Weber.

## REFERENCES

- 1: M. Larson, F-C. Liu, and U.E. Israelsson, Czech. J. of Phys. **46** part S1, 179 (1996).
- 2: M. A. Weilert, D. L. Whitaker, H. J. Maris and G. M. Seidel, J Low Temp. Phys. **106**, 101 (1997); M. A. Weilert, D. L. Whitaker, H. J. Maris and G. M. Seidel, Phys. Rev. Lett. **77**, 4840 (1996).
- 3: V. Privman, P. C. Hohenberg and A. Aharony, in: Phase Transitions and Critical Phenomena, eds: C. Domb and J. Lebowitz (Academic, N.Y., 1991), **14**, p.1.
- 4: R. Guida and J. Zinn-Justin, Nucl. Phys. B, preprint (1997).
- 5: L. A. Weber, J. Res. NBS, **74A**, 93 (1970).

## Experiments Along Coexistence near Tricriticality in $^3\text{He}$ - $^4\text{He}$ Mixtures

Melora Larson(a), Vladimir Dotsenko(b), Ashutosh Tiwari(b), Masoud Mohazzab(b),  
Norbert Mulders(b), Alfred Nash(a), John Panek(c), and Ben Vollmayr-Lee(d)

(a) Jet Propulsion Laboratory, California Institute of Technology, Pasadena, CA 91109

(b) Department of Physics and Astronomy, University of Delaware, Newark, DE 19716

(c) Goddard Space Flight Center, Greenbelt, MD 20771

(d) Department of Physics, Bucknell University, Lewisburg, PA 17837

The tricritical point in the phase diagram of  $^3\text{He}$ - $^4\text{He}$  mixtures offers unique opportunities to test our understanding of critical phenomena. Because  $D = 3$  is the marginal spatial dimension for tricriticality, the associated critical exponents are exact integer fractions. In addition, one expects to find logarithmic corrections. We present our results for the superfluid density, obtained from time-of-flight non-linear second sound measurements near the tricritical point and along the phase separation curve. We also report on our measurements of the phase separation curve near the tricritical point performed using inter-digital capacitor sensors on the top and bottom of our cell.

## **THE CAPABILITIES OF THE LOW TEMPERATURE MICROGRAVITY PHYSICS FACILITY FOR PERFORMING SCIENCE**

Melora Larson, Arvid Croonquist, G. John Dick, and Yuanming Liu  
Jet Propulsion Laboratory,  
California Institute of Technology,  
Pasadena, California 91109

The Jet Propulsion Laboratory (JPL) is developing the Low Temperature Microgravity Physics Facility (LTMPF). The LTMPF is a multiple-user and multiple-flight facility that will provide a long-duration low temperature environment for performing state-of-the-art experiments at the International Space Station (ISS). The LTMPF will fly attached to the Japanese Experiment Module (KIBO) Exposed Facility of the ISS, and the LTMPF will be ready for an initial flight in late 2005. The LTMPF is a self-contained, reusable, cryogenic facility containing a 180-liter superfluid helium tank, two experiment packages, and electronics to provide both control and telemetry. During each mission, two distinct primary experiments will be accommodated. Secondary experiments utilizing the hardware built for the primary experiments will also be accommodated during each mission. The detailed technical capabilities related to the science enabled by the Facility will be presented to illustrate how the LTMPF will provide a platform for breakthrough scientific investigations requiring both low temperatures and microgravity conditions.



# Numerical Simulation of Static and Dynamic Critical Properties of Confined Helium

Efstratios Manousakis  
Department of Physics and  
Center for Materials Research and Technology,  
Florida State University, Tallahassee, FL 32306-4350

July 15, 2002

## Abstract

We carry out state of the art simulations of properties of confined liquid helium near the superfluid transition, to a degree of accuracy which allows to make predictions for the outcome of fundamental physics experiments in microgravity. In this paper we discuss the specific heat and thermal conductivity of helium confined in pore-like and parallel plate geometries.

## 1 Introduction

The theory of second order phase transitions is based on the assumption that at temperatures close to the critical temperature there is only one dominating length scale associated with the critical behavior of the system. This length scale is the correlation length associated with the decay of the correlation function of the order parameter. Since the correlation length diverges as the critical temperature is approached, the microscopic details of the system are irrelevant for its critical behavior. This intuitive picture has its foundation in the renormalization group treatment of second order phase transitions. Within the renormalization group treatment, it becomes evident that the critical behavior can be divided into different universality classes. Each universality class is specified by only a few key features, such as the mathematical character of the order parameter and the dimensionality of the system. Vastly different systems, for example, a superfluid and a magnetic system can belong to the same universality class when the order parameter in both systems is a two-component vector. This implies that the set of critical exponents which describe the singular behavior of physical quantities in terms of the reduced temperature are the same. Because of this universal behavior of phase transitions, one can select an ideal and easier to work with system to study the critical behavior of all systems from each class at once.

During the past decade NASA has taken a number of key steps to support very important fundamental physics whose experimental implementation was seriously hindered by the influence of gravity. Two major experiments were carried out in space environment very

successfully: the so-called Lambda Point Experiment (LPE) and the Confined Helium Experiment (CHEX)[1]. CHEX was designed to test the validity of finite-size-scaling (FSS) theory of critical phenomena[2, 3, 4]. If the system is confined in geometries of reduced dimensionality, when the critical point is approached, the correlation length can become as large as the size of the confining length. In this case the values of global properties of the system, such as specific heat, are significantly different from their values for the bulk system. FSS theory can be used to determine the general dependence of a global property on the confining length-size near the critical point.

Though earlier experiments on superfluid helium films of finite thickness [5] seemed to confirm the validity of the FSS, there were more recent experiments[6, 7] where it was shown that the superfluid density of thick helium films does not satisfy FSS when the expected values of critical exponents were used. Similarly, in previous measurements of the specific heat of helium in finite geometries, other than the expected values for the critical exponents were found [8].

Our group had performed a number of simulations of equilibrium critical properties such as specific heat and superfluid density of helium restricted in various geometries including the film geometry used in CHEX. Our results, published[9, 10] a few years before the execution of CHEX, were found to be in satisfactory agreement to the results of CHEX[1]. We believe that our simulations can be used for predicting the outcome of more future major experiments. In addition to testing the theoretical framework on which the simulations are based, our simulations may be used to help design the experiment.

In the so-called BEST (Boundary Effects in the Superfluid Transition)[11], the thermal conductivity of helium confined in pore geometry and in parallel plate geometry will be measured. This experiment tests dynamical properties with respect to scaling and the critical exponents associated with thermal conductivity. Encouraged by the success of simulations of equilibrium properties we have developed techniques and computational tools to study critical dynamics and finite-size scaling of transport coefficients such as thermal conductivity using computer simulations. We have used these techniques to compute the thermal conductivity of superfluids in various confining geometries and investigate their finite-size scaling. Here we present results for such dynamical critical phenomena relevant to BEST and demonstrate that using the tools and techniques which we have developed we can perform computations which will yield support and accurate predictions for such experiments.

## 2 Models for Static Critical Properties

At any temperature below  $T_c$ , a sample of liquid helium large on the scale of the correlation length may be characterized by a macroscopic order parameter  $\psi(\vec{r})$ . The order parameter for the case of the lambda transition is a complex number proportional to the local average value of the field operator. The theory of phase transitions begins by asserting that the important statistical complexes, whose excitations reduce the macroscopic degree of order, are states obtained by a spatially varying order parameter[14]  $\psi(\vec{r})$  defined on long length-scales down to a cutoff which is much longer than the interparticle spacing and smaller than the correlation length. Each such configuration at temperature  $T$  is assigned a free energy

$F[\psi]$ , which may be assumed to have the Landau-Ginzburg form. Formally, this is obtained by dividing the original system of microscopic degrees of freedom in blocks containing several original degrees of freedom and by carrying out the partial trace

$$e^{-\beta F[\psi]} \equiv \text{Tr}' e^{-\beta \hat{H}}.$$

Here  $\beta = 1/k_B T$  and this trace is over all possible microscopic states inside each block which are consistent with the value  $\psi(\vec{r})$  of the order parameter for a block located at  $\vec{r}$ , which is an average over the microscopic degrees of freedom. The equilibrium thermodynamic properties of the system are obtained by performing the remaining partition function sum of  $e^{-F/k_B T}$  over fluctuations in  $\psi(\vec{r})$ . The average value of an observable  $O$  can be expressed as a functional integral over configurations of  $\psi(\vec{r})$ , namely

$$\langle O \rangle = \frac{1}{Z} \int \mathcal{D}\psi O(\psi) e^{-\beta F[\psi]} \quad (1)$$

$$Z = \int \mathcal{D}\psi e^{-\beta F[\psi]}. \quad (2)$$

The most singular terms of the thermodynamic functions near the critical point are insensitive to the precise form of the functional form of  $F[\psi]$  and the critical exponents are the same for an entire class of such functionals. The following Landau-Ginzburg free-energy functional can be used to describe the fluctuations of the order parameter  $\psi$

$$F[\psi(\vec{r})] = \int d^d x \left( \frac{1}{2} |\nabla \psi|^2 + \frac{1}{2} \mu_0 |\psi|^2 + u_0 |\psi|^4 \right). \quad (3)$$

Another form of the Landau-Ginzburg free energy for the lambda transition is the  $x - y$  model which is a special case of a more general case of models defined on a lattice with free energy given by

$$F[s^{(\alpha)}] = J \sum_{\langle ij \rangle, \alpha} s_i^{(\alpha)} s_j^{(\alpha)} \quad (4)$$

where the sum is over all nearest neighbors and

$$\sum_{\alpha=1}^n (s_i^{(\alpha)})^2 = 1 \quad (5)$$

Where  $n$  denotes the number of components of the order parameter. For the  $x - y$  model  $n = 2$  and the order parameter corresponds to a unit vector  $\vec{s}_i = (s_i^{(1)}, s_i^{(2)}) = (\cos \theta, \sin \theta)$ . The angle  $\theta$  is the phase of the order parameter, while the magnitude of the order parameter is frozen to unity. The renormalized free energy obtained by real-space integration over fluctuations with wavelengths smaller than a new larger cutoff will generate the free energy functional given by Eq. (3).

### 3 Studies of Equilibrium Properties

We have used a Monte Carlo approach and a hybrid Monte Carlo procedure similar in spirit to those of Refs.[9, 15] which consists of a combination of steps using the Metropolis update,



the Cluster update[16], and the over-relaxation algorithm[17]. Using such hybrid algorithms and our dedicated massively parallel cluster which is outlined later in this proposal, we typically generate of the order of 100,000 uncorrelated configurations from the equilibrium canonical ensemble at a given temperature. For the superfluid case, we have calculated several observables including the specific and superfluid density (which corresponds to the helicity modulus in our pseudo-spin notation) in various geometries and boundary conditions. These calculations have appeared in a number of earlier publications.[9, 10, 18, 19, 20, 15].

If the system is confined in a finite geometry (e.g. a cubic or film geometry) the singularities in the physical quantities are smoothed out and the finite-size scaling theory [2] is thought to well describe the behavior of the system at temperatures close to  $T_\lambda$ . The intuitive idea behind the finite-size scaling theory is that finite-size effects can be observed when the bulk correlation length  $\xi$  becomes of the order of the system size (for a film geometry this is the film thickness  $H$ ). For a physical quantity  $O$  this statement can be expressed as follows [3]:

$$\frac{O(t, H)}{O(t, H = \infty)} = f\left(\frac{H}{\xi(t, H = \infty)}\right), \quad (6)$$

$f$  is a universal function depending only on the geometry and the boundary conditions applied.

The experiment CHEX was a success and our results were satisfactory predictions. However, the test was made for the film geometry which goes through the crossover region to the pure 2D case where the well known Kosterlitz-Thouless transition occurs and that has some caveats with respect to scaling which we have pointed out in some of our previous publications[18].

Recently the results and the conclusions of the analysis of the experiment CHEX have been published[1] as well as those of more recent ground-based experiments[21, 22]; they are found to be in general agreement with the expectations from RG theory[23, 24, 25, 26]. Moreover, it was concluded[1] that the scaling function was in very good agreement with our prediction[9] based on numerical simulations of a model which belongs to the same universality class as the superfluid transition. In addition, the results of these simulations which were available well before the flight experiment, provided a guide to the CHEX team in planning the experiment. Fig. 1 is taken from Ref.[1] where the CHEX collaboration compares their results with theoretical predictions.

Since the renormalization group calculations are approximate, numerical investigations of the finite-size scaling properties of static and dynamic critical properties need to be carried out as an independent tool to study the validity of the theory.

The simulation techniques could be considered “exact” for a given finite-size system; however, the limitation of this approach is the finite system size used in the simulations. To obtain control over this problem we have taken the following steps:

We have developed and adopted algorithms such as the so-called cluster algorithm[16], the over-relaxation method[17], the Metropolis algorithm as well as combination of these updates to produce more efficient hybrids. We have completed a massively parallel cluster of processors with very high performance to cost ratio which we are using to simulate critical static and dynamic properties.

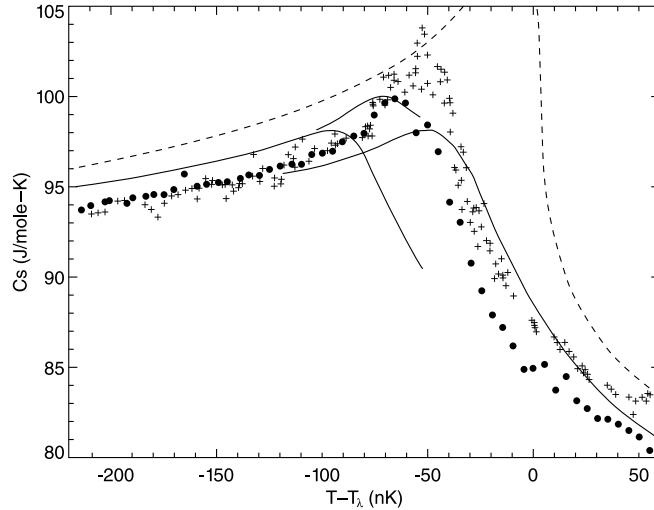


Figure 1: Comparison of the theoretical expectations to the CHeX results (Solid Circles). This figure is taken from the paper by Lipa, et al. [1]. The plus signs are the results of simulations (Schultka and Manousakis[9]). The solid lines are results from Dohm's group. The dashed line is the result for bulk.

It will be of great interest to compare the specific heat scaling function for other geometries. For example when the confining dimensions are two instead of one, i.e., in pore-like geometry the crossover is from 3D to 1D. The 1D system is not characterized by any other singularity similar to the dimensional crossover from 3D to the 2D case. We have calculated the specific heat scaling function for pore-like geometry (more precisely we used bar-like geometry) and we have compared it to that for the film geometry and this is shown in Fig. 2 Notice the very different behavior of the scaling function and how strongly it carries the “fingerprint” of the geometry. While Lipa and coworkers[28] have roughly tested our prediction with ground based experiments, it is necessary (Lipa et al.[27] have proposed to do this) to carry out microgravity experiments on much bigger confining size pores. In addition, using our most recently developed computational tools and techniques, we plan to carry out calculations using significantly larger size pores to provide a much better test of finite-size scaling than the one achieved by CHEX.

## 4 Dynamical Critical Phenomena

### 4.1 Progress in Finite-Size Scaling Theory of Transport

In recent years the experiments have measured accurately transport properties in well-defined geometries have been made[29, 30, 32]. In the past, transport properties and in particular thermal conductivity for bulk helium has been extensively studied theoretically[31]. Rather recently, Kahn and Ahlers[32] measured the thermal conductivity of  $^4\text{He}$  confined in a glass capillary array of thickness 3 mm with holes 2  $\mu\text{m}$  in diameter. Their results show that long cylindrical samples have a transition from three-dimensional to one-dimensional behavior. However measurements over a wide range of the confining length  $H$  are required in order to

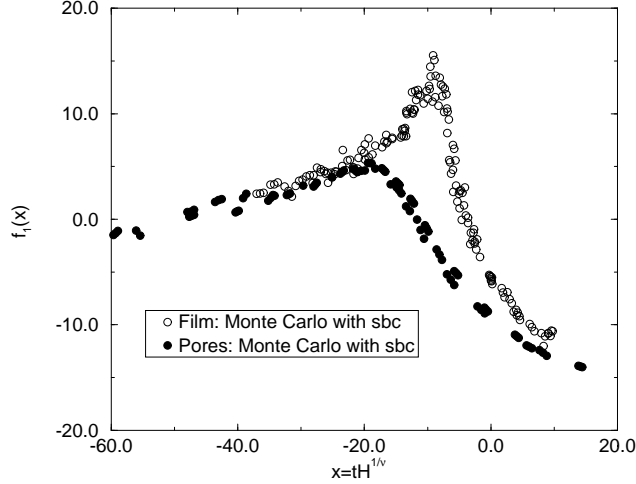


Figure 2: Comparison of the calculated specific heat scaling function near the lambda point for pore and film geometry

test the finite-size scaling theory for transport properties; experiments are planned to study dynamical exponents near the critical point and to study the finite-size scaling behavior of the thermal conductivity in pore-like geometries (BEST experiment).

There are already results for other models which are not directly related to superfluids. Koch, Dohm, and Stauffer[34] presented field-theoretical and numerical studies of the validity of dynamic finite-size scaling for relaxational dynamics in cubic geometry with periodic boundary conditions above and below  $T_c$ . Quantitative agreement between theory and Monte Carlo data was obtained by them. In addition, Koch and Dohm[35] have predicted the dynamic finite-size scaling function for the effective diffusion constant of model  $C$  of Hohenberg and Halperin[36].

Bhattacharjee[37] derived an approximate form of the scaling function for the thermal conductivity using a decoupled-mode approximation and model  $E$ . Krech and Landau[38] have calculated the thermal conductivity of bulk  $^4\text{He}$  using Monte Carlo spin dynamics simulations of the  $XY$  model in three dimensions on a simple cubic lattice with periodic boundary conditions.

## 4.2 Simulation of Critical Dynamics

To describe the dynamics of a superfluid, we use a model which is classified as model  $F$  by Hohenberg and Halperin[36]. Matsubara and Matsuda[39] has proposed model  $F$  to explain the properties of liquid  $^4\text{He}$ . The planar magnet model and the  $XY$  model[15] belong in the same universality class and the former can also be used to describe the dynamics of superfluid  $^4\text{He}$ .

In the pseudospin notation, the planar magnet model takes the following form:

$$H = -J \sum_{\langle ij \rangle} (S_i^x S_j^x + S_i^y S_j^y), \quad (7)$$

where the summation is over all nearest neighbors,  $\vec{S}_i = (S_i^x, S_i^y, S_i^z)$ , and  $J$  sets the energy scale. While the two pseudo-spin components of the order parameter correspond to the usual superfluid complex order parameter, the third corresponds to the particle density. The third component is introduced in order to describe dynamic evolution. When we consider the equilibrium critical properties of this model by including the third component of the order parameter, we find that the planar magnet model and the  $XY$  model have the same critical exponents[15].

We will use a hybrid Monte Carlo procedure similar in spirit to that of Refs. [15, 40] which consists of a combination of steps using the Metropolis update, the Cluster update[16], and the over-relaxation algorithm[17]. Using such hybrid algorithms, we typically generate 3,000-10,000 uncorrelated configurations from the equilibrium canonical ensemble at a given temperature. Each configuration is evolved using the equations of motion for the planar magnet model which are given as follows

$$\frac{d}{dt}\vec{S}_i = \frac{\partial H}{\partial \vec{S}_i} \times \vec{S}_i. \quad (8)$$

These equations are obtained from the planar magnet model following the procedure outlined in Ref. [36]. In our simulation, starting from a particular initial spin configuration, we perform numerical integration of these equations of motion. Using the decomposition method[41], the integration is carried out to a maximum time  $t_{max}$  (typically of the order of  $t_{max}=400$  in our units) with a time step  $\delta t=0.05$ . This way we determine the real-time history of every configuration within a sufficiently long interval of time ( $0 \leq t \leq t_{max}$ ).

We compute the thermal conductivity on the appropriate lattice geometry and boundary conditions. The thermal conductivity  $\lambda$  of  $^4He$  at a given temperature  $T$  will be calculated using the dynamic current-current correlation function[38]:

$$\lambda = \frac{1}{k_B T \chi_{zz} \pi} \int_0^\infty dt \sum_i \langle j_0^z(0) j_i^z(t) \rangle, \quad (9)$$

where the out-of-plane static susceptibility

$$\chi_{zz} = \langle M^z{}^2 \rangle / (k_B T L^3) \quad (10)$$

is needed for normalization. The  $z$ -component  $j_i^z$  of the current density  $\vec{j}_i$  associated with the lattice point  $i$  is defined by

$$j_i^z = J(S_i^y S_{i+e_z}^x - S_i^x S_{i+e_z}^y), \quad (11)$$

where the notation  $i + e_z$  denotes the nearest neighbor of the lattice site  $i$  in the  $z$  lattice direction.

In the experimental results of Kahn and Ahlers[32] the thermal resistivity  $R = 1/\lambda$  was reported. We would like to check the finite-size scaling hypothesis for the thermal resistivity  $R(t, H)$ . The dependence upon  $t$  of the bulk thermal resistivity can be described by the power law

$$R(t) = R_0 t^\pi, \quad (12)$$

where  $\pi$  is the dynamic critical exponent. Using Eq.(1), the finite-size scaling expression for the thermal resistivity  $R(t, H)$  is given by

$$R(t, H)H^{\pi/\nu} = f(tH^{1/\nu}), \quad (13)$$

where the function  $f(x)$  is universal and  $\nu=0.6705$  is the critical exponent of the correlation length[33].

### 4.3 Finite-Size Scaling: Predictions for BEST

To demonstrate that calculations of FSS studies of dynamic critical properties are possible and they can provide useful information, we have recently computed the thermal conductivity on  $H \times H \times L$  lattices, where  $H=6,8,10,12,14,20$  and  $L \approx 5H$  with open boundary condition along the  $H$  direction and periodic along the long direction  $L$ . Using FSS we have estimated the dynamic critical exponent  $\pi$  of the thermal resistivity and the scaling behavior of the thermal resistivity with respect to  $H$ .

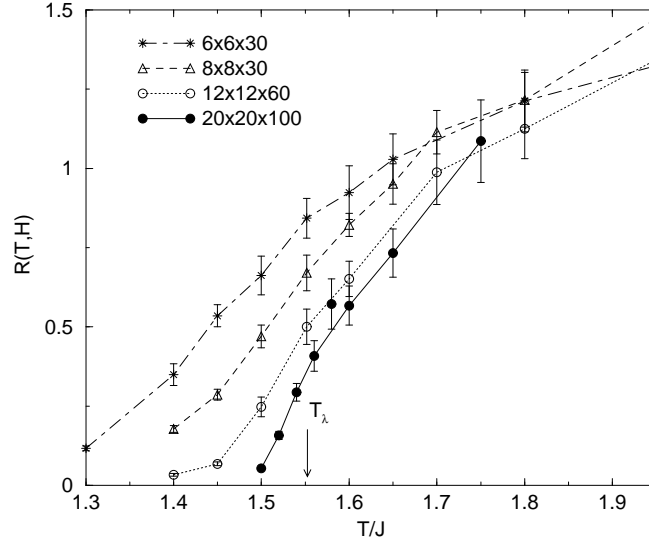


Figure 3: Thermal resistivity  $R(T, H)$  versus temperature for various lattice sizes

Fig. 3 shows our results for the thermal resistivity as a function of temperature  $T$  (in units of  $J$ ) for various lattice sizes with open boundary conditions in the  $H$  direction. The computations of dynamical properties are far more CPU time intensive and demanding large computational resources. Using the same amount of CPU time, the statistical fluctuations of the data are bigger than those in the data of the static observables. We found that the thermal resistivity feels strong finite-size effects. In bulk helium  $R(t)$  approaches zero as the bulk transition temperature  $T_\lambda$  is approached from above. The lower arrow in Fig. 3 shows the bulk transition temperature  $T_\lambda=1.5518$  obtained from Monte Carlo simulation using the planar magnet model[15].

Fig. 4 shows a scaling plot of the thermal resistivity  $R(t, H)$  versus reduced temperature, where the reduced temperature is taken relative to the bulk transition temperature  $T_\lambda$ . Our

Monte Carlo data collapse onto a universal curve  $f(x)$ . We have used the same value for the critical exponent  $\pi = 0.4397$  as determined by Ahlers[42]. However, the dynamic scaling theory[43] had predicted a divergence in  $\lambda$  with a critical exponent equal to  $\pi = \nu/2 = 0.335$  which is different from the value reported by Ahlers. Within our large error bars the results of our simulation also collapse on a different single scaling function using the theoretical value of  $\pi$  giving a lower quality of the fit. The renormalization group calculations can explain the difference between the experimental effective critical exponent of 0.44 and the asymptotic exponent of  $\nu/2$  in terms of non-universal corrections which vanish extremely slowly as  $T_\lambda$  is approached.

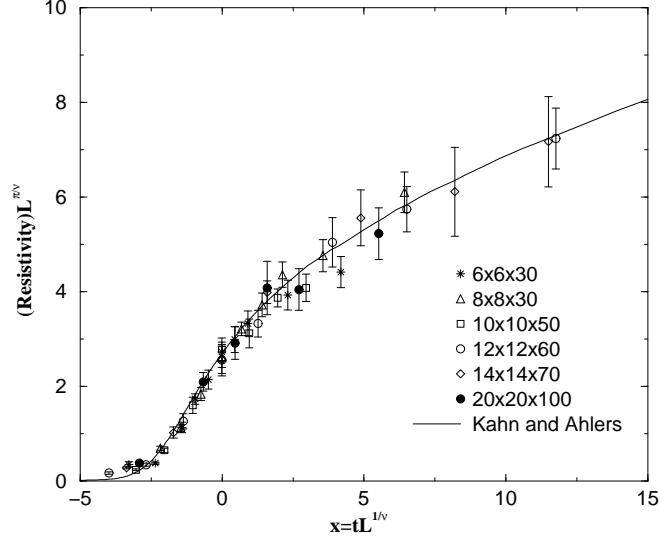


Figure 4: The scaling function of thermal conductivity  $f_\lambda(x)$  for pore geometry with open boundary conditions as obtained by rescaling the results of our simulation Fig. 3. The solid line are the experimental results.

In Fig. 4 we also compare our universal function  $f_\lambda(x)$  with the experimental data points obtained by Kahn and Ahlers[32]. In order to do this, we used two multiplicative constants as free fitting parameters, one multiplying the scale of  $x$  axis and another the scale of  $y$ . The agreement between Monte Carlo simulation and experiment is quite satisfactory. We have demonstrated[9] that the boundary conditions play a role in defining the universal function  $f(x)$ . We believe that if we use more realistic boundary conditions such as Dirichlet boundary conditions along the  $H$ -direction we can reduce the number of fitting parameters to only one. In this proposal the role of the boundary condition as well as that of the geometry will be studied.

In summary we have computed the heat capacity and the thermal resistivity  $R(t, H)$  of liquid  $^4\text{He}$  in a pore-like geometry, i.e., an  $H \times H \times L$  lattice, applying Dirichlet and open boundary conditions in the  $H$  direction respectively. The heat capacity can be tested in microgravity and it is a natural extension of CHeX. In addition, we have demonstrated that using finite-size scaling theory, and the experimentally determined dynamic critical exponent  $\pi$  our results for the  $R(t, H)$  for various different values of  $H$  collapse onto a universal scaling function which agrees rather well with the present experimental data. In future work we plan

to study the role of the boundary conditions as well as the role of the geometry on the thermal conductivity.

## 5 Future Calculations

During our meeting, we also presented results of preliminary calculations on thermal resistivity of helium confined in parallel plate geometry. We[44] are in the process of finalizing these calculations on larger size systems and we plan to publish the results soon.

In addition, during the meeting we presented results of our quantum Monte Carlo calculation of submonolayer of hydrogen on graphite. These results are now published and can be found in Ref.[45].

## 6 Acknowledgements

This work was supported by the National Aeronautics and Space Administration under grant No. NAG3-1841 and NAG8-1773.

## References

- [1] J.A. Lipa, D.R. Swanson, J.A. Nissen, Z.K. Geng, P.R. Williamson, D.A. Stricker, T.C.P. Chui, U.E. Israelsson and M. Larsen, Phys. Rev. Lett. **84**, 4894 (2000); and J. Low Temp. Phys. **113**, 849 (1998).
- [2] M. E. Fisher and M. N. Barber, Phys. Rev. Lett. **28** 1516 (1972); M. E. Fisher, Rev. Mod. Phys. **46** 597 (1974); V. Privman, Finite Size Scaling and Numerical Simulation of Statistical systems, Singapore: World Scientific 1990.
- [3] E. Brezin, J. Physique **43** 15 (1982).
- [4] V. Privman, J. Phys. **A23** L711 (1990).
- [5] J. Maps and R. B. Hallock, Phys. Rev. Lett **47** 1533 (1981). D. J. Bishop and J. D. Reppy, Phys. Rev. Lett. **40**, 1727 (1978).
- [6] I. Rhee, F. M. Gasparini, and D. J. Bishop, Phys. Rev. Lett. **63** 410 (1989).
- [7] I. Rhee, D. J. Bishop, and F. M. Gasparini, Physica **B165&166** 535 (1990).
- [8] T. Chen and F. M. Gasparini, Phys. Rev. Lett. **40** 331 (1978); F. M. Gasparini, T. Chen, and B. Bhattacharyya, Phys. Rev. **23** 5797 (1981).
- [9] N. Schultka and E. Manousakis, Phys. Rev. Lett. **75**, 2710 (1995).
- [10] N. Schultka and E. Manousakis, J. Low Temp. Phys. **V 109**, 733 (1997).
- [11] G. Ahlers, Private Communication and AIP Conf. Proc. **502**, 450 (2000).

- [12] J. A. Lipa, Private Communication.
- [13] N. Schultka and E. Manousakis, J. Low Temp. Phys. **V 111**, 783 (1998).
- [14] P. C. Hohenberg and P. C. Martin, Annals Phys. **34**, 291 (1965). P. C. Hohenberg, A. Aharony, B. I. Halperin, and E. D. Siggia Phys. Rev. **B 13**, 2986 (1976). P. C. Hohenberg and B. I. Halperin Rev. Mod. Phys. **49**, 435 (1977). V. Ambegaokar, B. I. Halperin, D. R. Nelson and E. D. Siggia, Phys. Rev. **B21** 1806 (1980). D. R. Nelson and J. M. Kosterlitz, Phys. Rev. Lett. **39**, 1201 (1977). J. V. Jose, L. P. Kadanoff, S. Kirkpatrick, and D. R. Nelson, Phys. Rev. **B16**, 1217 (1977) S. Teitel and C. Jayaprakash, Phys. Rev. **B27** 598 (1983). Y.-H. Li and S. Teitel, Phys. Rev. **B40** 9122 (1989).
- [15] K. Nho and E. Manousakis, Phys. Rev. **B 59**, 11575 (1999).
- [16] U. Wolff, Phys. Rev. Lett. **62**, 361 (1989).
- [17] F.R. Brown and T.J. Woch, Phys. Rev. Lett. **58**, 2394 (1987).
- [18] N. Schultka and E. Manousakis, Phys. Rev. **B51**, 11712 (1995).
- [19] N. Schultka and E. Manousakis, Phys. Rev. **B52**, 7528 (1995).
- [20] N. Schultka and E. Manousakis, Phys. Rev. **B49** 12071 (1994). K. Nho and E. Manousakis, Phys. Rev. **B 59**, 11575 (1999).
- [21] S. Mehta and F.M. Gasparini, Phys. Rev. Lett. **78**, 2596 (1997).
- [22] S. Mehta, M.O. Kimball and F.M. Gasparini, J. Low Temp. Phys. **114**, 467 (1999).
- [23] R. Schmolke, A. Wacker, V. Dohm, and D. Frank, Physica **B165 & 166** 575 (1990).
- [24] V. Dohm, Physica Scripta **T49** 46 (1993).
- [25] P. Sutter and V. Dohm, Physica **B194-196** 613 (1994); W. Huhn and V. Dohm, Phys. Rev. Lett. **61** 1368 (1988).
- [26] M. Krech and S. Dietrich, Phys. Rev. **A46** 1886 (1992), 1922 (1992).
- [27] J. A. Lipa, private communication.
- [28] J. A. Lipa et al., J. Low Temp. Phys. **113**, 849 (1998).
- [29] J.A. Lipa and T.C.P. Chui, Phys. Rev. Lett. **58**, 1340 (1987); T.C.P. Chui, Q. Li, and J.A. Lipa, Jpn. J. Appl. Phys. **26**, Suppl. 26-3, 371 (1987).
- [30] G. Ahlers and R. V. Duncan, Phys. Rev. Lett. **61**, 846 (1988).



- [31] B.I. Hohenberg and E.D. Siggia, Phys. Rev. Lett. **32**, 1289 (1974); Phys. rev. B **13**, 1299 (1976); E.D. Siggia, Phys. Rev. B **13**, 3218 (1976); C. DeDominici and L. Peliti, Phys. Rev. Lett. **38**, 505 (1977); Phys. Rev. B **18**, 353 (1978); V. Dohm, Z. Phys. B **31**, 327 (1978); R.A. Ferrell and J.K. Bhattacharjee, Phys. Rev. Lett. **42**, 1638 (1979); J. Low Temp. Phys. **36**, 165 (1979); P.C. Hohenberg, B.I. Halperin, and D.R. Nelson, Phys. Rev. B **22**, 2372 (1980); V. Dohm and R. Folk, Z. Phys. B **40**, 79 (1980); Phys. Rev. Lett. **46**, 349 (1981); G. Ahlers, P.C. Hohenberg, and A. Kornblit, Phys. Rev. Lett. **36**, 493 (1981); Phys. Rev. B **25**, 3136 (1982); V. Dohm and R. Folk, Z. Phys. B **45**, 129 (1981); **41**, 251 (1981); V. Dohm, Phys. Rev. B **44**, 2697 (1991).
- [32] A.M. Kahn and G. Ahlers, Phys. Rev. Lett. **74**, 944 (1995).
- [33] L. S. Goldner and G. Ahlers, Phys. Rev. **B 45**, 13129 (1992).
- [34] W. Koch, V. Dohm, and D. Stauffer, Phys. Rev. Lett. **77**, 1789 (1996).
- [35] W. Koch and V. Dohm, Phys. Rev. E **58**, R1179 (1998).
- [36] P.C. Hohenberg and B.I. Halperin, Rev. Mod. Phys. **49**, 435 (1977).
- [37] J.K. Bhattacharjee, Phys. Rev. Lett. **77**, 1524 (1996).
- [38] M. Krech and D.P. Landau, Phys. Rev B **60**, 3375 (1999).
- [39] T. Matsubara and H. Matsuda, Prog. Theor. Phys. **16**,416 (1956); **16**, 569 (1956);**17** 19 (1957).
- [40] K. Nho and E. Manousakis, Phys. Rev. **B 64**, 44513 (2001).
- [41] J. Frank, W. Huang, and B. Leimkuhler, J. Comp. Phys. **133**, 160 (1997); M Krech, A. Bunker, and D.P. Landau, Comp. Phys. Commun. **111**, 1 (1998).
- [42] G. Ahlers, J. Low Temp. Phys. **115**, 143 (1999).
- [43] R.A. Ferrell, N. Menyhard, H. Schmidt, F. Schwabl, and P. Szepfalusy, Phys. Rev. Lett. **18**, 891 (1967).
- [44] K. Nho and E. Manousakis, work in progress.
- [45] K. Nho and E. Manousakis, Phys. Rev. **B 65**, 115409 (2002).

# MISTE Flight Experiment Status

M. Barmatz, F. Zhong, Inseob Hahn and M. Weilert

*Jet Propulsion Laboratory, California Institute of Technology  
4800 Oak Grove Drive, Pasadena, CA 91109*

The MISTE flight experiment has made significant scientific and technical progress in preparing for a future microgravity flight. We are collaborating with several theoretical modeling groups that have developed crossover (equation-of-state) models for predicting thermodynamic behavior near the liquid-gas critical point. Computer codes for these models are being prepared in preparation for analyzing future MISTE flight data. Several of these models have already been used to test experimental measurements of the heat capacity at constant volume, isothermal susceptibility, and coexistence curve in the crossover region near the  $^3\text{He}$  liquid-gas critical point. A brief description of these models and a representative fit to experimental data will be presented. An important technical advancement required for the successful completion of the MISTE flight experiment is the development of a low temperature valve that can be actuated multiple times. In collaboration with Mission Research Corporation, MISTE has been testing a new small pneumatic valve for use at low temperatures. The results of recent successful low temperature actuation tests will also be discussed.

## I. INTRODUCTION

The main objective of the MISTE flight experiment is to perform pressure, density and temperature measurements as well as heat capacity at constant volume and isothermal susceptibility measurements near the  $^3\text{He}$  liquid-gas critical point. This study is important because these thermodynamic quantities diverge and measurements very close to the transition can be used to unambiguously test critical phenomena scaling theories that apply to all simple fluids.

The MISTE experiments will determine the asymptotic critical amplitudes and exponents for  $C_V$  and  $\chi_T$  above and below the transition. To more clearly understand the meaning of this statement, Eq. (1) shows the theoretically expected behavior of the isothermal susceptibility along the critical isochore above the transition and along the coexistence curve below the transition.

$$\chi_T^{\pm*} = (P_c/\rho_c^2)\chi_T^{\pm} = \Gamma_0^{\pm}|t|^{-\gamma}[1 + \Gamma_1^{\pm}|t|^{\Delta_s} + \dots], \quad (1)$$

where  $\gamma \simeq 1.24$  is a universal critical exponent that defines the strength of the susceptibility divergence and  $\Gamma_0^\pm$  are system-dependent asymptotic critical amplitudes. In this expression, the + sign indicates above the transition and the - sign below. The asymptotic region is very close to the critical point where critical fluctuations dominate the behavior of the system. In this region, the susceptibility is expected to follow the power law behavior given by the leading term. The MISTE flight experiment will obtain values for the asymptotic critical amplitudes and critical exponent.

Farther away from the transition, the system enters the crossover region where it slowly changes from critical behavior to mean field behavior. In this region, correction-to-scaling terms, shown in the brackets of Eq. (1), become important. These terms are generally called Wegner correction terms.  $\Gamma_1^\pm$  are system dependent amplitudes and  $\Delta_s$  is another exponent that describes crossover behavior. Ground-based measurements provide information about the crossover region.

There are expressions similar to that shown in Eq. (1) for other thermodynamic quantities such as the heat capacity at constant volume and shape of the coexistence curve. A new flight guest experiment called Coexistence Boundary Experiment (COEX)[1] is being considered to use the MISTE flight hardware. The COEX experiment will accurately determine the shape of the coexistence curve. By combining the MISTE/COEX flight measurements with corresponding ground-based thermodynamic measurements, we can test the predictions of critical phenomena theories both in the asymptotic region as well as in the crossover region. These predictions will include the amplitude ratios and exponent scaling relations. The approach to be taken is to perform measurements primarily along the critical isochore or path of constant critical density, the critical isotherm or path of constant critical temperature and the liquid and gas sides of the coexistence curve.

## II. GROUND EXPERIMENTAL ACTIVITIES

We have spent considerable time and effort in upgrading the ground-based MISTE cryostat. A new donut shaped cell was fabricated. This design will permit the cell to withstand higher pressures than the previous cell design. We will now be able to perform measurements along the critical isochore to  $\approx 11$  K. This will allow a determination of the crossover to mean field behavior as well as the analytic background contributions.

We have also significantly improved the High Resolution Thermometer readout electronics. This was accomplished by developing a flux counter system that can read at least 60,000 flux counts/sec. This means that we will not lose count of temperature changes even for the fastest experimental temperature slewing rates.

This new measurement system is now being tested in preparation for a more precise set of thermodynamic measurements. Of particular significance is the ability to accurately measure the shape of the coexistence curve. The COEX approach for measuring the coexistence curve will also be used during this next run. Thus, for the first time, we will have a complete set of precision thermodynamic measurements within the crossover region obtained in the same apparatus. These combined sets of measurements will provide a stringent test of theoretical crossover models.



### III. THEORETICAL ACTIVITIES

During this last year, the main emphasis in this area has been to analyze existing ground-based measurements using the predictions of recent theoretical models. We have been developing collaborations with theoreticians to improve and test their models. Here are listed some of these collaborations and the progress that has been made.

The Minimal Renormalization  $\phi^4$  model was initially developed by Volker Dohm and co-workers[2][3] to make predictions for the lambda point. The MISTE team has applied this approach to the  $O(1)$  universality class that includes the liquid-gas critical point. There are three articles already published[4]-[6] that use our  $C_V$  and  $\chi_T$  data to test this approach, and a detailed description of this application to the  $O(1)$  universality class is in preparation[7].

Another field theoretical approach called the Massive Renormalization  $\phi^4$  model was also developed by Bagnuls and Bervillier several years ago[8][9]. They have recently extended their model to cover the complete classical-to-crossover region[10]. We recently developed computer fitting routines for their various models and have fit heat capacity, susceptibility and coexistence curve  $^3\text{He}$  data using these models. The results of this analysis is now being prepared for publication[11].

We have worked closely with Professor Anisimov and co-workers in testing their new crossover parametric model (CPM)[12]. A joint article was initially published comparing their model against  $^3\text{He}$  heat capacity and susceptibility measurements[4]. These data were also used in their paper that gave a complete description of this model[12]. We have just finished developing a computer code for the complete equation-of-state form of their model and are now prepared to use this code to also include coexistence curve measurements in the analysis.

The most recent advancement is a new field-theoretical parametric crossover model (PCM) developed in collaboration with Joseph Rudnick who is a co-investigator on MISTE. This is a complete equation-of-state model that satisfies the most accurate field theoretical predictions of Guida and Zinn-Justin[13] in the asymptotic limit and also satisfies the mean field predictions[14] far away from the transition. The model has the critical exponents and amplitude ratios fixed at the latest theoretical values. A computer code is now being developed and testing against  $^3\text{He}$  measurements is in progress[15].

As an example of our analyses of recent theoretical models, Fig. 1 shows a fit of  $^3\text{He}$  susceptibility data to the PCM model. The susceptibility data were scaled by the leading power-law behavior in order to provide a more sensitive test of the theory. For this initial fit to the theory, we manually adjusted the three model parameters to give a reasonable fit to the data. The parameters  $u$  and  $\tau$  are the fundamental model parameters and must be the same for fitting any other  $^3\text{He}$  thermodynamic parameter. The parameter  $A_s$  adjusts the susceptibility amplitude. We see that this manual fit is reasonably good and we can extract estimates of the leading and first Wegner critical amplitudes both above and below the transition. Of course we plan to perform more thorough non-linear least square fits in the near future. It should be noted that these are gravity free data that only approach the transition to a reduced temperature of  $|t| \cong 10^{-4}$ . The MISTE microgravity experiment should be able to extend these data another two decades closer to the critical point.

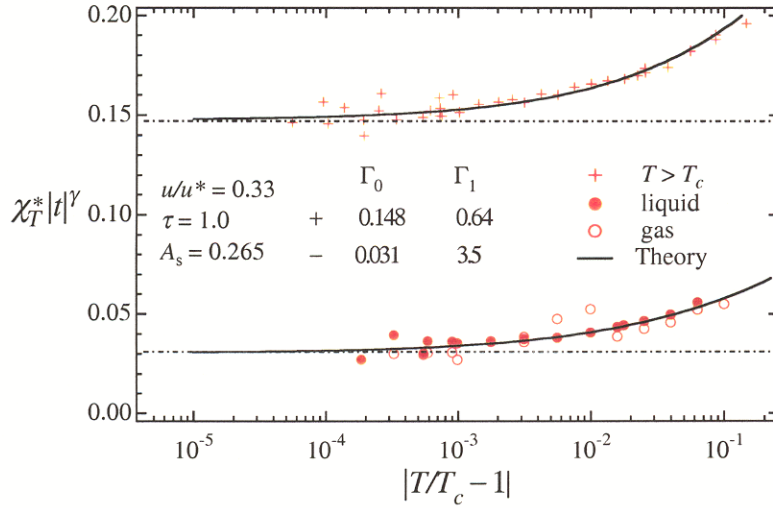


FIG. 1: Manual fit of the PCM model to  $^3\text{He}$  susceptibility data both above and below the critical point. The parameter  $\tau$  was held constant and the parameters  $u$  and  $A_s$  were adjusted.

#### IV. FLIGHT ENGINEERING ACTIVITIES

In order for the flight experiment to be successful, we need a low temperature mini-valve that can be actuated many times in-situ. We have been collaborating with Mission Research Corporation (MRC) and have recently successfully tested a prototype mini-valve. The valve body is approximately 3.8 cm in diameter by 4.4 cm long. A more detailed description of this valve design has already been published[16]. The leak rate determined during the actuation study is shown in Fig. 2. The valve was actuated over 200 times with the leak rate being generally below  $2 \times 10^{-7}$  std cc/s. The requirement for the MISTE flight is  $1 \times 10^{-6}$  std cc/s for 25 cycles. Thus, this valve satisfies these requirements and further tests of a flight-like valve are planned.

Progress has also been made in developing the MISTE flight cell. It consists of a 5.9 cm inner diameter by 3.2 cm height cylindrical cell body that contains the  $^3\text{He}$  fluid. The cell will have approximately 60 copper plates and 60 copper spacers each being 0.025 cm thick. The plates will have a large number of small holes to permit fluid to communicate between adjacent local 0.025 cm thick cells. These plates and spacers are introduced to reduce the thermal equilibration time which becomes very long near the critical point. There will also be two sets of temperature, density and pressure sensors attached to the cell. These cell components are now being fabricated.

The MISTE flight cell and associated sub-systems will be situated on the Low Temperature Microgravity Physics Facility (LTMPF) probe. This entire assembly will be sealed in a vacuum can and inserted in the LTMPF dewar. Figure 3 shows an assembly drawing of the MISTE instrument sensor package integrated with the probe support structure. The MISTE flight cell is at the top of the probe and the probe is attached to the dewar cold plate. The cold plate is 25 cm in diameter and the height of the assembly shown here is



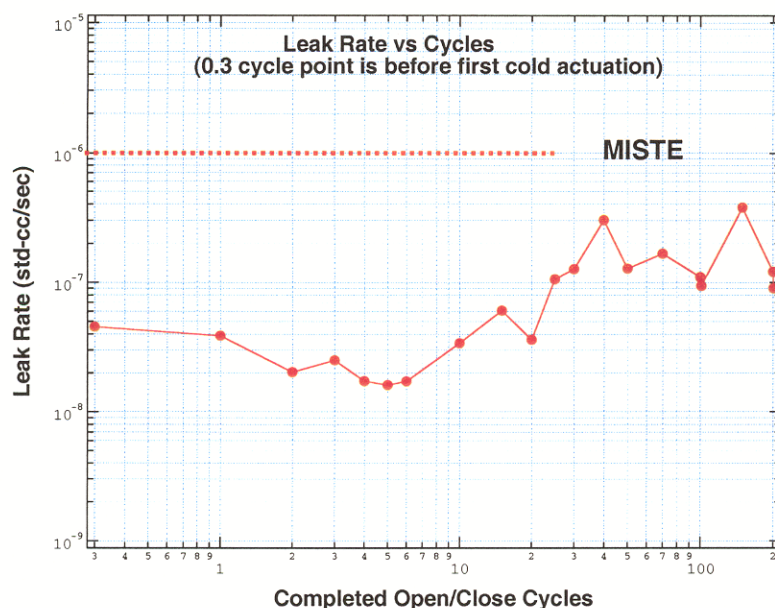


FIG. 2: Leakrate of MRC valve versus number of actuation cycles. Leakrate remained below the MISTE requirement of  $1 \times 10^{-6}$  std cc/s for 200 actuation cycles.

approximately 40 cm. The probe support consists of three isolation stages. Each stage has better than a 1000:1 isolation from the previous stage. With this level of isolation, a temperature resolution of better than a nano-Kelvin at the MISTE cell can be attained. In the final assembly, the shield stage will have an aluminum radiation shield that will surround the MISTE cell to improve thermal isolation. A vacuum can, that surrounds this entire assembly, will be sealed at the cold plate.

In conclusion, a new MISTE ground-based cell has been fabricated and will be use to perform a complete set of thermodynamic measurements in the critical region ( $PVT$ ,  $C_V$ ,  $\chi_T$ , coexistence curve shape). Computer fitting routines for several recent theoretical critical point models have been developed and these models are being tested using ground-based measurements. All of the MISTE flight hardware components have been designed and are now being fabricated for testing.

## ACKNOWLEDGMENTS

We would like to acknowledge the engineering support given to the MISTE flight experiment by Hyung Cho, Jim Granger, Ellyn McCoy, Steven Patrick, Siu-Chun Lee, and David Johnson. The research described in this article was carried out at the Jet Propulsion Laboratory, California Institute of Technology, under contract with the National Aeronautics and Space Administration.

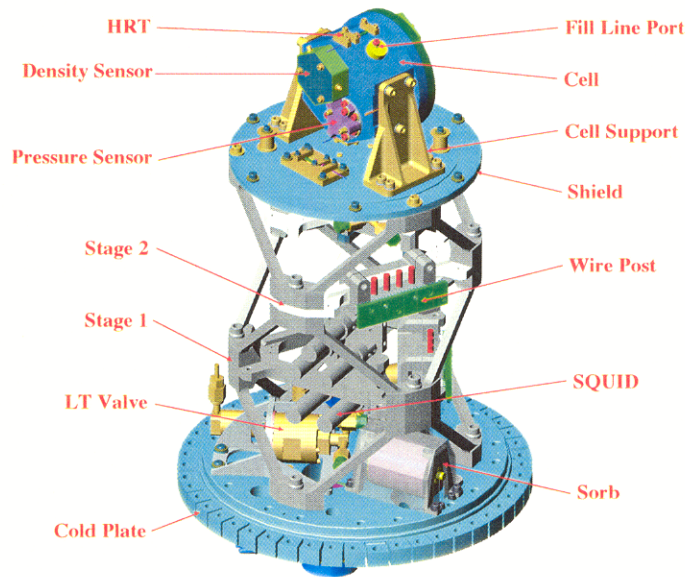


FIG. 3: The MISTE instrument sensor package integrated with the LTMPF probe support structure.

## REFERENCES

- [1] Inseob Hahn, Science Requirements Document, JPL No. D-23024, (2002).
- [2] R. Schloms and V. Dohm, Nucl. Phys. B **328**, 639 (1989).
- [3] H. J. Krause, R. Schloms, and V. Dohm, Z. Phys. B: Conds. Matter **79**, 287 (1990).
- [4] M. Barmatz, I. Hahn, F. Zhong, V. A. Agayan, and M. A. Anisimov, J. Low Temp. Phys., **121**, 633 (2000).
- [5] Inseob Hahn, Fang Zhong, M. Barmatz, Rudolf Haussmann and Joseph Rudnick, Phys. Rev. E, **63**, 055104(R), (2001).
- [6] M. Barmatz, F. Zhong, and I. Hahn, Proceedings of the 2nd Pan Pacific Basin Workshop on Microgravity Sciences (CD-ROM), Eds. N. Ramachandran and M. Lee, (2001).
- [7] F. Zhong, M. Barmatz, and I. Hahn, to be published.
- [8] C. Bagnuls and C. Bervillier, Phys. Rev. B **32**, 7209 (1985).
- [9] C. Bagnuls, C. Bervillier, D. Meiron, and B. Nickel Phys. Rev. B **35**, 3585 (1987).
- [10] C. Bagnuls and C. Bervillier, lanl.arXiv.org **hep-th**, 0112209 (2002).
- [11] F. Zhong and M. Barmatz, to be published.
- [12] V. A. Agayan, M. A. Anisimov, and J. V. Sengers, Phys. Rev. E, **64**, 026125, (2001).
- [13] R. Guida and J. Zinn-Justin, J. Phys. A: Math. Gen. **31**, 8103 (1998).
- [14] J. Binney, *The theory of critical phenomena: an introduction to the renormalization group* (Clarendon Press; Oxford University Press, Oxford New York, 1993)
- [15] J. Rudnick, M. Barmatz, and Fang Zhong submitted to The 23rd International Conference on Low Temperature Physics.
- [16] M. Weilert, I. Hahn, M. Barmatz, D. Higham and G. Frodsham, Proceedings of the 2001 Space Cryogenics Workshop, Cryogenics **41**, 813 (2002).

## **Progress on two superfluid gyroscopes**

Richard Packard  
University of California  
Berkeley, CA 94720

We are developing two types of sensitive superfluid rotation sensors, i.e gyroscopes. One type is based on phase slippage in He-4. This device has advanced to a 13-turn pickup loop with  $100 \text{ cm}^2$  enclosed area. We find that there is no long-term drift and that there are no detectable unknown noise sources. Our present device displays the intrinsic noise floor of about  $5 \times 10^{-3}$  of the Earth's rotation rate. Our second device is a proof-of-principle prototype based on the DC Josephson effect in He-3. We have made the analog of a DC-SQUID and modulated the current by reorienting the pickup loop with respect to the Earth's rotation axis. Our first instrument includes a pickup area of  $6 \text{ cm}^2$  and the noise is due to ambient building vibrations, not intrinsic processes.



## Using Cesium containers to suppress nucleation in quantum fluids

A. Nguyenle, P. Taborek, and J.E. Rutledge  
University of California, Irvine

Cesium substrates have an unusually weak interaction with adsorbates and are the only substrates not wet by liquid  $^4\text{He}$ . In containers made of conventional strong-binding materials such as copper, nucleation of the liquid-vapor phase transition in  $^4\text{He}$  and phase separation in  $^4\text{He}$ - $^3\text{He}$  mixtures takes place via a wetting layer on the walls of the container. We are investigating the possibility of suppressing nucleation in these phase transitions using a cesiated container. Suppressing nucleation would allow thermodynamic measurements on quantum fluids in a previously inaccessible range of temperature and density. We will discuss theoretical estimates of the limits of supercooling, and progress on the fabrication of a helium filled cesiated cell as well as experimental techniques to detect supercooling.

## Mode Splitting of Levitated Helium Drops

C. Vincente, W. Yao, H. J. Maris and G. M. Seidel

Physics Department, Brown University, Providence, Rhode Island 02912

We have been studying the properties of drops of liquid helium levitated, by virtue of the diamagnetism of helium, by a magnetic field. The field is produced by a superconducting solenoid of such a configuration as to produce a stable trap for suspending drops[1]. The combined effect of gravity and the magnetic field can be described by the potential energy per unit volume  $U(x, y, z)$  of the helium. If the origin of the coordinate system  $x, y, z$  is chosen to coincide with the minimum of the trap potential, then close to the potential minimum, the trap can be described by a harmonic potential,

$$U(x, y, z) = U_0 + k_{xy}(x^2 + y^2) + k_z z^2, \quad (3)$$

In order for the drop to have lateral stability, it is necessary to have  $k_{xy} > 0$ . This is achieved if the magnitude of the magnetic field increases as a function of the horizontal distance  $(x^2 + y^2)$  from the levitation point. The constants  $k_{xy}$  and  $k_r$  are functions of the current in the magnet and in general are not equal. Thus, the trap does not have spherical symmetry and so a drop suspended in the trap will not be spherical.

We have measured the surface tension of superfluid helium at low temperatures using the well known Rayleigh expression[2] for the frequency of the vibrational modes of oscillation of a spherical, incompressible and inviscid drop,

$$\omega_l^2 = \frac{\sigma}{\rho a^3} (l(l-1)l(l+2)),$$

where  $\sigma$  is the surface tension,  $\rho$  is the density of the liquid, and  $a$  is the radius of the drop. The mode number,  $l$ , can be any integer equal to or larger than 2. A measurement of the vibrational frequency can thus be used to determine  $\sigma$  provided that the radius and density are known.

A number of possible corrections to the Rayleigh frequency need to be considered including the effects of charge (used to excite the oscillations), influence of the helium

vapor, and viscosity of the liquid. The effects of these perturbations are inconsequential. However, the shape of the magnetic trap used to levitate the drops can have a small but dramatic effect on the vibrational modes. In Fig. 1 is illustrated the  $l = 2$  mode, which is observed to split into three modes by an amount that depends on the current in the solenoid. The influence of the trap potential of axial symmetry is to lift the 5-fold degeneracy of the  $l = 2$  mode, splitting it into three frequencies, two of which are doubly degenerate.

We have considered the effect on the normal modes of a weak external potential having axial symmetry, which exerts a body force on every part of the liquid drop[3]. A related problem has been discussed by Cummings and Blackburn[4] who have treated the case of a non-spherical pressure on the surface of a drop.

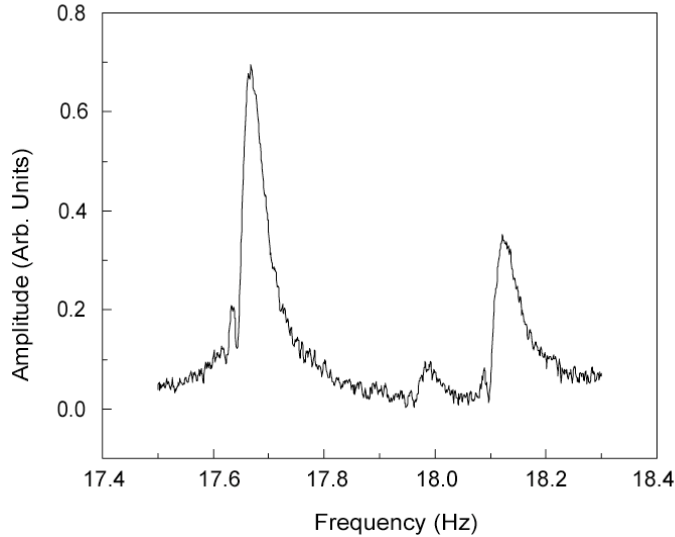


Fig. 1. Vibrational spectrum for the  $l = 2$  modes of a drop of radius 0.117 cm at a temperature of 1.4 K. The magnet current was 117 A.

The result of the calculations yield for the frequencies of the  $l = 2$  mode

$$\omega_{20} = \left( \frac{8\sigma}{\rho a^3} \right)^{1/2} [1 + 2A + B], \quad \omega_{21} = \omega_{2\bar{1}} = \left( \frac{8\sigma}{\rho a^3} \right)^{1/2} [1 + A + B],$$

$$\text{and } \omega_{22} = \omega_{2\bar{2}} = \left( \frac{8\sigma}{\rho a^3} \right)^{1/2} [1 - 2A + B], \quad \text{where}$$

$$A = \frac{19a^3}{168\mu}(k_z - k_{xy}), \quad B = \frac{a^3}{12\mu}(k_z + 2k_{xy}),$$

and  $k_{xy}$  and  $k_z$  are the coefficients entering into the trap potential.

We are able to calculate the potential due to the trap from the magnet current and the known geometry of the magnet windings. The values of the spring constants  $k_{xy}$  and  $k_z$  are used to compute the splittings of the modes as a function of the current in the magnet. The results of the calculations, with one adjustable parameter to fix the current at which  $k_{xy} = k_z$ , are compared with the experimental results in Fig. 2. It can be seen that the agreement between theory and experiment is very good.

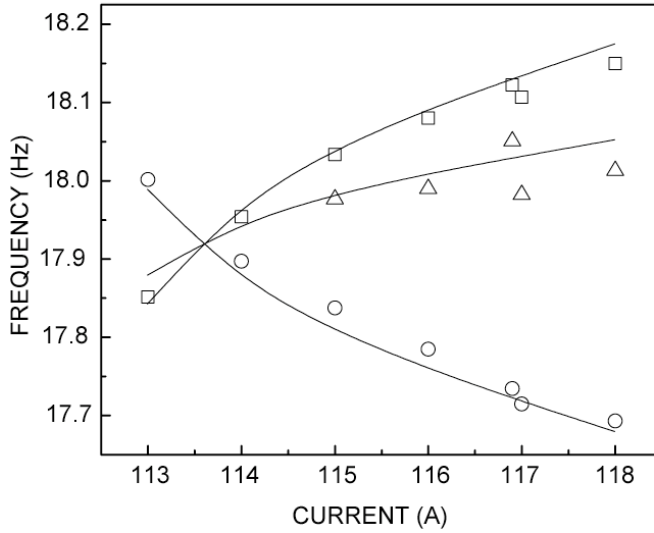


Fig. 2. Frequency of the  $l = 2$  modes of a drop of radius 0.117 cm as a function of magnet current at 1.4 K. The three different modes are denoted by the triangles, squares and circles. The solid lines are the results of calculations

#### References:

- [1] M.A. Weilert, D.L. Whitaker, H.J. Maris and G.M. Seidel, J. Low Temp. Phys. **106**, 1 (1997).
- [2] Lord Rayleigh, Proc. Roy. Soc. Lond. **29**, 71 (1879).
- [3] C. Vincente, W. Yao, H. J. Maris and G. M. Seidel, Phys. Rev. submitted.
- [4] D.L. Cummings and D.A. Blackburn, J. Fluid Mech. **224**, 395 (1991).

## The Fluctuations of the Phase Difference Across An Array of Josephson Junction

Talso Chui and Warren Holmes  
Jet Propulsion Laboratory  
Pasadena, CA 91109

We present calculations of the thermodynamic fluctuations of the phase difference  $\phi$  across an array of Josephson junctions in superfluid  $^4\text{He}$ . We use a model of the Josephson effect, analogous to a rigid pendulum, to understand the dynamics of  $\phi$  in the limit of large fluctuations. In this model, the angle sustained by the pendulum is analogous to  $\phi$ . We show that the rms fluctuations of  $\phi$  increase as the lambda transition is approached. At a critical value of  $\phi$ , the fluctuations of  $\phi$  can exceed  $2\pi$  causing a continuous phase slip. The probability of a phase slip increases closer to the lambda point until  $\phi(t)$  becomes chaotic and the Josephson effect disappears. We show that the mean square fluctuations of  $\phi$  decrease  $\sim 1/N$ , where  $N$  is the number of orifices in the array. We show that for a single junction of dimension  $L \times L \times L$ , near the lambda transition where the correlation length is  $\sim L$ , there is already a significant probability of phase slip. This means that the Josephson effect does not occur in a single junction but does occur in an array of such junctions.